Surface acoustic wave investigations of low dimensional electron systems

Nash, Geoffrey Richard

Award date:
1996

Awarding institution:
University of Bath

Surface Acoustic Wave Investigations of Low Dimensional Electron Systems

Submitted by Geoffrey Richard Nash

for the degree of Ph.D.

of the University of Bath

1996

Geoffrey Nash

ProQuest LLC
789 East Eisenhower Parkway
P.O. Box 1346
Ann Arbor, MI 48106-1346

Abstract

The electronic properties of low dimensional systems have been probed using surface acoustic wave (SAW) scattering. Arrays of quantum wires and dots were fabricated from a modulation doped MBE grown AlGaAs/GaAs heterostructure using reactive ion etching and holographic lithography. Interdigital transducers, which were deposited on the edges of the samples, were used both to excite and detect the SAWs. Due to the piezoelectric coupling between the SAWs and the electronic systems there are very small changes in the attenuation and velocity of a SAW pulse with magnetic field at low temperatures, and a sensitive detection system was developed to measure these.

With the SAWs propagating perpendicular to quantum wires strong oscillations were observed in the transmitted intensity (which were mirrored in the velocity measurements) reflecting the magnetic depopulation of 1D subbands as described by a full quantum mechanical description of the SAW - electron interaction. With the SAWs parallel to the wires the SAW - electron scattering rate is suppressed at low electron concentrations in narrow wires as predicted on the basis of phase space arguments. Surprisingly, at high electron concentrations, the SAW attenuation increases sharply to where it is a factor of three larger than in the unstructured two dimensional electron gas. We speculate that this is due to the excitation of intraband 2D plasmon-like modes.

In quantum dots the transmitted SAW intensity shows a broad asymmetric minimum as a function of magnetic field, which reflects the density of single electron energy level crossings per unit magnetic field interval. A simple model, assuming parabolic confinement, predicts a peak in the level crossing density at low magnetic fields and a corresponding decrease in SAW amplitude is observed. At high magnetic fields, where the single electron model predicts no interaction, the magnetic field dependence of the SAW intensity may signify that many body effects are important.

Acknowledgements

The work presented in this thesis was carried out at the School of Physics, University of Bath with financial support from the Royal Society and the Engineering and Physical Sciences Research Council of the United Kingdom.

I would like to express my sincere thanks to all those who have helped me in any way with this work, in particular:

Dr. Simon Bending for his excellent supervision, constant enthusiasm and encouragement, and for many of the ideas on which this work is based.

Gordon Sowersby of Barman Electronics for designing and building our unique phase sensitive detector.

Prof. K. Von Klitzing for giving me the opportunity to prepare the samples at the Max-Planck-Institute, Stuttgart, and to everyone at the Institute for helping make my visit so productive. I am very grateful to Yvonne Kershaw for all her help during my stay.

Mauro Boero for performing the Fermi's Golden Rule calculations of the scattering rates, and Prof. J. C. Inkson for useful discussions.

The technical staff of the School of Physics, particularly Bob Draper for his help in a vast range of tasks. It has been a great pleasure to work and socialise with the staff and students of the School (even the football team).

My flat-mate Iain Goodfellow who has been writing-up at the same time as me and has therefore been the ideal companion.

The members of the Quantum Electronics Group, past and present, for providing comradeship and humour throughout the many highs and lows: Simon Stoddart, Zul Othaman, Virginia Lam, Dan Carey, Mark Dellow, Ahmet Oral, Jon Pinto and Mukesh Mistry.

Finally my thanks go to my parents and family for their unfaltering support and encouragement.

Contents

1 Introduction

1.1 Motivation

Over the fifty or so years since the invention of the transistor the semiconductor industry has grown rapidly to become one of the worlds largest and most important businesses. Underlying this growth have been the remarkable technological achievements of integration and miniaturisation, the results of which have had a profound impact on modern society, particularly in computing and consumer electronics. Although other semiconductors are used for optical and microwave devices it is silicon that is still dominant in the manufacture of electronic components. Over the last two decades or so, however, there has been a dramatic increase in research in a new area of semiconductor science and technology; that of low-dimensional-systems (LDS). Research into such systems began with the demonstration of resonant tunnelling through quasi-two-dimensional (2D) bound states in a GaAs/AlGaAs quantum well structure by Chang, Esaki and Tsu [1]. This was the first experimental evidence that electrons (or holes) confined to a single layer, by the larger conduction band energy of neighbouring materials, will exhibit properties based on their quantum mechanical properties if the layer width is comparable to the extent of the electron wavefunction. Central to the initial development of low dimensional semiconductor systems, therefore, has been the refinement of epitaxial growth techniques, such as molecular beam epitaxy (MBE) [2] and metal organic vapour deposition (MOCVD) [3], which can be used to prepare semiconductor multilayers one atomic layer at a time, with independent control over both the composition of the semiconductor and the level of doping in each layer.

The most extensively studied material system has been $Al_xGa_{1-x}As/GaAs$, where the size of the offset between the conduction band in the two materials is controlled by the Al fraction x. The technique of modulation doping, in which electrons are spatially separated from their parent donors, has enabled the fabrication of high mobility quasi-2D sheets of electrons, confined at the interface of a single $Al_xGa_{1-x}As/GaAs$ heterojunction. In such structures the electron motion is free only in the directions parallel to the crystal interface, so forming a two dimensional electron gas (2DEG). A wide range of devices, such as the high electron mobility transistor (HEMT) [4], have been realised from such two dimensional systems, which have also have provided the ideal basis for the study of numerous important physical phenomena such as the integer [5] and fractional quantum Hall effects [6] (IQHE, FQHE respectively).

Confinement of electrons in two and three dimensions produces one and zero dimensional systems, known as quantum wires and dots respectively. Such systems have often been fabricated by taking a two-dimensional system and adding an extra degree of confinement, either by physical patterning of the semiconductor [7], or by using a metal gate to define a constriction [8]. Much of the work on quantum wires and dots has been based on structures fabricated from $Al_xGa_{1-x}As/GaAs$ heterojunctions, and these have been used to study phenomena such as the quantisation of 1D conductance [9] and the Coulomb blockade [10]. It has long been recognised that semiconductor quantum wires and dots could form the basis of electronic and optical devices with superior performance compared to existing devices [11]. For example quantum wires could form the basis of very high mobility transistors due to the reduced phase space for carrier scattering in 2D confined systems, and lasing from quantum dots should occur with high efficiency and at lower threshold current than either in quantum wells or wires.

Power considerations require that practical devices will be based on arrays of such structures and there is a pressing need to further the understanding of the physics of these arrays.

Surface acoustic waves (SAWs) are elastic waves which are confined to the surface of a crystal and they have been utilised for many years in electronic devices such as filters and delay lines [12] because of their slow speed compared with electromagnetic waves. Wixforth et al [13] first investigated the interaction of SAWs with the 2DEG formed at an $Al_xGa_{1-x}As/GaAs$ heterojunction. As the applied magnetic field is increased at low temperatures the measured SAW intensity and velocity shift oscillate, with the oscillations following those of the measured DC magnetoconductivity. A classical relaxation model was used to describe the interaction of the electric field of the propagating SAWs on piezoelectric GaAs with the conduction electrons in the 2DEG. Since these pioneering measurements were made SAWs have been used extensively to investigate 2D systems in the QHE regime [15-20] and more recently in the FQHE [21-26]. Additionally the currents and voltages induced by momentum transfer from the SAWs to electrons, the acoustoelectric effect, have been used as a probe of 2D and 1D systems [27-34].

In this thesis SAWs have been used for the first time to investigate the properties of quantum wire and dot arrays. This technique has many advantages. It is a contactless measurement and ideal for studying large area arrays with good signal-to-noise ratio (the samples investigated in this thesis had arrays of area ~$9mm^2$). SAW generation using interdigital transducers (IDT) is strongly directional, allowing studies to be made with the SAWs propagating perpendicular or parallel to quantum wires, and the long wavelength used in these measurements $(\lambda = 40\mu m)$ rules out possible

diffraction effects. The low frequency of the SAWs $(f = 70MHz)$ means that the SAW-electron interaction is quasi-elastic in contrast to other techniques such as far infrared spectroscopy [35]. To perform this work instrumentation has been developed, based upon a custom-built phase sensitive detector, that is capable of measuring very small changes in the measured SAW intensity and velocity shift (better than 1 part in 10^3 and 1 part in 10^4 respectively)

A key aspect of the interpretation of the results presented in the thesis is the use of a quantum mechanical (QM) approach to the SAW-electron scattering. The classical relaxation model used for describing the SAW-2D electron interaction is not applicable when the SAWs propagate either perpendicular to the quantum wires or are incident on quantum dots. Treating the interaction as a small perturbation SAW-electron scattering rates have been calculated for the first time using Fermi's Golden Rule.

1.2 Overview of Thesis

Two, one and zero dimensional electron systems were studied. The electronic properties of such systems are reviewed in Chapter 2, with particular emphasis placed on their properties in magnetic fields applied perpendicular to the supporting substrate. The aim of the chapter is not to provide a complete review of the many interesting properties that such systems have, but to introduce the concepts relevant to later chapters. Chapter 3 is an introduction to the properties of Surface Acoustic Waves. Emphasis is again placed on concepts of importance to later chapters. The classical relaxation model, used to describe the interaction between electrons in a 2D system and SAWs, is outlined in this chapter as is the quantum mechanical approach to SAW-

electron scattering. The experimental work was carried out on an AlGaAs/GaAs heterostructure, grown by MBE, and on samples containing arrays of quantum wires and dots that were patterned from the same wafer. Chapter 4 describes the fabrication of the samples together with the experimental apparatus used to make measurements of SAW intensity and velocity shift.

The experimental results for SAW scattering from a 2DEG, arrays of quantum wires, and arrays of quantum dots are presented in Chapters 5, 6, 7 respectively. With the 2DEG oscillations in the SAW amplitude and velocity shift were observed in an increasing magnetic field, as seen by previous workers. We note for the first time that the QM calculation of scattering rate, which is included for the 2DEG at the end of Chapter 5, contains the characteristic splitting observed, and predicted by the classical model, in the SAW amplitude around integer filling factors. An infrared LED was used during measurements on the quantum wires and dots to increases the electron concentration via the persistent photoconductivity effect. With the quantum wires measurements were made in two orientations, with the SAWs propagating either perpendicular or parallel to the wires, as a function of illumination level and magnetic field, for 500nm and 250nm wide wires. The strong observed anisotropy is compared with the calculated scattering rates, which are also presented in Chapter 6. Measurements were also made as a function of illumination and magnetic field for 500nm and 250nm wide dots, and the experimental data is again compared with the calculated scattering rates for an idealised dot geometry. A description of the velocity shift measurements is also given in each chapter, although as far as we know no model to describe these yet exists. Chapter 8 contains the conclusions, and some suggestions for future work

2 Properties of Low Dimensional Electron Systems

2.1 Introduction

Semiconductor research has for the last twenty years been to a large extent dominated by the physics and properties of low dimensional systems. The spatial confinement of electrons (or holes) in one, two, or three dimensions leads to two, one or zero dimensional systems. In such systems the electronic mean free path is comparable with the size of the confinement and quantum rather than classical mechanics describes the energy and properties of the electrons. It is the unusual properties of the confined electrons or holes that has generated great excitement concerning their practical applications. In this chapter a brief outline is given of some of the physics of ideal low dimensional systems. However, there is not room here to discuss all the interesting phenomena, such as the quantisation of the conductance [9,36] in one dimensional systems and the Coulomb Blockade in zero dimensional systems [10], that have been discovered and investigated. A number of books [4,37,38] have been written on the physics and technology of low dimensional semiconductor systems over the last few years. The actual low dimensional samples investigated by Surface Acoustic Waves (SAWs) in this work will be described in Chapter 4.

2.2 Two Dimensional Systems

2.2.1 Zero Magnetic Field Properties

In a two dimensional (2D) system electrons (or holes) are confined in one dimension by an electrostatic potential, so forming a two dimensional electron gas (2DEG), and their energy becomes quantised in the confinement direction. In a real system the confining potential can be complicated to calculate as a self-consistent solution of Poisson's and Schrödinger's equations is required. The simplest approximation that can be made for the potential is to consider an electron in an infinite square well, with the confinement in the z direction. Since the electron motion is unrestricted in the x and y directions the electron wave function $\Psi(\mathbf{r})$ is separable with planewave solutions for the x and y motion:

$$\Psi(\mathbf{r}) = e^{ik_x x} e^{ik_y y} \psi(z) \tag{2.1}$$

where $\psi(z)$ obeys the one-dimensional Schrödinger equation for a particle in a box, the solutions to which are sines and cosines of the form $\psi(z) = \sin(k_z z)$ and are shown schematically in *Figure 2.1a* (page 9). As the wavefunction must be zero on the boundaries of, and outside the well (of width a) the wavevector k_z has to equal $p\pi/a$ with $p = 1,2,3,\ldots$ The allowed energy associated with the electron's z-motion is therefore quantised into a discrete set of energy levels E_p usually known as electronic subbands:

$$E_p = \frac{\hbar^2 \pi^2 p^2}{2m^* a^2}, \quad p = 1,2,3,\ldots \tag{2.2}$$

where m^* is the effective mass.

The total electron energy is the combination of the quantised energy in the z direction and the continuum of energy states in the unconfined x and y directions:

$$E_p(k_x,k_y) = E_p + \frac{\hbar^2 k_x^2}{2m^*} + \frac{\hbar^2 k_y^2}{2m^*} \tag{2.3}$$

and is sketched in *Figure 2.1b*. In a 2D system each electron state occupies an area of $(2\pi)^2/A$ in momentum space, where A is the area of the system, and in a circle of constant energy of radius k the number of electrons N_e is given by:

$$N_e = 2\pi k^2 \frac{A}{(2\pi)^2} \tag{2.4}$$

where the factor of two is included to account for spin. Using the free electron energy dispersion, $k^2 = 2m^*E/\hbar^2$, the number of electrons per unit area n is hence:

$$n = \frac{N_e}{A} = \frac{m^*E}{\pi\hbar^2} \tag{2.5}$$

The density of states (DOS) per unit energy, $\partial n/\partial E$, for one subband is therefore independent of energy:

$$\frac{\partial n}{\partial E} = \frac{m^*}{\pi\hbar^2} \tag{2.6}$$

The DOS in each subband is constant (if m^* is independent of energy) and the total density of states $D_{2D}(E)$, also sketched in *Figure 2.1b*, is a step-like function with increasing energy:

$$D_{2D}(E) = \frac{m^*}{\pi\hbar^2}\sum_p \theta(E - E_p) \tag{2.7}$$

where θ is the Heaviside step function:

$$\theta(x - x') = 0 \quad x\langle x' \tag{2.8}$$

$$= 1 \quad x\rangle x'$$

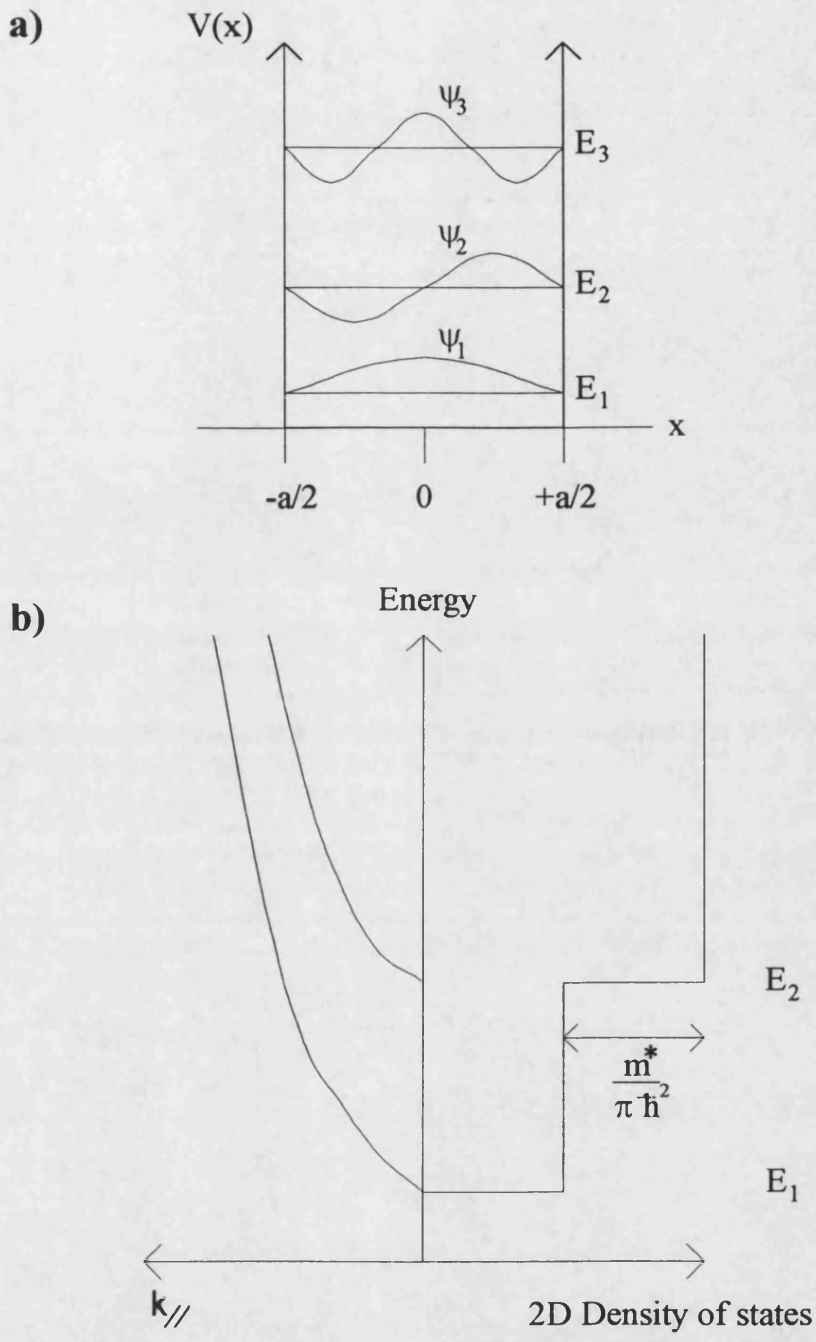

Figure 2.1: *(a) The first few energy levels and wavefunctions for a particle in an infinite square well potential. (b) Left: Parabolic energy dispersion in k-space in the plane of a 2DEG. E_1 and E_2 indicate the energies of the first two electronic subbands. Right: Schematic representation of the density of states, per unit area and per unit energy, of a 2DEG with zero applied magnetic field.*

2.2.2 Properties in a Perpendicular Magnetic Field

The application of a magnetic field to a 2DEG imposes a Lorenz force on the electrons in a direction perpendicular to both the field and to their direction of motion. If the field direction is perpendicular to the plane of the 2DEG then in strong magnetic fields the electrons will follow closed circular orbits in the *x-y* plane known as cyclotron orbits. The magnetic field introduces an extra degree of confinement in addition to the electrostatic confinement. To solve for the electron wavefunctions and energy levels in the magnetic field it is usual to introduce the magnetic field through the vector potential A, where $\underline{\nabla} \wedge A = B$ and $\underline{\nabla}.A = 0$, so that the Hamiltonian becomes:

$$\hat{H} = \frac{1}{2m^*}(\hat{p} + eA)^2 \tag{2.9}$$

where $\hat{p}$ is the momentum operator $-i\hbar\underline{\nabla}$. By choosing the Landau gauge for the vector potential $A = (0, Bx, 0)$ we obtain a uniform magnetic field in the *z*-direction. The Schrödinger equation (assuming that the effective mass approximation still holds) therefore becomes:

$$\frac{1}{2m^*}\left(-\hbar^2\frac{\partial^2}{\partial x^2} - \hbar^2\frac{\partial^2}{\partial y^2} - 2i\hbar eB_z x\frac{\partial}{\partial y} + e^2B_z^2x^2\right)\psi = E\psi \tag{2.10}$$

as in 2D we assume that $\partial/\partial z = 0$. Solutions can be found of the form:

$$\psi(x,y,z) = u(x)e^{ik_y y} \tag{2.11}$$

and an equation for *u(x)* is therefore obtained:

$$-\frac{\hbar^2}{2m^*}\frac{\partial^2 u}{\partial x^2} + \frac{e^2B_z^2}{2m^*}\left(x + \frac{\hbar k_y}{eB_z}\right)^2 u(x) = (E - E_z)u(x) \tag{2.12}$$

The above Schrödinger equation is that for a one-dimensional harmonic oscillator centred at the point x_0, where $x_0 = -\hbar k_y / eB_z$, with the following Hamiltonian:

$$\hat{H} = \frac{\hat{p}_x^2}{2m^*} + \frac{m^* \omega_c^2}{2}(x - x_0)^2 \tag{2.13}$$

where ω_c is the cyclotron frequency ($\omega_c = eB/m^*$). The eigenfunctions are of the form:

$$\psi_{n,k_y}(x,y) = \phi_n^L(x - x_0)e^{ik_y y} \tag{2.14}$$

where ϕ_n^L is the harmonic-oscillator function:

$$\phi_n^L \propto H_n\left(\left(\frac{m^*\omega_c}{\hbar}\right)^{1/2}(x - x_0)\right)e^{-\frac{m^*\omega_c(x-x_0)^2}{2\hbar}} \tag{2.15}$$

and H_n are Hermite polynomials [39]. The energy levels are:

$$E_n = (n + 1/2)\hbar\omega_c \tag{2.16}$$

where n is an integer 0, 1, 2,,... These energy levels are known as Landau levels and the total energy of the particle is given by:

$$E_{p,n} = (n + 1/2)\hbar\omega_c + E_p \tag{2.17}$$

where E_p is the quantised energy of the electron in the z direction. A further quantisation occurs within each Landau level due to the presence of spin-up and spin down electron states. Hence the Zeeman energy must be included in the complete energy spectrum:

$$E_{p,n,s} = (n + 1/2)\hbar\omega_c + E_p + sg^*\mu_B B_z \tag{2.18}$$

where μ_B is the Bohr magneton and $s = +1/2$ and $-1/2$ for spin up and spin down states respectively. The effective Landé g-factor g^* contains many-body corrections, as electron-electron interactions enhance the spin splitting of the electron states [40], and is dependent on the occupation of spin-up and spin-down states within each Landau level

(which is strongly magnetic field dependent). The zero magnetic field energy levels are quantised into a ladder of Landau levels, *Figure 2.2a* (page 14), with the number of electron states per Landau level, per spin and unit area, n_L, given by:

$$\frac{eB_z}{h} \tag{2.19}$$

The total density of states is a series of delta functions:

$$D_{2D}(E) = n_L \sum_{p,n,s} \delta(E - E_{p,n,s}) \tag{2.20}$$

and it is useful to define the filling factor ν as:

$$\nu = \frac{n_{2D}}{n_L} = \frac{hn_{2D}}{eB} \tag{2.21}$$

where n_{2D} is the two dimensional electron concentration, so that at integer filling factors an integer number of Landau levels are completely filled. In a real crystal disorder, for example the presence of impurity atoms near interfaces, will cause an energy broadening of the Landau level density of states. The broadened density of states was first modelled as sum of half-ellipses by Ando [41], however a more realistic model was developed by Gudmundsson and Gerhardts [42] to explain the significant DOS between Landau Levels measured in subsequent experiments[43],[44]. They gave the DOS as:

$$D_{2D}(E) = n_L \sum_n \frac{1}{\sqrt{2\pi\Gamma^2}} \exp\left[-\tfrac{1}{2}\left(\frac{E - E_{n,s}}{\Gamma}\right)^2\right] \tag{2.22}$$

where Γ is a measure of the broadening of each Landau level and depends on the type of disorder present in the crystal:

$$\Gamma = \hbar\sqrt{\frac{2eB}{\pi m^* \tau_B}} \tag{2.23}$$

where τ_B is a mean scattering time and importantly is not the same as that obtained from the low field magnetoresistance. To resolve the Landau levels experimentally their separation has to be greater than the average thermal energy of the particle and the intrinsic broadening of the levels. This only occurs at low temperatures and high magnetic fields for pure samples.

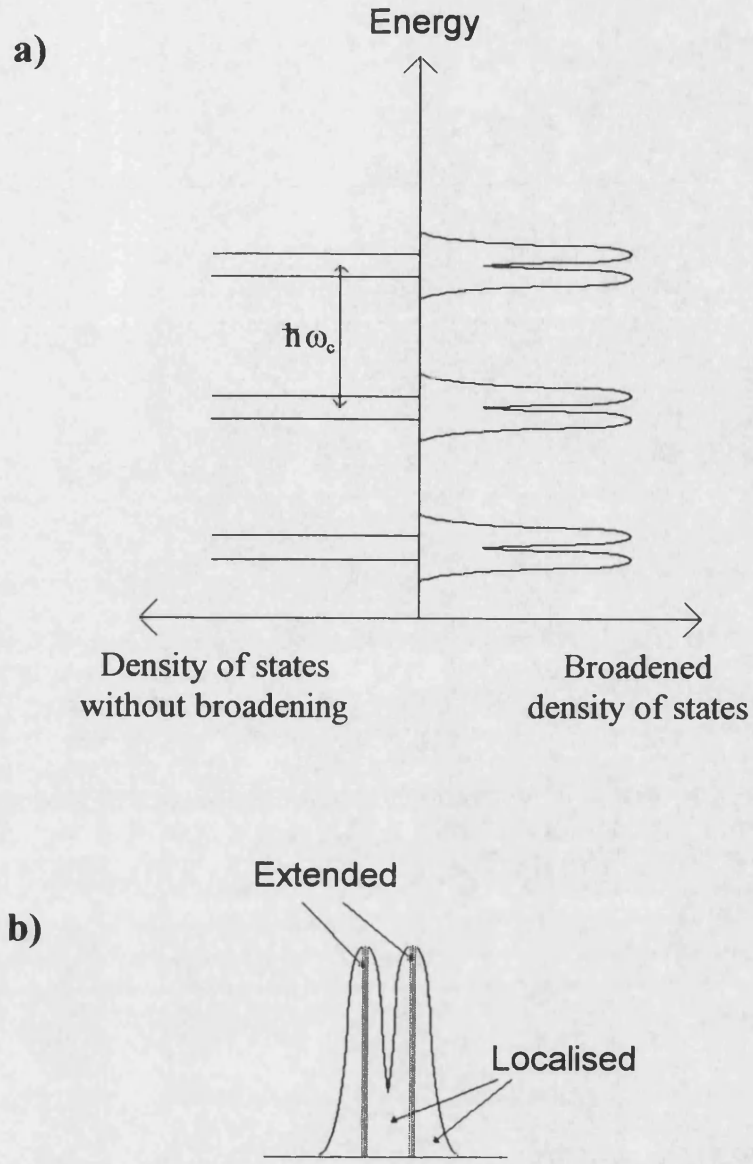

Figure 2.2: *(a) Left: The density of states, per unit area and per unit energy, for a 2D electron gas with a magnetic field perpendicular the to electron gas, causing Landau quantisation with a δ-function peak at each energy level. Here the levels are split into spin-up and spin-down and the enhanced g-factor is assumed to be the same for each Landau level. Right: The density of states including the level broadening caused by scattering. (b) Representation of the energy positions of localised and extended states within each level.*

2.2.3 Magnetoresistance in 2DEGs

At low temperatures the longitudinal resistivity tensor ρ_{xx} of a 2DEG oscillates with increasing magnetic field, and in *Figure 2.3a* the measured magnetoresistance of a 2DEG formed at the interface of an AlGaAs/GaAs heterojunction (see Chapter 4) is shown. These Shubnikov-de Haas (SdH) oscillations, which are periodic in 1/B, reflect the discrete nature of the DOS of the 2DEG at low temperatures in high magnetic fields, and they contrast starkly with the classical magnetoresistance which is a monotonic function of magnetic field. The applied electric field and the measured magnetoresistance ρ_{xx} are related via the tensor relationship:

$$\boldsymbol{E} = \rho(B)\boldsymbol{J} \tag{2.24}$$

where $\boldsymbol{J}$ is the current density and $\rho(B)$ is the magnetoresistivity tensor:

$$\rho(B) = \begin{bmatrix} \rho_{xx} & \rho_{xy} \\ -\rho_{xy} & \rho_{xx} \end{bmatrix} \tag{2.25}$$

As the magnetoconductivity tensor $\sigma(B)$ is the inverse of $\rho(B)$ it is simple to show that:

$$\rho_{xx} = \frac{\sigma_{xx}}{\sigma_{xx}^2 + \sigma_{xy}^2} \tag{2.26}$$

The resistivity is therefore proportional to the conductivity if σ_{xx} is small compared to σ_{xy}. At magnetic fields where the Fermi energy lies between Landau levels (integer filling factors) the DOS, conductivity, and hence the resistivity are at a minimum. At low integer filling factors (high magnetic fields) ρ_{xx} tends to zero over significant ranges of the magnetic field. This can be explained by considering the difference between electron states in the middle of a Landau level, which are *extended* and can carry current, and

those in the edges (or tails), which are *localised* and cannot carry current [45]; *Figure 2.2b*. Disorder in a crystal, for example impurities in a semiconductor heterostructure, causes fluctuations in the potential confining the electrons. The long range confining potential no longer appears constant to the electrons, but can be visualised instead as a landscape of potential hills and valleys. Electrons in the centre of a Landau level are able to move along equipotential lines that percolate through the sample and these states can therefore carry current. However, electrons in the Landau level tails follow cyclotron orbits that circle around a potential hill or valley and are therefore localised. The conductivity and resistivity therefore tend to zero when the Fermi energy lies in the tails of Landau levels near integer filling factors.

A plot of integer filling factor ν versus reciprocal magnetic field is a straight line:

$$\nu = \frac{hn_{2D}}{e}\frac{1}{B} \tag{2.27}$$

so that SdH measurements provide an accurate experimental method of measuring the 2D electron concentration n_{2D}. Other information, such as electron mobility and effective mass, can also be determined from these measurements. With high purity samples extra minima can be seen that correspond to each Landau level splitting into two, one minimum for spin up and one for spin down.

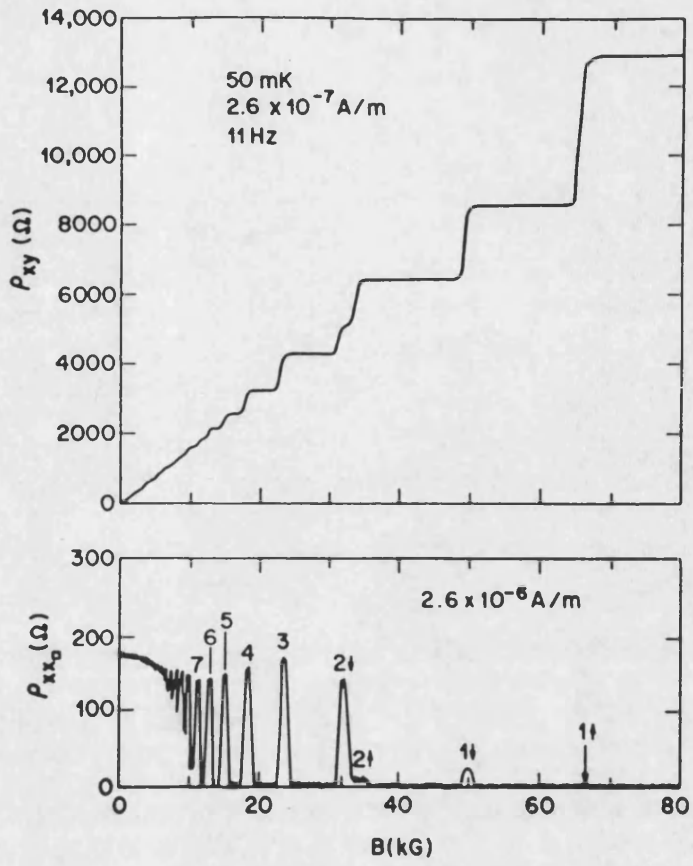

Figure 2.3: *(a) Magnetoresistance* ρ_{xx} *and (b) Hall resistance* ρ_{xy} *measured as a function of magnetic field for a GaAs/AlGaAs heterostructure at 50mK. From Paalenen et al* [5].

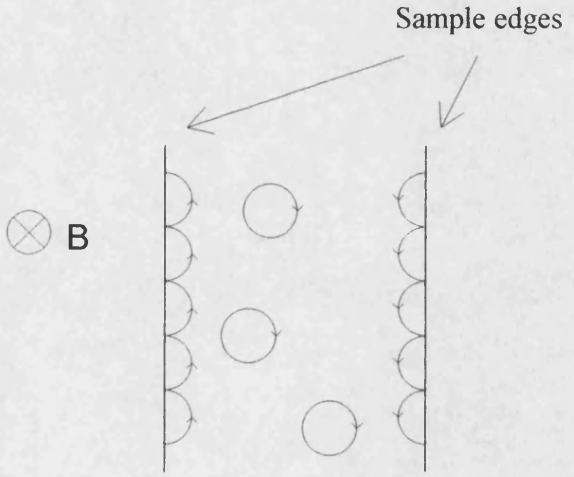

Figure 2.4: *Current flow via skipping orbits at the edge of a Hall bar sample in a high magnetic field. Orbits in the centre of the sample are localised in the quantum Hall plateau regime.*

2.2.4 The Quantum Hall Effect

In *Figure 2.3b* the measured Hall resistance is also plotted as a function of magnetic field. The Hall resistance, which is best described as a set of plateaux separated by steep rises, contrasts starkly with the classical Hall resistance which is a linear function of magnetic field. The resistance at the plateaux, which occur at integer filling factors, is precisely quantised in units of h/e^2 whatever the sample material or parameters. The first observations of these Hall resistance plateaux were made by von Klitzing et al [46] and the phenomenon is termed the Quantum Hall Effect. In a three dimensional sample the Hall voltage V_H, (the voltage developed across a sample at right angles to the current I_x when a perpendicular magnetic field B_z is applied) is:

$$V_H = -\frac{B_z I_x}{nde} \tag{2.28}$$

where n is the carrier density, d the sample thickness and e the electronic charge. In a 2D system the sheet carrier concentration n_{2D} is defined by the product nd so that Hall resistance becomes:

$$R_H = \frac{B_z}{n_{2D}e} \tag{2.29}$$

At integer filling factors the 2D carrier concentration is given by the number of electrons per Landau level multiplied by the filling factor, leading to a Hall resistance of:

$$R_H = \frac{h}{\nu e^2} \tag{2.30}$$

Clearly this predicts the quantisation of the Hall resistance, but only at magnetic fields at which the uppermost Landau level is fully occupied, and the existence of plateaux of constant resistance is not explained. By returning to the concept of localised and

extended states in the Landau levels a simple description of the plateaux can be made. Only current carrying states (extended) can contribute to the Hall resistance, and so in the region between Landau levels where only localised states exist the Hall resistance would be expected to be constant. While this does explain the existence of the plateaux it does not explain why the resistance should be quantised at h/e^2 as the localised states cannot carry current and should not influence the Hall resistance (localised states are also sample dependent as they are related to disorder).

One model that predicts both the plateaux and their resistance value is based on *edge states* or *edge channels*. When the finite size of the sample is to taken into to account it is found that one-dimensional electron states exist at the edges of the samples with increased energy eigenvalues compared with states in the centre of the sample. Classically these edge states correspond to cyclotron orbits that skip along the sample boundary, colliding elastically with the edge potential, *Figure 2.4*. Unless the magnetic field is such that the Fermi level is situated in the middle of a Landau level the only empty states that exist at the Fermi level, which are needed to carry current, are at the edges of the sample. Many experiments [47] indicate that most of the Hall current flows around the perimeter of the sample in the edge states (although this has yet to be experimentally demonstrated unequivocally). When the Landauer-Büttiker formulism [48] (which models the resistance of a muliterminal conductor in quantum terms) is used to describe the current flowing in the edge states both the plateaux and their resistance values are predicted.

2.3 One Dimensional Systems

2.3.1 Quantum Wires

Adding an extra degree of confinement to a 2D system transforms it into a one-dimensional (1D) system. Semiconductor structures in which electrons are confined in two dimensions are often called quantum wires, in which the electrons form a one-dimensional gas (1DEG). In a quantum wire the electron energy is quantised in two dimensions, and the total electron energy is the combination of these levels with the unrestricted energy in the third direction. If the extra electrostatic confinement is in the x-direction and the free translational motion is in the y-direction then the Hamiltonian becomes:

$$\hat{H} = \frac{\hat{P}_y^2}{2m^*} + V_E(x) + V_E(z) \tag{2.31}$$

where $V_E(x)$ and $V_E(z)$ are the confining electrostatic energy terms. If $V_E(x)$ is sufficiently strong the energy spectrum will consist of well separated discrete subbands E_n^0. The total electron energy will therefore consist of the translational motion in the y-direction and the quantised energies E_n^0 and E_p in the x and z directions respectively:

$$E_{n,p}^0(k_y) = E_n^0 + \frac{\hbar^2 k_y^2}{2m^*} + E_p \tag{2.32}$$

In a 1D system each electron state now occupies a length in momentum space of $2\pi/L$ where L is the length of the system. Therefore in a line of momentum of length $2k$ (+/-) the number of electrons N_e is given by:

$$N_e = 4k\frac{L}{2\pi} \tag{2.33}$$

allowing for spin. Using $k^2 = 2m^*E/\hbar^2$ the number of electrons per unit length n becomes:

$$n = \frac{N_e}{L} = \frac{2}{\pi}\left(\frac{2m^*}{\hbar^2}\right)^{1/2} E^{1/2} \tag{2.34}$$

The density of states per unit energy, $\partial n/\partial E$, for one 1D subband now contains characteristic $E^{-1/2}$ singularities:

$$\frac{\partial n}{\partial E} = \frac{1}{\pi\hbar}\left(\frac{2m^*}{E}\right)^{1/2} \tag{2.35}$$

The total density of states $D_{1D}(E)$ (if m^* is independent of energy) is the sum over all subbands:

$$D_{1D}(E) = \frac{1}{\pi\hbar}(2m^*)^{1/2}\sum_n \frac{1}{(E-E_n^0)^{1/2}}\theta(E-E_n^0) \tag{2.36}$$

where θ is the Heaviside step function (Eqn. 2.8). The total DOS is shown schematically in *Figure 2.5*. The number of electrons per unit length, N_e^{1D} can be calculated by summing over the subbands to the Fermi energy:

$$N_e^{1D} = \frac{2}{\pi\hbar}\sum_n \left[2m^*\left(E_F - E_n^0\right)\right]^{1/2}\theta(E_F - E_n^0) \tag{2.37}$$

In a semiconductor quantum wire exact solutions of the 1D wavefunctions again requires a self-consistent solution. However the extra degree of electrostatic confinement in a quantum wire can often be modelled as a parabolic potential in x:

$$V_E(x) = \tfrac{1}{2}m^*\omega_0^2 x^2 \tag{2.38}$$

where ω_0 is some constant of the wire (dependent on wire width). In reality the actual potential is likely to be parabolic only for narrow wires and low electron concentrations, but for many purposes this is an acceptable starting point which can then be later refined

in the light of experimental data, see for example; [49]. In zero magnetic field the total energy of the electrons is therefore:

$$E_{n,j,y} = \hbar\omega_0(n+\tfrac{1}{2}) + \frac{\hbar^2 k_y^2}{(2m^*)} + E_p \tag{2.39}$$

and the total wavefunction is of the form:

$$\Psi(x,y,z) = \left(1/\sqrt{L}\right)e^{ik_y y}\phi_n(x)\xi_p(z) \tag{2.40}$$

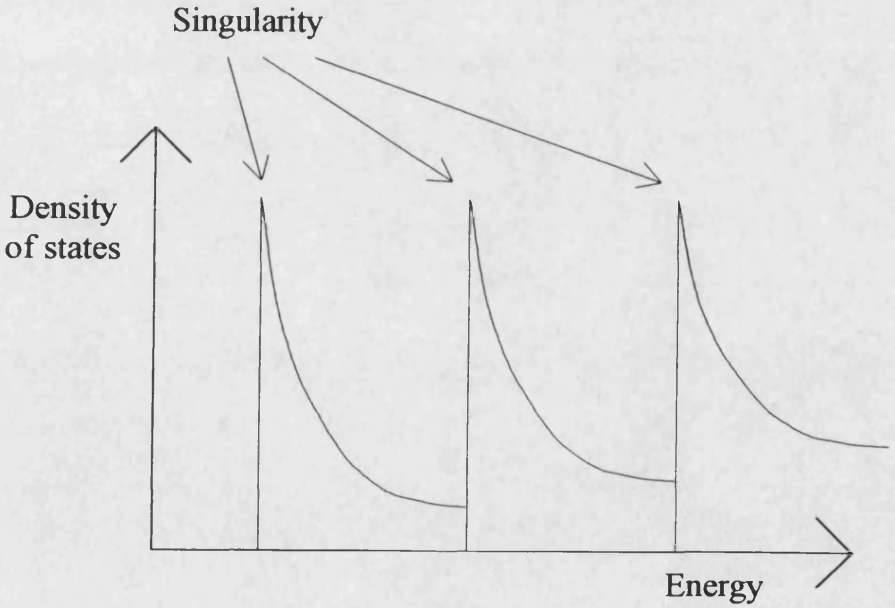

Figure 2.5: *The density of states, per unit area and per unit energy, for a 1D system*

2.3.2 Properties in a Perpendicular Magnetic Field

In a magnetic field (perpendicular to the original 2DEG) the Schrödinger equation now becomes (assuming parabolic electrostatic confinement in the x-direction):

$$-\frac{\hbar^2}{2m^*}\frac{\partial^2 u}{\partial x^2}+\frac{e^2B_z^2}{2m^*}\left(x+\frac{\hbar k_y}{eB_z}\right)^2 u+\tfrac{1}{2}m^*\omega_0^2x^2u=Eu \tag{2.41}$$

which can be rearranged to:

$$-\frac{\hbar^2}{2m^*}\frac{\partial^2 u}{\partial x^2}+\frac{e^2B_z^2}{2m^*}(x-x_0)^2u+\tfrac{1}{2}m^*\omega_0^2x^2u=Eu \tag{2.42}$$

where $x_0=\dfrac{\hbar k_y}{eB_z}$ and is the centre of motion. This is the equation for a harmonic oscillator and can be simplified and rearranged to give an expression for the total energy (excluding spin splitting terms) of the electron in a quantum wire in a magnetic field:

$$E=\tfrac{1}{2}m^*\left(\frac{\omega_c^2\omega_0^2x_0^2}{\omega_c^2+\omega_0^2}\right)+\left(n+\tfrac{1}{2}\right)\hbar\sqrt{\left(\omega_c^2+\omega_0^2\right)}+E_p \tag{2.43}$$

In the case when the electrostatic confinement of the wire is parabolic the density of states remains the same as in zero magnetic field provided that m^* is replaced by $m^*(\omega/\omega_0)^2$ and $\hbar\omega_0(n+\frac{1}{2})$ is replaced by $\hbar\omega(n+\frac{1}{2})\,(=E_n(B))$ where ω is defined by:

$$\omega=\sqrt{\left(\omega_c^2+\omega_0^2\right)} \tag{2.44}$$

However, the DOS becomes more sharply peaked in the presence of a magnetic field due to the heavier effective mass. At high magnetic fields, when $\omega_c \rangle\rangle \omega_0$, the electronic structure in the Landau levels is essentially that as in the 2DEG, whereas at low magnetic fields they differ strongly due to the extra electrostatic confinement; *Figure 2.6.*

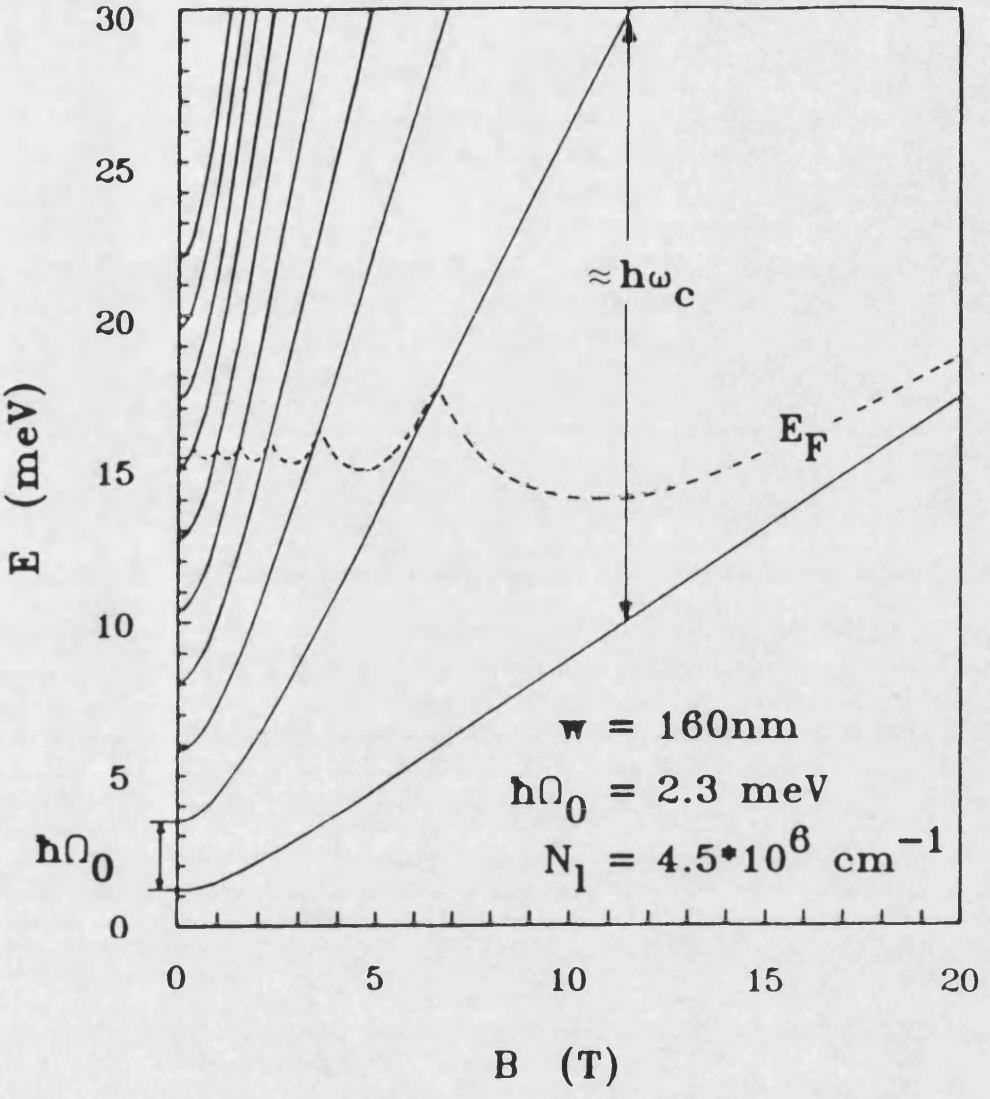

Figure 2.6: *Single particle energy spectrum for an electron confined in a quantum wire, having a confinement* $V_{Conf}(x) = \frac{1}{2}m^*\Omega_0^2 x^2$, *with an effective with of 160nm. Note that at high magnetic fields the energy separation of the levels tends to* $\hbar\omega_c$, *the 2D separation. From Heitmann [35].*

2.3.3 Magnetic Depopulation of 1D Subbands

In an increasing magnetic field the separation between the 1D magnetic subbands increases so that with a fixed number of electrons in the wires less and less subbands are occupied. This is known as the magnetic depopulation of subbands and at low temperatures there are oscillations in the measured longitudinal magnetoresistivity along the wires that reflect the density of states at the Fermi energy and are analogous to Shubnikov-de Haas oscillations [50]; *Figure 2.7.* When a particular subband n is just depopulated the Fermi energy lies at the bottom of the highest occupied subband, so that $E_F = E_n$. Replacing m^* by $m^*(B)$ and E_n^0 by $E_n(B)$ we can modify the zero field expression for the number of electrons N_e^{1D} to:

$$N_e^{1D} = \frac{2}{\pi}\left(2m^*/\hbar\right)^{1/2}\left(\omega^{1/2}/\omega_0\right)\sum_{\alpha=1}^{n}\alpha^{1/2} \tag{2.45}$$

when the nth subband is just being depopulated. This can be rearranged to:

$$B_z^2 = \left(\frac{m^*}{e}\right)^2\left(\frac{N_e^{1D}\omega_0\pi}{2}\right)^{1/3}\left(\frac{2\hbar}{m^*}\right)^{2/3}\left(\sum_{\alpha=1}^{n}\alpha^{1/2}\right)^{-4/3} - \omega_0^2\left(\frac{e}{m^*}\right)^2 \tag{2.46}$$

There is no longer a simple linear relationship between filling factor ν and reciprocal magnetic field as in the 2D case. However, N_e^{1D} and ω_0 can be determined from a linear fit of B_z^2 to $\left(\sum_{\alpha=1}^{n}\alpha^{1/2}\right)^{-4/3}$.

At high magnetic fields, when the cyclotron orbit size is smaller than the electrostatic confinement, the 1D subbands tend towards 2D Landau levels and the filling factor ν and inverse magnetic field are again approximately linearly related.

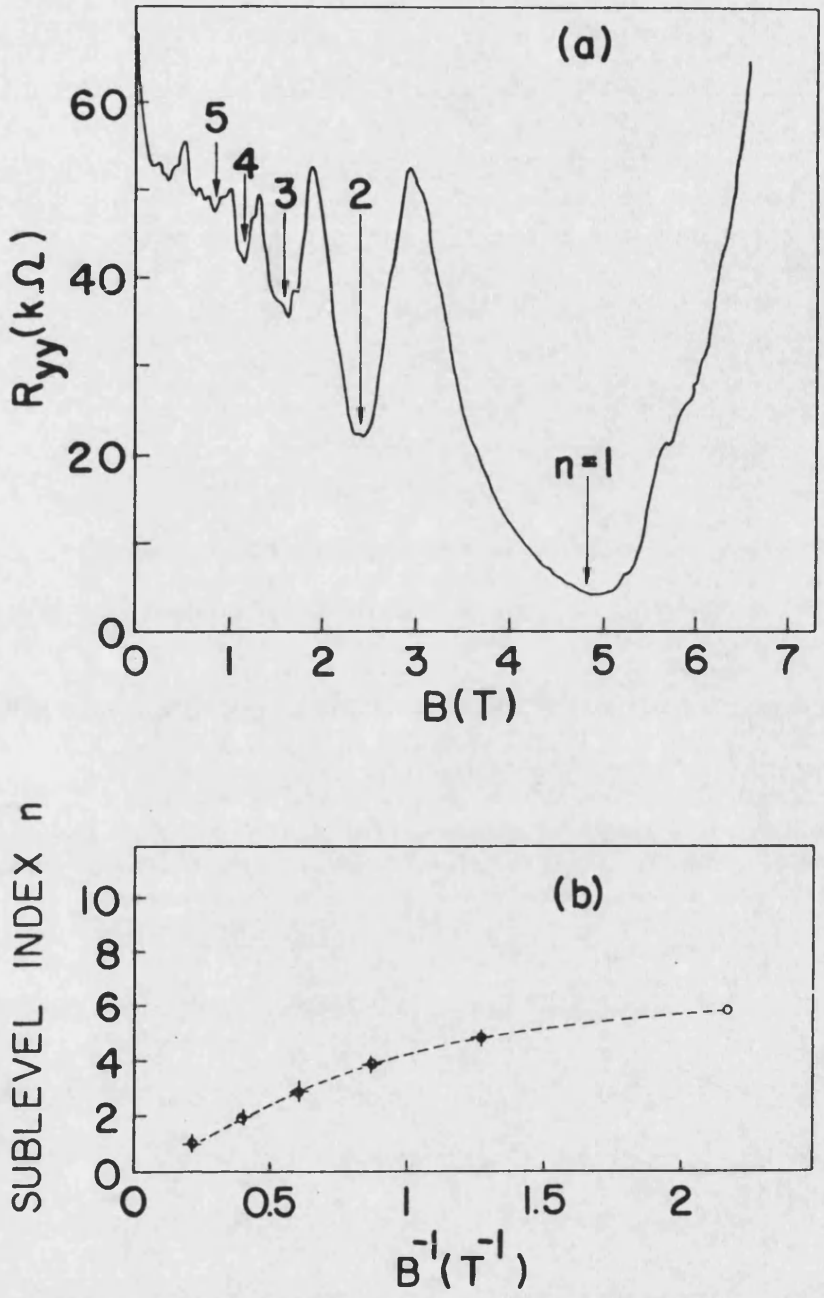

Figure 2.7: *(a) Measured magnetoresistance at 2.4 K in an etched AlGaAs/GaAs mesa structure of nominal width 0.5μm (the conducting channel is along the y-axis). Arrows indicate the magnetic depopulation of subbands. (b) Sublevel index n vs inverse magnetic field. Crosses refer to minima in the measured magnetoresistance in (a) and circles to theoretical results. From Berggren et al [50].*

2.4 Zero Dimensional Systems

Complete confinement of electrons and holes produces zero-dimensional systems, and semiconductor structures in which this occurs are often known as quantum dots. The complete confinement means that the electron states are discrete rather than occurring in bands (quantum dots are therefore sometimes called artificial atoms), and the electronic density of states is a series of delta functions.

2.4.1 Single Electron Properties

The spacing of the energy levels, and the electron wavefunctions, are determined by the exact shape of the confining potential, which is itself determined by the electron density so that a self consistent approach is again needed. Additionally with only a small number of electrons in each dot (typically from a few to a few hundred) the role of electron-electron interactions cannot be ignored (see next section). However, the confining potential is often simply modelled as parabolic, having the form $V_{conf} = \frac{1}{2}m^*\omega_0^2 r^2$, where r is the distance from the centre of the dot (compared with the $1/r$ dependence of the core potential of real atoms) and the single electron energy levels have been calculated in a magnetic field B by Fock (1928) [51]:

$$E_{m,l} = \left(2m + |l| + 1\right)\sqrt{\left(\hbar\omega_0\right)^2 + \left(\frac{\hbar\omega_c}{2}\right)^2} + l\left(\frac{\hbar\omega_c}{2}\right) \qquad (2.47)$$

where $m = 0, 1, 2, \ldots$ and $l = 0, \pm1, \pm2, \ldots$ are the radial and azimuthal quantum numbers respectively. This single electron energy spectrum is shown in *Figure 2.8,* for a

confinement potential $\hbar\omega_0$=3.3meV. The wavefunctions have the form (apart from a normalisation constant):

$$\varphi(\mathbf{r}) = r^{|l|}e^{-il\theta}L_n^{|l|}\left(r^2/2a^2\right)e^{\left(-r^2/4a^2\right)} \tag{2.48}$$

where $L_n^{|l|}$ is a Laguerre polynomial, and $a^2 = \left(\hbar/m^*\right)\left(\omega_c^2 + 4\omega_0^2\right)^{-1/2}$.

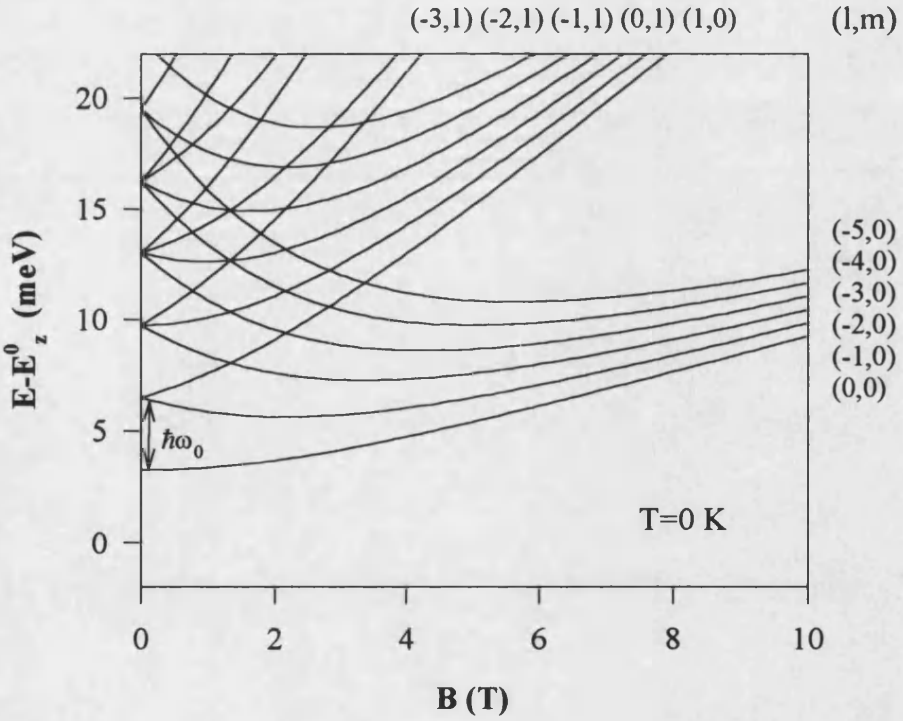

Figure 2.8: *Single particle energy levels calculated for an electron in a quantum dot, with confining potential* $V_{Conf}(r) = \frac{1}{2}m^*\omega_0^2 r^2$, *where r is the distance from the centre of the dot, and* $\hbar\omega_0$ *=3.3meV.*

2.5 Plasmons and Screening

The simplest plasmon to consider is the three dimensional (3D) plasmon that can be excited in bulk 3D metals. This can be described by imagining shifting the entire electron gas with respect to the fixed positive background of the ions, leaving a positive charge density of *neu* at one end of the sample and a negative charge density of *-neu* at the other, where *n* is the electron concentration, and *u* the displacement of the electron gas. An electric field *E* is thus developed and the electron gas as a whole obeys the equation of motion:

$$nm\frac{d^2u}{dt^2} = -neE = -\frac{n^2e^2u}{\varepsilon_0} \tag{2.49}$$

where *m* is the electronic mass. This can be written as:

$$\frac{d^2u}{dt^2} = +\omega_p^2 u = 0 \tag{2.50}$$

where $\omega_p = \left(\frac{ne^2}{\varepsilon_0 m}\right)^{1/2}$, and is the equation of motion of a simple harmonic oscillator of frequency ω_p, the plasma frequency, and the longitudinal oscillations of the electron gas are known as plasma oscillations or dynamic excitations. A plasmon is a quantum of a plasma oscillation. The plasma frequency can also be derived by seeking the zeroes of the frequency and wavevector dependent dielectric function $\varepsilon(q,\omega)$, which imply that the electron system can support an internal electric field without any external applied electric field.

In low dimensional systems a range of plasma oscillations can be excited and the spectra of the oscillations are characteristic of the dimensionality of the system. The

elementary collective excitation in a two dimensional electron gas is the two dimensional plasmon. In a pure two dimensional system the plasmon dispersion is:

$$\omega_p^2 = \frac{n_{2D}e^2}{2\bar{\varepsilon}\varepsilon_0 m^*}q \tag{2.51}$$

where $\bar{\varepsilon} \equiv \bar{\varepsilon}(\omega, q)$ is the effective dielectric function (which depends on the surroundings) and q is the plasmon wave-vector in the plane of the 2D system. As real 2D systems have finite thickness corrections have to be made to the above dispersion relationship at long wavelengths (small wavevector). These plasma oscillations have been observed in far-infra red (FIR) absorption experiments [52]. Additionally if two 2D subbands are occupied it is possible to excite carriers from one subband to another. These intersubband resonances represent oscillations of the carriers perpendicular to the plane of the 2D system [53] and alter the pure 2D dispersion given above. Other plasmon modes, for example *linear edge plasmons*, can also be excited [54]. The application of a perpendicular magnetic field shifts the 2D plasmon frequency given above, so that the *magnetoplasmon* dispersion is: $\omega_{mp}^2 = \omega_p^2 + \omega_c^2$ [55].

In quantum wires it is possible to excite 1D plasmons propagating freely along the direction of quantum wires, single particle transitions between 1D subbands (which can be thought of as confined plasma oscillations perpendicular to the wires) and combinations of these modes [35]. The simplest way to describe the plasmons that can be excited in a quantum dot is to model the dot as a small disk of 2D system. The q-vectors are then quantised into values $q = i/R$ (i=1 , 2,...), where R is the radius of the disk, and one considers the excitation of linear edge plasmons (excitations that exist at an edge of a semi-infinite 2DEG). At zero magnetic field the dispersion is:

$$\omega_{0i}^2 = 0.81\frac{n_{2D}e^2 i}{2m^*\varepsilon_0\bar{\varepsilon}R} \tag{2.52}$$

whereas in a magnetic field there is a set of double branches:

$$\omega_{i\pm}^2 = \sqrt{\omega_{oi}^2 + \left(\frac{\omega_c}{2}\right)^2} \pm \left(\frac{\omega_c}{2}\right) \tag{2.53}$$

These relationships have been used to successfully model FIR data [56]. An extensive review of plasmon excitations in low dimensional systems is given in [35]. Most of the FIR experiments that have probed plasma excitations in these systems have been performed on arrays of quantum wires and dots where the Coulomb interaction between the structures, although not mentioned here, has to be taken into account.

Surface acoustic waves have been used to couple to 2D *edge magnetoplasmons* [57] in a two dimensional hole gas. In this experiment SAW amplitude and phase were measured as a function of magnetic field, *Figure 2.9*. The minimum in phase was associated with resonant absorption and the resonant frequency was found to have a $1/B$ dependence. This absorption was attributed to the excitation of an edge magnetoplasmon. A value of the 2D hole concentration was obtained, by modelling the charge sheet as an infinitely thin oblate spheroid, which was in reasonable agreement with the value obtained from transport measurements. It should be noted that the excitation of plasmons by SAWs requires a matching of the SAW and plasmon velocity in the long wavelength limit and was only possible in this case due to the large area of the hole gas.

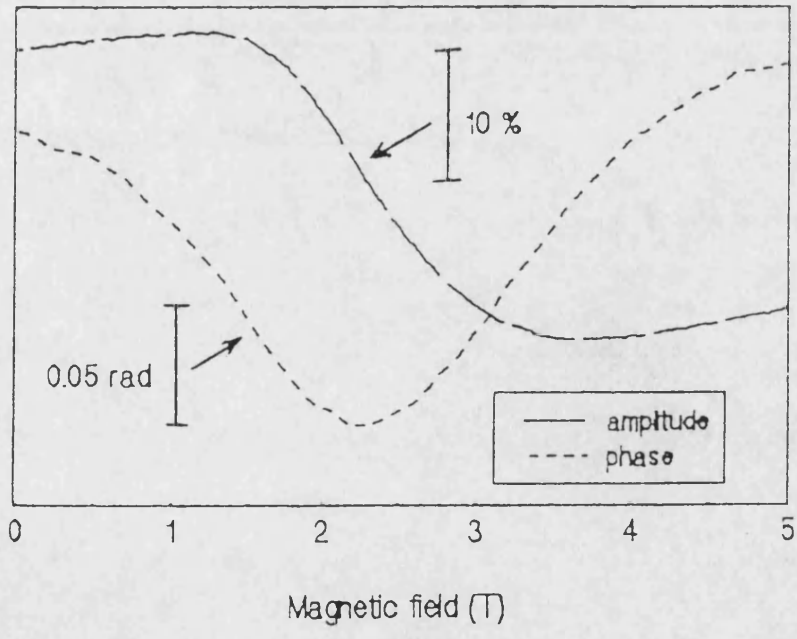

Figure 2.9: *A plot of SAW amplitude and phase as a function of magnetic field showing the excitation of an edge magnetoplasmon in a two dimensional hole gas. From Hawker et al [57].*

The plasma oscillations discussed above are the long range limit of the Coulomb interaction between electrons. Screening is the short range limit: in 3D, a fixed positive impurity charge modifies the local density of electrons so that the extra charge is partially screened out. However, the screening properties of the electron system are also affected by the dimensionality. In low dimensional systems the screening of the impurity charge is thought to be progressively less effective due to the restricted possibilities of confined electrons to move and screen the additional charge.

2.6 Many Body Effects

So far the effects of electron-electron interactions have only been mentioned in passing. However, in low dimensional systems these many body effects can be highly significant and a few important examples of many body effects are briefly outlined below.

In magnetotransport measurements in two dimensional systems plateaux are seen in the Hall voltage, and zeroes in the longitudinal resistance, *Figure 2.10*, at magnetic fields at which all the electrons are in the lowest Landau level and therefore no further plateaux expected. These plateaux occur at fractional filling factors and the phenomenon is termed the Fractional Quantum Hall Effect [6]. Near ½ filling factor it is thought that the strong electron-electron interaction causes the formation of quasiparticles of composite fermions [58]. Self consistent solutions for quasi 1D electron states in a split-gate AlGaAs/GaAs heterostructure [59], where a metal gate is used to define a 1D channel, show that the 1D subband spacing decreases with increasing electron concentration due to self-consistent screening. In quantum dots containing few electrons there are two competing energies; the kinetic energy of the electrons and the interaction

energies (e.g Coulomb repulsion between electrons). These many body effects not only alter the zero magnetic field single electron energy level spacings in quantum dots, but also their magnetic field spectrum, and the magnetic field dependence of the chemical potential contains fine structure which is due to these many body effects [60].

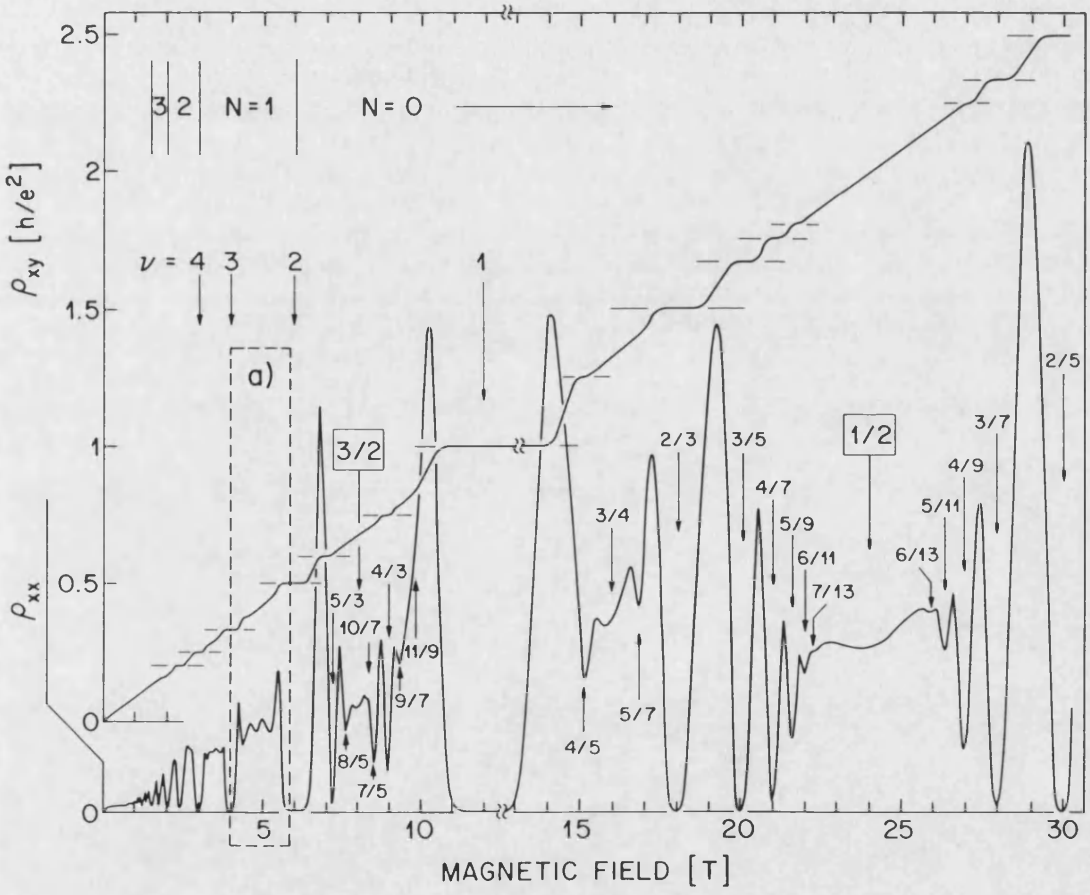

Figure 2.10: *The fractional quantum Hall effect, showing evidence of a rich variety of many body phenomena in a 2DEG in a high magnetic field. From Willet et al [6].*

3 Surface Acoustic Waves and their Properties

3.1 Surface Acoustic Waves

3.1.1 Introduction and General Properties

The properties of Surface Acoustic Waves (SAWs) have been investigated since Lord Rayleigh in 1855 delivered the first mathematical discussion on the propagation of waves on the plane free surface of a homogeneous isotropic elastic solid in an address to the London Mathematical Society [61]. These studies were found to be of particular relevance to the description of seismic waves. Early electronic acoustic wave devices actually employed bulk waves, for example in a simple delay line where bulk waves propagate in an elastic medium between two transducers. The invention of the Interdigital Transducer (IDT) in 1965 by White and Voltmer [62] made it possible to excite SAWs directly on the surface of piezoelectric crystals. Due to the many advantages of SAW devices, particularly the slow SAW velocity compared to electro-magnetic signals and the ability to access the signal during propagation, their exploitation in a large range of analogue signal processing then followed [12,63]. In addition SAWs are now used in a vast range of sensor applications [64]. The chapter begins with a description of the classical elastic behaviour of bulk crystals, which leads into brief a introduction to the properties of SAWs, with particular reference to their propagation in piezoelectric materials. SAW-electron scattering is then discussed in both classical and quantum mechanical terms. The chapter concludes with a short section on the excitation of SAWs via interdigital transducers.

3.1.2 Bulk Acoustic Waves in Isotropic Crystals

Elasticity is concerned with the internal forces within a solid and the related displacement of the solid from its equilibrium, or force-free configuration. The forces exerted on an infinitesimal volume of the solid, which is assumed to be homogeneous, are expressed as a symmetrical stress tensor with components T_{ij}, where T_{ij} is the component along the x_i direction of the force per unit area acting on a surface normal to the x_j direction. Newton's third law can be used to derive the wave equation:

$$\rho \frac{\partial^2 u_i}{\partial t^2} = \frac{\partial T_{ij}}{\partial x_j} \tag{3.1}$$

where u_i are the displacement components of the volume parallel to the directions x_i, and ρ is the mass density. Here a repeated subscript in a term implies that the term is summed over the values of the repeated index, for example:

$$\frac{\partial T_{ij}}{\partial x_j} = \frac{\partial T_{i1}}{\partial x_1} + \frac{\partial T_{i2}}{\partial x_2} + \frac{\partial T_{i3}}{\partial x_3} \tag{3.2}$$

In an elastic medium the stress is a linear function of the strain:

$$T_{ij} = c_{ijkl} S_{kl} \qquad \text{i, j, k, l = 1, 2, 3.} \tag{3.3}$$

where c_{ijkl} is the elastic stiffness, which is a fourth rank tensor having eighty one components. However, the symmetry of c_{ijkl} in the first two and the last two suffixes ($c_{ijkl} = c_{jikl}$, $c_{ijkl} = c_{ijlk}$) makes it possible to write the elastic stiffness as a (6 x 6) matrix where the first two suffixes of the fourth rank tensor are abbreviated into a single one running from 1 to 6, and the last two are abbreviated in the same way, according to the scheme [65]:

tensor notation	11	22	33	23, 32	31, 13	12, 21
matrix notation	1	2	3	4	5	6

In cubic crystals the number of elements is further reduced, by symmetry, to three: c_{11}, c_{12} and c_{44}, as compared to an isotropic medium in which there are only two independent elements as $2c_{44} = c_{11} - c_{12}$.

In an infinite isotropic crystal there are always three plane wave solutions to the wave equation: one longitudinal wave and two shear or transverse waves. The phase velocities of the two waves are:

$$V_{transverse} = \sqrt{c_{44}/\rho} \tag{3.4}$$

$$V_{longitudinal} = \sqrt{c_{11}/\rho} \tag{3.5}$$

The velocities of these waves are independent of the direction of propagation, the velocity of the longitudinal waves always being greater than the transverse ones. Note also that the velocities of these long wavelength acoustic waves are independent of the frequency. An alternative approach is to consider the simple harmonic oscillations of the individual atoms, or planes of atoms, in the solid [66]. In the long wavelength limit such an approach also yields that the sound velocity is independent of frequency (non-dispersive).

3.1.3 Bulk Acoustic Waves in Anisotropic and Piezoelectric crystals

In an anisotropic crystal all the properties of the wave depend on the direction of propagation. In a cubic crystal the velocity of bulk longitudinal waves along a crystal axis is the same as in the isotropic case while on the same axes there are again two

degenerate shear waves with velocities also as above. In general, however, the velocities are different for other directions of propagation. For example for a wave propagating in the [110] axis in a cubic solid the two shear velocities are nondegenerate having velocities:

$$V_{t1} = \sqrt{c_{44}/\rho} \tag{3.6}$$

$$V_{t2} = \sqrt{c_{44}/\eta\rho} \tag{3.7}$$

where $\eta = \dfrac{2c_{44}}{c_{11} - c_{12}}$ and is a measure of the anisotropy. The longitudinal velocity is given by:

$$V_{longitudinal} = \sqrt{(c_{11} + c_{12} + 2c_{44})/2\rho} \tag{3.8}$$

In GaAs these velocities have been measured as 3345 m/s, 2476 m/s and 5238 m/s respectively at 300K [67]. So far the effects of piezoelectricity have been ignored. In a piezoelectric material (which has to lack a centre of symmetry), such as GaAs, the application of stress T_{ij} produces not only strain but also an electric field, which can be represented by a time varying scalar potential φ:

$$T_{ij} = c_{ijkl} S_{kl} + e_{kij} \frac{\partial \varphi}{\partial x_k} \qquad (i, j, k, l = 1, 2, 3) \tag{3.9}$$

or in terms of the particle displacement:

$$T_{ij} = c_{ijkl} \frac{\partial u_k}{\partial u_l} + e_{kij} \frac{\partial \varphi}{\partial x_k} \tag{3.10}$$

where e_{kij} is the piezoelectric tensor having 27 components. However, it is possible to write the piezoelectric constant as a (3 x 6) matrix, where the first suffix is the same in both notations, and the second and third suffixes in the tensor notation are replaced in the new notation by a single suffix running from 1 to 6 as follows:

tensor notation	11	22	33	23, 32	31, 13	12, 21
matrix notation	1	2	3	4	5	6

In a cubic crystal there is only one independent element e_{14}. Here the elastic stiffness is measured at constant electric field. The modified relationship for the stress leads to a new wave equation:

$$\rho\frac{\partial^2 u_j}{\partial t^2} = c_{ijkl}\frac{\partial^2 u_k}{\partial x_i \partial x_l} + e_{kij}\frac{\partial^2 \varphi}{\partial x_k \partial x_i} \tag{3.11}$$

The electric displacement D also contains a mechanical coupling term:

$$D_i = -\varepsilon_{ij}\frac{\partial \varphi}{\partial x_j} + e_{ijk}\frac{\partial u_j}{\partial x_k} \tag{3.12}$$

where ε_{ij} is the dielectric tensor at constant strain which has six independent elements, reduced to one in isotropic and cubic crystals. In a piezoelectric insulator $\underline{\nabla}.\underline{D} = 0$ and hence:

$$\varepsilon_{ik}\frac{\partial^2 \varphi}{\partial x_i \partial x_k} = e_{ikl}\frac{\partial^2 u_k}{\partial x_i \partial x_l} \tag{3.13}$$

The solutions to these equations are plane waves both for the particle displacement and the electric potential, and therefore the associated electric field. The electric potential and field are not electromagnetic but are a component part of the predominantly mechanical wave and can be thought of as electrostatic in nature as elastic disturbances travel much more slowly than electromagnetic ones. The effect of the piezoelectricity is to increase the elastic constants by the factor $\left(1+K^2\right)$ where K^2 is given by:

$$K^2 = \frac{e^2_{piezo}}{c\varepsilon} \tag{3.14}$$

K^2 is known as the piezoelectric coupling coefficient and is a measure of the piezoelectricity of the solid. Note that the tensor subscripts have been dropped in the above, as appropriate constants depend on the direction of propagation. Piezoelectricity therefore increase the wave velocity, an effect known as piezoelectric stiffening. For GaAs the strongest piezoelectric coupling occurs for a shear wave propagating in the [110] direction [68], with a coupling coefficient of:

$$K_{14}^2 = \frac{e_{14}^2}{\varepsilon c_{14}} \approx 0.06 \tag{3.15}$$

where the dielectric constant $\varepsilon = \varepsilon_0 . \varepsilon_r$.

3.1.4 Surface Acoustic Waves in Isotropic Crystals

If the crystal is not infinite in extent, but is bounded by a plane, then surface waves can propagate at the free surface. Ignoring piezoelectricity for the moment, solutions to the wave equation are sought which decay with depth below the surface, the defining feature of a surface wave, and which are "straight-crested"; in that there is no dependence of the displacement, at any depth, on the distance measured from the sagittal plane (where the sagittal plane is the plane perpendicular to the free surface and containing the propagation vector). The solutions to the wave equation also have to satisfy the boundary condition that the stress on the free surface be zero. In isotropic crystals the surface wave solution is a combination of shear and longitudinal partial waves (it should also be noted that a bulk shear wave travelling parallel to the surface also is a solution) and the particle displacements are elliptical, with the shape of the ellipse changing as a function of depth; *Figure 3.1*. The amplitude of the disturbance becomes negligible for

depths more than a few wavelengths from the surface and the particle displacement is confined to the sagittal plane. Surface waves of this form are known as Rayleigh waves. The surface wave velocity v_{sw} can be calculated from [69]:

$$\left[2-\left(\frac{v_{sw}}{v_{transverse}}\right)^2\right]^2 = 4\left[1-\left(\frac{v_{sw}}{v_{longitudinal}}\right)^2\right]^{1/2}\left[1-\left(\frac{v_{sw}}{v_{transverse}}\right)^2\right]^{1/2} \tag{3.16}$$

The phase velocity can then be approximated by:

$$\frac{v_{sw}}{v_{transverse}} \cong \frac{0.72-\left(v_{trans.}/v_{long.}\right)^2}{0.75-\left(v_{trans.}/v_{long.}\right)^2} \tag{3.17}$$

The surface wave therefore has a lower velocity than the lowest bulk-wave velocity, and its wavelength measured along the surface is greater than the projected wavelength of any bulk wave propagating at any angle to the surface. As a result the surface wave on a free isotropic surface cannot phase match to any bulk wave.

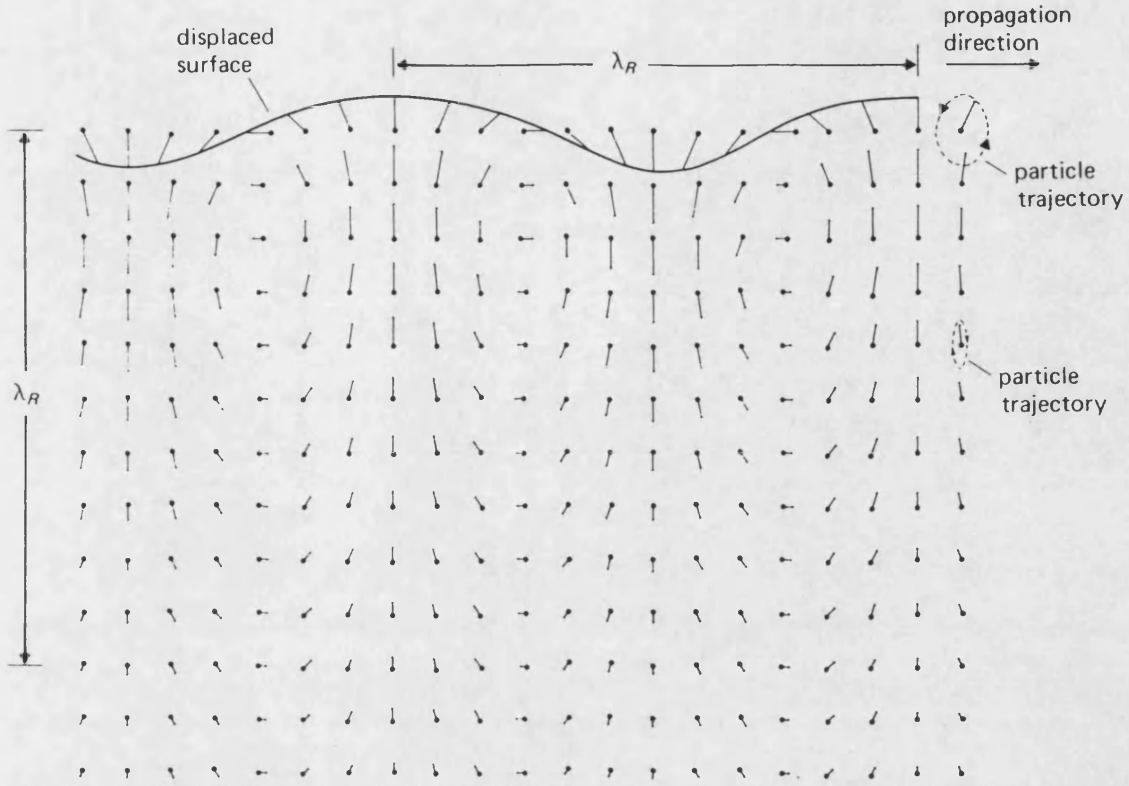

Figure 3.1: *Instantaneous displacements for Rayleigh wave propagation in isotropic material. From Morgan [63].*

3.1.5 Surface Acoustic Waves in Anisotropic and Piezoelectric Crystals

Because of algebraic complexity, numerical techniques usually have to be used to calculate the phase velocities and corresponding particle displacements for waves in anisotropic crystals. The properties of the surface wave now depend both on the free surface and on the direction of propagation. For a wave propagating exactly in the [110] direction on the (001) (or basal) plane of a cubic crystal there is a surface wave solution having a phase velocity given by [68]:

$$c_{11}\left(v_{sw}^2-\frac{c_{44}}{\rho}\right)\left(v_{sw}^2-\frac{2c_{44}+c_{12}+c_{11}}{2\rho}+\frac{c_{12}^2}{c_{11}\rho}\right)^2 = c_{44}v_{sw}^2\left(v_{sw}^2-\frac{2c_{44}+c_{12}+c_{11}}{2\rho}\right) \tag{3.18}$$

In this case the particle displacements are, as in the isotropic case, both elliptical and confined to the sagittal plane. At a few degrees from [110] there is a leaky, or pseudo, surface wave solution in which energy is radiated into the bulk of the crystal [69].

When piezoelectricity is included the solutions to the wave equation now have to satisfy the extra boundary conditions that the normal component of the electric displacement at the surface is continuous and that the tangential electric field is continuous, if there are no free charges. For [110] propagation on the (001) surface of GaAs the surface wave solution is a pure stiffened Rayleigh wave [70]. The electric potential associated with this wave, which extends above and into the crystal surface, is confined to the saggital plane, so that there are electric field components normal to the surface and in the direction of propagation. The electric potential decays to zero inside the crystal within approximately one wavelength (depending on the electrical properties of the free surface). In semi-insulating GaAs the room temperature SAW velocity has

been measured as 2841m/s [71], intermediate between the two bulk shear (transverse) wave velocities. An effective piezoelectric coupling coefficient is defined as:

$$\frac{K_{eff}^2}{2} = \frac{v_{sw} - v_{shorted}}{v_{sw}} \tag{3.19}$$

where $v_{shorted}$ is the surface wave velocity for a shorted (or metallised) surface. In GaAs K_{eff}^2 has a value of 6.4×10^{-4} [71], at room temperature. It should be noted that these stiffened Rayleigh waves are non-dispersive (velocity is independent of frequency), which is of great technological importance.

3.2 Classical Description of the SAW-Electron Interaction

3.2.1 Overview

The discussion of piezoelectric stiffening, where some of the elastic energy of an acoustic wave is transferred to the accompanying electric field, has so far been confined to piezoelectric insulators (or poor conductors). However, for an acoustic wave propagating in a very good piezoelectric conductor, with conductivity approaching infinity, the internal electric fields have to vanish. In this case the wave propagates as though in a non-piezoelectric material, with a reduced velocity compared to a piezoelectric insulator. Additionally the currents that flow whilst the electric field is being screened will be of short duration, and the Ohmic losses, and hence attenuation, associated with them will be small. In a piezoelectric insulator there are no such currents and Ohmic losses. At some finite conductivity currents will flow for the whole time between wavecrests to screen the electrostatic electric field of the acoustic wave. Ohmic

losses will therefore be at a maximum, and the wave velocity will be at an intermediate value. The development and limits of this classical model, and the modifications needed to apply it to SAWs will be briefly outlined.

3.2.2 Relaxation Model for Bulk Waves

To derive expressions for the attenuation and velocity shift of a SAW due to the piezoelectric interaction with conduction electrons we begin by considering the bulk wave case. This description follows closely that given by McFee [72] and Hutson and White [73]. Poisson's equation, the Continuity equation and an expression for the current density in one dimension are given by:

$$\frac{\partial D}{\partial x} = -en \tag{3.20}$$

$$\frac{\partial J}{\partial x} = e\frac{\partial n}{\partial t} \tag{3.21}$$

$$J = e(n_0 + n)\mu E + e\mathcal{D}\frac{\partial n}{\partial x} \tag{3.22}$$

where J is the current density, e the electronic charge, μ the electron mobility, $\mathcal{D}$ the electron diffusion constant, n_0 is the equilibrium density of electrons (with no acoustic wave) and n is the variation in conduction electrons caused by the acoustic wave. Equations (3.20), (3.21) and (3.22) can be combined to relate D and E:

$$\frac{\partial^2 D}{\partial x \partial t} = -en_0\mu\frac{\partial E}{\partial x} + \mu\frac{\partial D}{\partial x}\frac{\partial E}{\partial x} + \frac{\partial^2 D}{\partial x^2}\mu E + \mathcal{D}\frac{\partial^3 D}{\partial x^3} \tag{3.23}$$

The wave equation (Eqn.3.11) can be rewritten as:

$$\rho\frac{\partial^2 u}{\partial t^2} = c\frac{\partial^2 u}{\partial x^2} - e_{piezo}\frac{\partial E}{\partial x} \tag{3.24}$$

where ω is the acoustic frequency. Solutions can be found of the form:

$$E = E_0 e^{i(qx-\omega t)} \tag{3.25}$$

$$D = D_0 e^{i(qx-\omega t)} \tag{3.26}$$

Substitution of Eqns. (3.25) and (3.26) into Eqn. (3.23) gives D as a function of E:

$$D = \frac{-i(n_0 \mu e/\omega)E}{(2\mu q/\omega)E + 1 + i(q^2/\omega)\mathcal{D}} \tag{3.27}$$

The term $(2\mu q/\omega)E$ can be ignored if the acoustic velocity is much greater than the drift velocity giving:

$$D = \frac{-i(\sigma/\omega)E}{1 + i(q^2/\omega)\mathcal{D}} \tag{3.28}$$

The strain S can therefore be described in terms of the electric field E using Eqn.3.13:

$$S = \frac{\varepsilon E}{e_{piezo}}\left[\frac{-i(\sigma/\omega)/\varepsilon - \left[1 + i\omega(q/\omega)^2\mathcal{D}\right]}{1 + i\omega(q/\omega^2)\mathcal{D}}\right] \tag{3.29}$$

Substituting for the electric field E in the wave equation leads to a new wave equation with modified elastic constant:

$$\rho\frac{\partial^2 u}{\partial t^2} = c'\frac{\partial^2 u}{\partial x^2} \tag{3.30}$$

$$c' = c\left(1 + \frac{e_{piezo}^2/\varepsilon c}{1 + \dfrac{i(\sigma/\omega)/\varepsilon}{1 + i\omega(q/\omega)^2\mathcal{D}}}\right) \tag{3.31}$$

Note that this relationship now includes the effect of the conductivity of the crystal. The above can be simplified using the following definitions for the conductivity relaxation frequency ω_σ and the electron diffusion frequency ω_D:

$$\omega_\sigma = \frac{n_0 e\mu}{\varepsilon} = \frac{\sigma}{\varepsilon} \tag{3.32}$$

$$\omega_D = \frac{v^2}{\mathcal{D}} \tag{3.33}$$

where v is the acoustic wave velocity. This leads to:

$$c' = c\left\{1 + \frac{e_{piezo}^2}{c\varepsilon}\left[\frac{1+(\omega_\sigma/\omega_D)+(\omega/\omega_D)^2 - i(\omega_\sigma/\omega)}{1+2(\omega_\sigma/\omega_D)+(\omega/\omega_D)^2+(\omega_\sigma/\omega)^2}\right]\right\} \tag{3.34}$$

The interaction between the wave and the electrons is small in absolute terms and the energy loss of the wave can therefore be characterised as an attenuation coefficient per unit length α:

$$q = \frac{\omega}{v} + i\alpha \qquad \text{where: } |\alpha| \langle\langle \frac{\omega}{v} \tag{3.35}$$

The new wave equation (3.30) can thus be solved by substituting:

$$u = u_0 e^{i(qx-\omega t)} \tag{3.36}$$

yielding:

$$\frac{\omega/v + i\alpha}{\omega} = \left(\frac{\rho}{c'}\right)^{1/2} \tag{3.37}$$

The wave velocity v and the attenuation coefficient α (per unit length) are then given by:

$$v = \rho^{-1/2} Re\left[(c')^{1/2}\right] \tag{3.38}$$

$$\alpha = \omega\rho^{1/2} Im\left[(c')^{-1/2}\right] \tag{3.39}$$

Substituting for the elastic constant c' and using the fact that $e_{piezo}^2/c\varepsilon$ is a small quantity yields:

$$v = v_0\left\{1+\frac{e_{piezo}^2}{2c\varepsilon}\left[\frac{1+(\omega_\sigma/\omega_D)+(\omega/\omega_D)^2}{1+2(\omega_\sigma/\omega_D)+(\omega/\omega_D)^2+(\omega_\sigma/\omega)^2}\right]\right\} \tag{3.40}$$

$$\alpha = \frac{\omega}{v_0}\frac{e_{piezo}^2}{2c\varepsilon}\left[\frac{(\omega_\sigma/\omega)}{1+2(\omega_\sigma/\omega_D)+(\omega/\omega_D)^2+(\omega_\sigma/\omega)^2}\right] \tag{3.41}$$

where v_0 is $\sqrt{c/\rho}$ and is the acoustic wave velocity as the conductivity tends to infinity (and the piezoelectric field is completely screened). At low temperatures ω_D is usually much greater than ω_σ so finally :

$$v = v_0\left\{1+\frac{e_{piezo}^2}{2c\varepsilon}\left[\frac{1}{1+(\omega_\sigma/\omega)^2}\right]\right\} \tag{3.42}$$

$$\alpha = \frac{\omega}{v_0}\frac{e_{piezo}^2}{2c\varepsilon}\left[\frac{(\omega_\sigma/\omega)}{1+(\omega_\sigma/\omega)^2}\right] \tag{3.43}$$

3.2.3 Modification for Surface Waves

Equations (3.42) and (3.43) can be modified for surface waves by using the effective electromagnetic coupling coefficient K_{eff} defined in Eqn 3.19 [74]:

$$v = v_0\left\{1+\frac{K_{eff}^2}{2}\left[\frac{1}{1+(\omega_\sigma/\omega)^2}\right]\right\} \tag{3.44}$$

$$\alpha = \frac{\omega}{v_0}\frac{K_{eff}^2}{2}\left[\frac{(\omega_\sigma/\omega)}{1+(\omega_\sigma/\omega)^2}\right] \tag{3.45}$$

3.3 Introduction to Quantum SAW Scattering

The classical model of SAW-electron interaction outlined above is only strictly valid when $ql<<1$, where l is the electron elastic mean free path and q is the SAW wavevector [71]. In the experiments described in later chapters this condition is only sometimes satisfied and then only marginally: when the SAWs are incident on a two dimensional electron gas, and when they propagate parallel to quantum wires. When $ql>>1$ quantum mechanical perturbation theory should be used. The vibrations of the atoms about their equilibrium positions, caused by the SAWs, introduce a time-dependent component H_{ep} into the time-independent one-electron Schrödinger equation. This is the electron-phonon interaction and it is usually weak enough for H_{ep} to be considered as a small perturbation that induces transitions between unperturbed states.

In the classical relaxation model described previously the attenuation and velocity shift of SAWs due to the interaction with conduction electrons were found to be functions of the electron conductivity. Conductivity, and the electron mean free path, are clearly not defined either across quantum wires or within quantum dots, and in these cases a quantum mechanical treatment of the SAW-electron interaction is demanded. In the discussion so far SAWs have been described classically as elastic lattice vibrations. However, the energy of a lattice vibration is quantised, and the quantum of energy is called the phonon, with energy E:

$$E = \hbar\omega \tag{3.46}$$

where ω is the angular frequency of the elastic vibration. It is assumed that attenuation of the SAW signal is solely due to the absorption of single SAW quanta. From first

order perturbation theory the probability of the absorption of a SAW quanta by an electron is given by Fermi's Golden Rule [75]:

$$w = \int \frac{2\pi}{\hbar} \left| \langle f | H_{ep} | i \rangle \right|^2 \delta(E_f - E_i) dS_{fn} \tag{3.47}$$

where w is the probability per unit time of a transition from an initial state i to an available final state f, and the integral is over all final states S_f. The allowed transitions are determined by energy and momentum conservation as the SAW phonon carries energy $(\hbar\omega)$ and momentum $(\hbar q)$. In GaAs the electron-phonon interaction (at the measurement frequency of 70MHz) is known to be predominantly via the piezoelectric interaction [72], with the following Hamiltonian [76]:

$$\begin{aligned} H_{piezo} &= \frac{e e_{14}}{\varepsilon_0 \varepsilon_r} \left(\frac{\hbar}{2\rho V \omega_q} \right)^{1/2} \times \\ & 2i \sum_q \frac{1}{q^2 + q_0^2(B)} \left[\varepsilon_{q,x} q_y q_z + \varepsilon_{q,y} q_x q_z + \varepsilon_{q,z} q_x q_y \right] \left(a_q e^{iq.r} + a_q^+ e^{-iq.r} \right) \end{aligned} \tag{3.48}$$

where e_{14}, ρ, ε_r are respectively the piezoelectric constant, mass density, and relative dielectric constant of GaAs, V is the sample volume, q, ω_q are the SAW wavevector and frequency, ε_q is a unit polarisation vector, a (a^+) is the SAW annihilation (creation) operator, $q_0(B)$ is the magnetic field dependent inverse Thomas-Fermi screening length and x, y, z are the GaAs crystallographic axes. Although this quantum mechanical approach describes the attenuation of a SAW signal, to the best of our knowledge the model has not been extended to describe the velocity shift of a SAW signal due to the interaction with conduction electrons.

3.4 SAW Excitation via Interdigital Transducers

At its most simple the interdigital transducer (IDT) consists of a periodic array of metal electrodes (or fingers) deposited on the surface of a piezoelectric crystal, as sketched in *Figure 3.2a*. Note that as shown the metallisation ratio η, which relates finger width a with their spacing b ($\eta = a/b$), is one half (η determines the relative amount of harmonic generation relative to the fundamental [77]). The overlap of adjacent fingers is also constant and the IDT is said to be uniformly apodised. When a voltage is applied to the transducer a spatially periodic electric field is generated by the electrodes and, through the piezoelectric coupling, a corresponding acoustic stress is generated. If the voltage is applied at a frequency such that the SAW wavelength is equal to the periodicity of the electrodes ($\lambda = 2b$) there is strong coupling to surface waves. By symmetry, surface waves are radiated equally in two opposite directions, and the transducer is reciprocal in that it can also convert SAW energy into electrical energy.

The time dependent voltage applied to the transducer, $V_{in}(t)$, causes charge to instantaneously accumulate on adjacent electrode fingers. At any instant, adjacent electrode fingers have opposite voltage parity and hence opposite charge accumulation. Although the distribution of the time-varying electric field under the electrodes is complicated, it may be approximated as normal to the surface of the piezoelectric sample. In the *delta function model* the electric field distribution is further simplified by modelling it as a series of normalised delta function sources as sketched in *Figure 3.2b*. A summation of these sources, at a convenient reference point, can be used to simulate the resultant electric field intensity of one IDT [12].

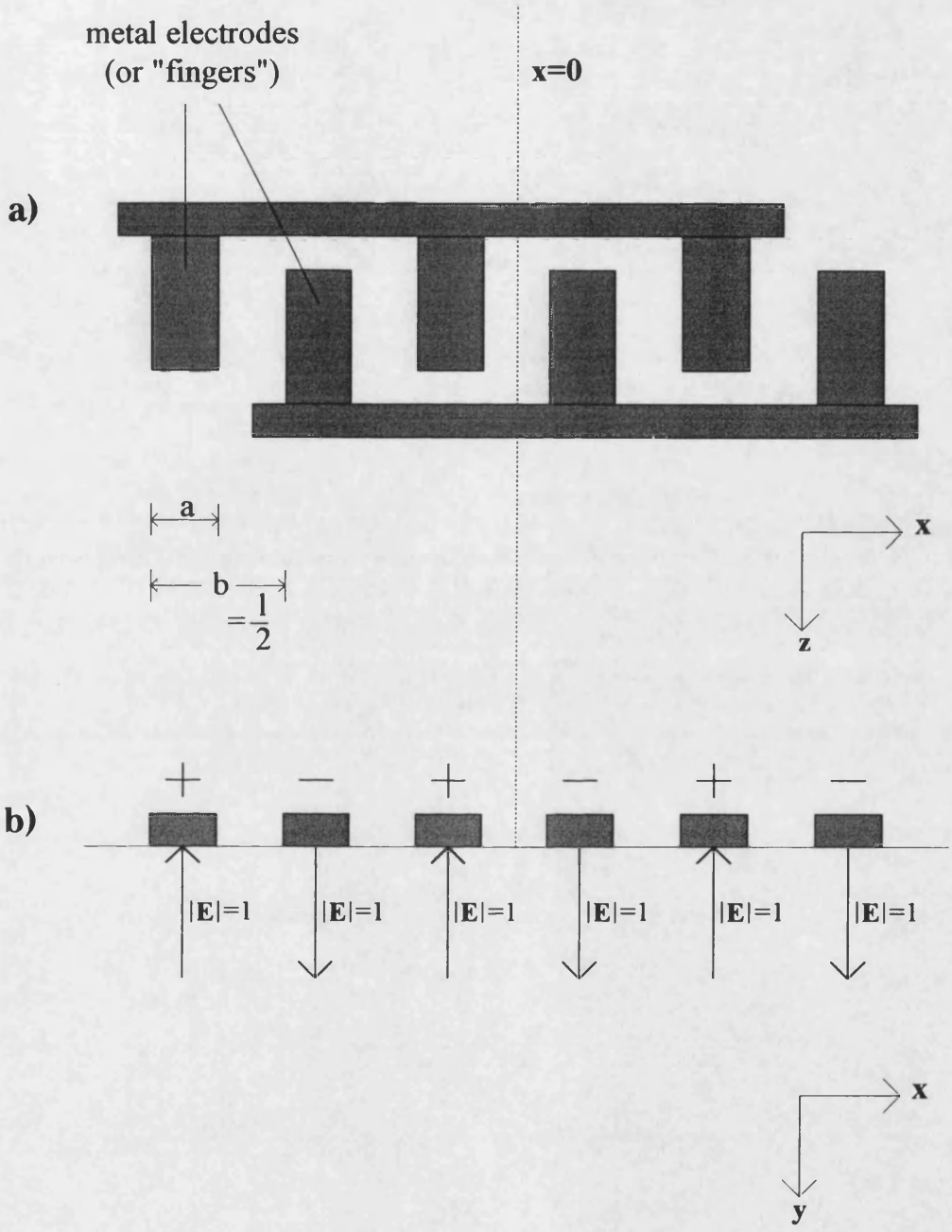

Figure 3.2: *(a) Bidirectional interdigital transducer with metallisation ratio η (= b/a) of one half and constant finger overlap. (b) Delta-function modelling of the electric field distribution in the xy-plane under an excited transducer.*

The summation therefore yields the relative amplitude of the generated SAW as function of frequency, or the frequency response $H(f)$. By summing the sources at the centre of the transducer, $x = 0$ (see *Figure 3.2*), the frequency response becomes:

$$H(f) = \sum_{m}^{M} (-1)^m e^{-ikx_m} = \sum_{m}^{M} (-1)^m \left\{ \cos(kx_m) - i \sin(kx_m) \right\} \tag{3.49}$$

where there are M delta sources, x_m is the distance of each source from the centre and the term $(-1)^m$ describes the alternating finger polarity. Although the sources are approximated as having electric fields of unit amplitude, there is a phase shift e^{-ikx_m} associated with each source at the summation point. However, at the reference axis, as $\cos(\theta) = \cos(-\theta)$ and $\sin(-\theta) = -\sin(\theta)$, the complex terms in the summation cancel out in pairs. The relative phase angle of the transfer function is therefore always 0 or 180° at $x = 0$ (depending which way round the leads are connected). Eqn. 3.49 can be further manipulated to obtain the frequency response centred at some centre frequency f_0:

$$|H(f)| \approx N \left| \frac{\sin\left\{ N_p \pi (f - f_0)/f_0 \right\}}{N_p \pi (f - f_0)/f_0} \right| \tag{3.50}$$

where N is the number of fingers, and $N_p = N/2$ for even N. *Figure 3.3* shows a calculated magnitude response of a uniform IDT with ten finger pairs and centre frequency 70MHz. A linear phase bandpass filter, in which both the phase and group velocities are ideally constant and equal over the desired frequency band of the filter, can be therefore be made using one IDT to transmit, and one IDT to receive, a SAW signal. As SAWs are non-dispersive all frequency components of the signal travel at the same velocity and no phase changes are introduced either by the material or by the transducers.

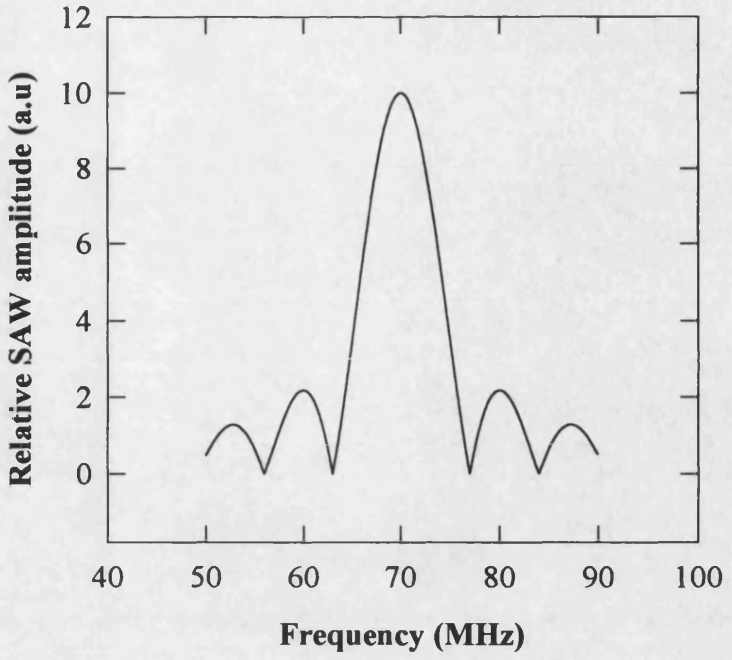

Figure 3.3: *Calculated frequency response of an uniform IDT with 10 finger pairs and centre frequency of 70MHz.*

This type of SAW filter with uniformly apodised IDTs is commonly referred to as a delay line, with the SAW propagation time τ given by $\tau = d/v_{SAW}$, where d is the distance between the centre points of the IDTs, and v_{SAW} is the SAW velocity. More complicated transducer geometries, for example "sinc apodisation", can lead to improved filter characteristics [12]. The delta function model is over-simplified and ignores such second order effects as electromagnetic feedthrough, triple-transit-interference, mass-loading discontinuities caused by the fingers, bulk wave interference, harmonic excitation and diffraction. In particular as impedances are not considered the model can only yield a transfer function that determines relative insertion loss as a function of frequency. Other more complicated models, such as the "crossed field model" have been developed to deal with these problems [12].

4 Measurement System

4.1 Sample Fabrication

4.1.1 Modulation Doped Heterostructures grown by MBE

Molecular beam epitaxy (MBE) and metal-organic chemical vapour deposition (MOCVD) (see [2] and [3] respectively for reviews) are widely used for the preparation of III-IV semiconductor multilayers both for research and commercial device applications. With these two epitaxial techniques (where epi means upon and taxi means arrangement) it is possible to grow layers of semiconductor, on a suitable substrate, where the chemical composition and doping of the layers can be controlled to thicknesses that are approaching atomic monolayers. MBE produces the better quality crystal and for this reason is used to grow most research material (for instance in MOCVD the interfaces between adjacent layers are not as abrupt as with MBE). Commercial devices, such as the high electron mobility transistor (HEMT) used in microwave applications, are mostly grown with MOCVD because of cost. The samples investigated in the work described in later chapters were fabricated from an $Al_{0.3}Ga_{0.7}As/GaAs$ heterostructure (#8393), grown by MBE on a semi-insulating (001) GaAs substrate (at the Max Planck Institute, Stuttgart), with an electron concentration of 2.1×10^{15} m^{-2} and a mobility of $60 m^2/Vs$ at 4.2K in the dark. The growth sequence of the wafer is shown schematically in *Figure 4.1a.*

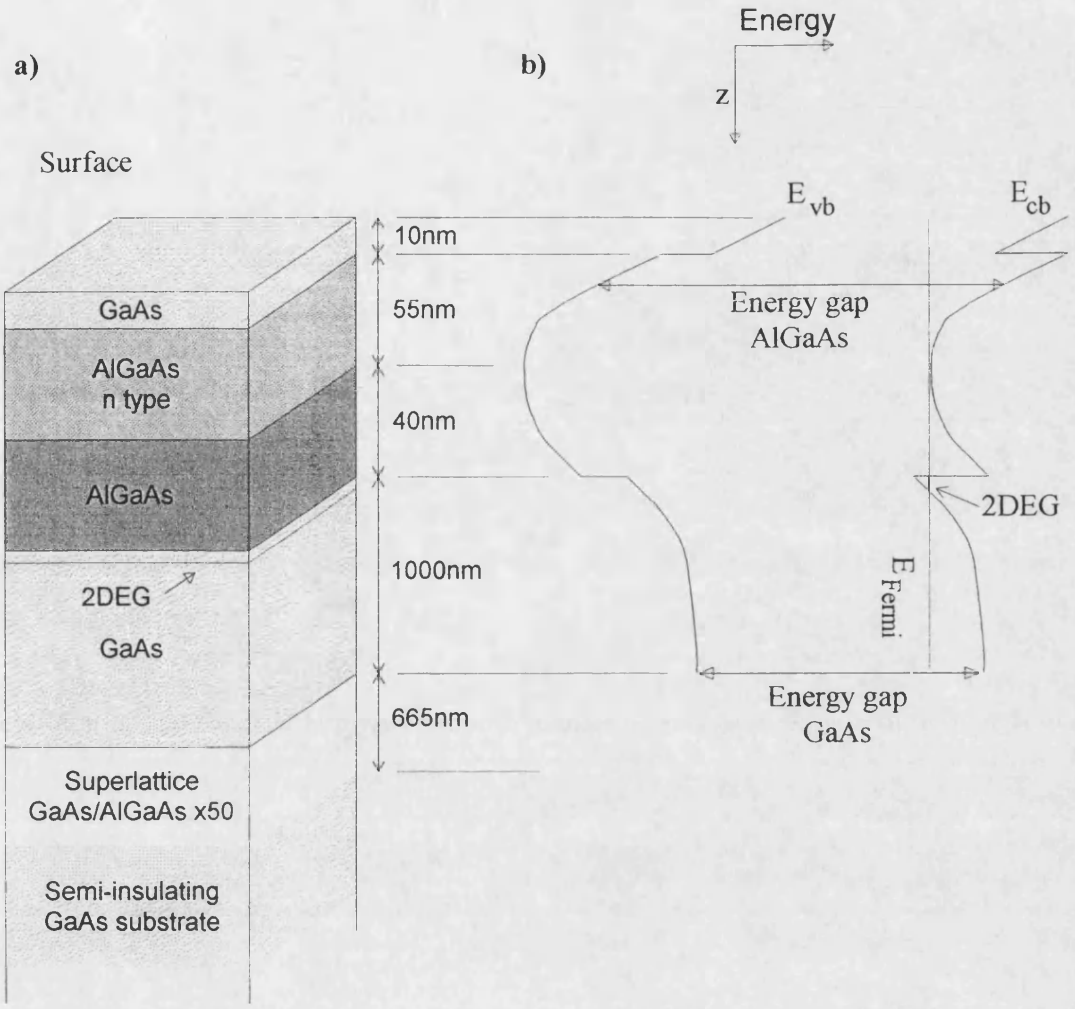

Figure 4.1: *(a) Schematic diagram of the crystal layers of the AlGaAs/GaAs heterostructure used to fabricate the samples used in this work. (b) Sketch of the conduction band edge energy E_{cb} and the valence band edge E_{vb} for the crystal in the growth direction z.*

A heterojunction is formed when two different semiconducting materials are brought into contact. Usually, as with $Al_{0.3}Ga_{0.7}As$/GaAs heterojunctions (now on referred to as AlGaAs/GaAs), the semiconductors have similar lattice constants so that the minimum number of defects and dislocations are formed at the interface. Each semiconductor is assumed to keep its bulk properties up to the interface, which is assumed to be only a few atomic layers thick. AlGaAs has a larger bandgap than GaAs and if the AlGaAs layer is donor doped, for example with silicon atoms, then electrons will diffuse from the AlGaAs layer to the GaAs layer, where they have a lower potential energy. The diffusion continues until the Fermi level in each material is the same. This process leaves behind unscreened positive ions in the AlGaAs layer which are spatially removed from the electrons. This separation reduces the Coulomb interaction between the ionised donor atoms and the electrons and hence increases the electron mobility. The technique of spatially separating donor electrons from their parent donor atoms is known as modulation doping. The redistribution of charge causes band bending which produces an electron potential at the interface as shown schematically in *Figure 4.1b*.

Electrons are unable to move across the interface but are unconfined in the x and y directions. To reduce further the Coulomb interaction of the electrons and ionised donors (which is usually the most important factor limiting mobility at low temperatures) a spacer layer of undoped AlGaAs is used to increase their spatial separation [78]. In the effective mass approximation, with an effective mass m* (which is also a function of z, but this is usually ignored) the normalised envelope wavefunctions $\xi_i(z)$ and the corresponding energy levels E_i for motion in the z direction are given by the Schrödinger equation :

$$\left[-\frac{\hbar^2}{2m^*}-\phi(z)\right]\xi_i(z)=E_i\xi_i(z) \tag{4.1}$$

where $\phi(z)$ is the electrostatic potential of the conduction band edge and can be calculated from Poisson's Equation:

$$\frac{\partial^2\phi(z)}{\partial z^2}=-\frac{\rho(z)}{\varepsilon_0\varepsilon_r(z)} \tag{4.2}$$

where $\rho(z)$ is the charge density ε_0 is the permittivity of free space and $\varepsilon_r(z)$ is the relative dielectric constant of the semiconductors (different for AlGaAs and GaAs and hence a function of z). However, the charge density is proportional to $\xi_i^2(z)$ and to solve fully for the energy levels and wavefunctions requires a self-consistent calculation, which can only be achieved numerically [79]. Surprisingly good values of the energy levels in the well, however, can be obtained by assuming a triangular potential [80]. Using this approximation the ground state electron energy level for wafer #8393 was calculated as ~36meV.

4.1.2 Nanostructuring using Holographic Lithography

In the GaAs/AlGaAs heterojunction described above the electrons are confined in the direction perpendicular to the layers of semiconductors. Quantum wires can be formed by taking a well defined two dimensional electron gas (2DEG), so that only one sub-band is occupied, and confining the electrons in one extra dimension perpendicular to the original confinement. Perhaps the most direct method of achieving this is to remove, by etching, part of the semiconductor material so that only a thin strip of 2DEG remains in

which the electrons are confined in two dimensions. Quantum wires and dots were structured from wafer #8393 using holographic lithography and reactive ion etching.

Holographic lithography is based on the same principles as optical lithography, which is used almost universally in the fabrication of semiconductor microstructures. The sample is first coated with a layer of optically sensitive material "photoresist" or 'resist" (most usually an organic polymer), the thickness of which can be carefully controlled. When exposed to light, typically ultraviolet (UV), some resists are weakened and can then be easily dissolved by solvents (or 'developer') that do not attack unexposed areas. These are known as positive resists. Exposed areas of negative resists harden with exposure and it is the unexposed areas that will be dissolved by the solvent. An opaque mask, typically made from metal film on glass, can be used to pattern resist by selectively shielding parts of the surface from exposure. Diffraction effects limit the smallest size of feature that can be transferred from the mask to the resist and using visible light this is in the range 0.4-0.8μm. In holographic lithography an expanded laser beam of UV light is split into two and then recombined at the surface of the sample to produce an interference pattern of "light" and "dark" stripes; *Figure 4.2* is a schematic diagram of the holographic lithography setup. This technique is therefore ideal to produce large area arrays of resist wires (due to the large area that is homogeneously illuminated), where the periodicity of the wires can be varied by changing the angle of incidence of the beam. The width of the wires is roughly equal to half the period (1:1 aspect ratio). The smallest period is defined by $\lambda/2\sin\theta$. By exposing the sample twice at reduced times, but at 90° orientations, it is straightforward to define dots in the resist. Wafer #8393, which was first diamond scribed into 7mm square samples, was patterned using an argon ion laser of wavelength 457nm and wires and dots of 1000nm and 500nm

periods were defined in the resist on the surface of the samples. *Figure 4.3a* and *Figure 4.3b* are scanning electron microscopy (SEM) images of wires and dots in the resist respectively.

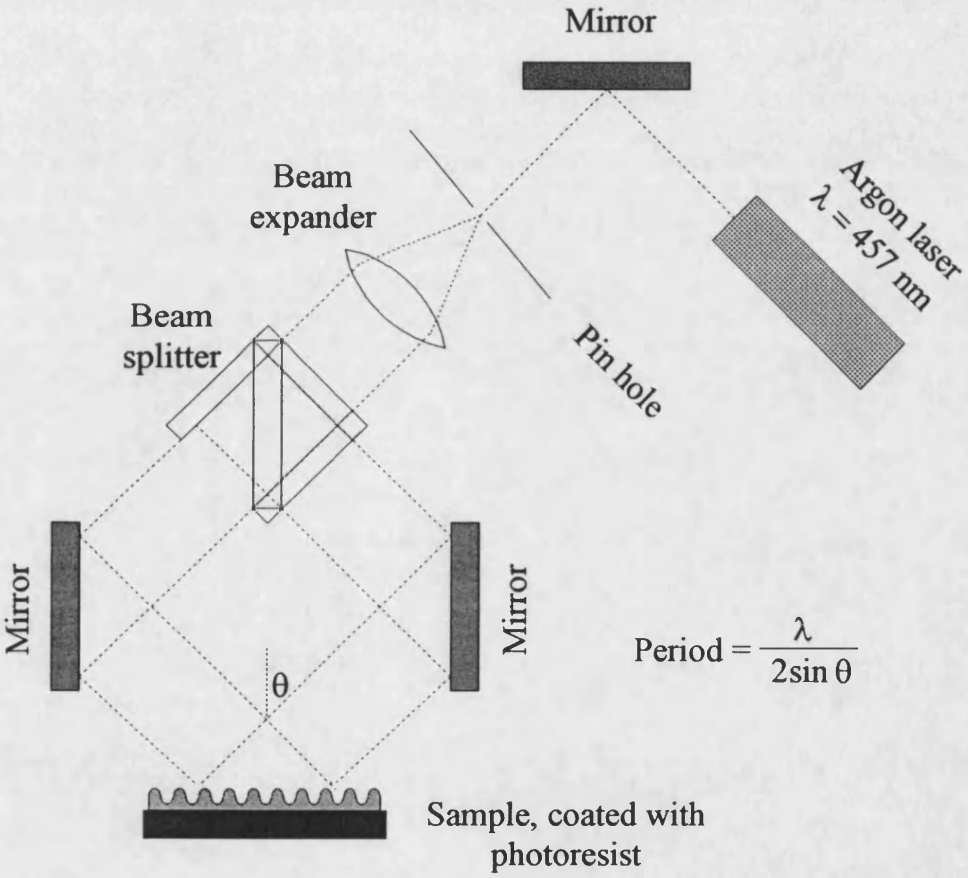

Figure 4.2: *Schematic diagram of the holographic process used to fabricate arrays of quantum wires and dots.*

a)

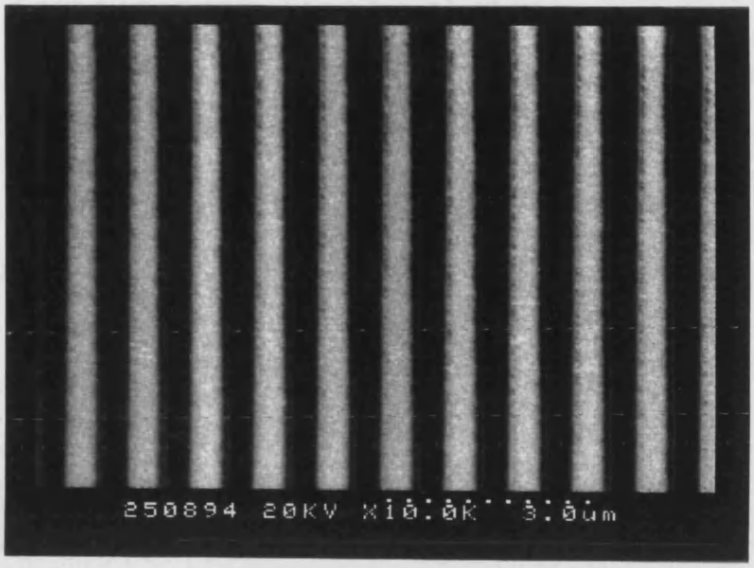

b)

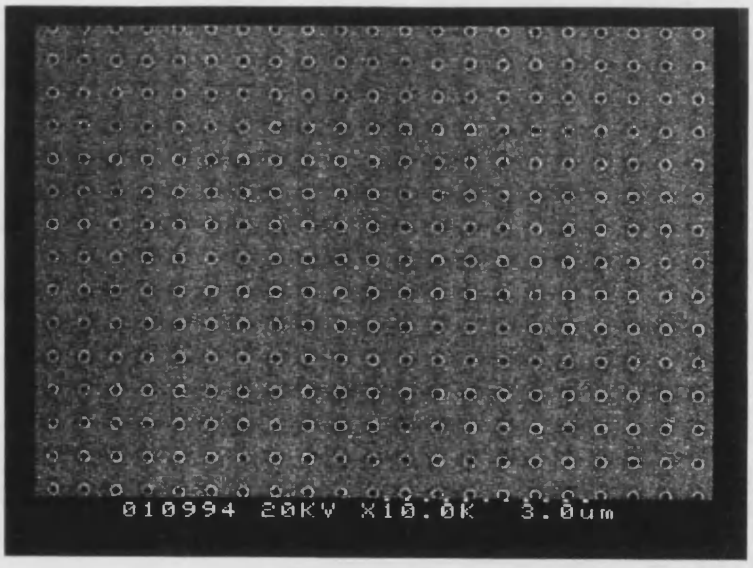

Figure 4.3: *Scanning electron microscope image of (a) an array of 500nm wide quantum wires and (b) an array of 250nm wide quantum dots formed in photoresist after holographic lithography (dark areas are photoresist).*

Two quantum wire samples #8393no6 and #8393no13 (with ~1:1 aspect ratios and 1000nm and 500nm periods respectively), and two quantum dot samples #8393no19 and #8393no15 (with ~1:1 aspect ratios and 1000nm periods and 500nm periods respectively) were used in the work described in later chapters. The wires were orientated parallel to the $[\bar{1}10]$ axis. One unstructured sample (#8393no.m2) was used as a test of the measurement system (see Chapter 5). Sample #8134no2 was also used for initial tests.

4.1.3 Reactive Ion Etching

After the holographic lithography the surface of the samples were covered by wires or dots made from photoresist. To pattern the semiconductor into real quantum wires and dots the areas unprotected by resist were etched to a depth of approximately 87nm using reactive ion etching (RIE). The etch depth was chosen so that edge depletion effects (where electrons become trapped in etching-induced surface states) at the boundary of the structures were minimised. Reactive ion etching has many advantages over wet etching due to its strong anisotropy, which allows microstructures with extreme height to width ratios to be patterned. In wet etching a liquid chemical (dilute acid or alkali) is used to attack the semiconductor. However, the rate of etching is very dependent on the crystal orientation, so that layers of resist can be undercut as the etchant follows the easiest path. In RIE an ion plasma etches the sample in a very directional fashion. The ion plasma is generated from a basis gas, $SiCl_4$, by an RF field applied between two plate electrodes on the lower of which the sample sits during etching. A DC bias applied to this plate accelerates ions towards the surface of the sample where they impact at almost

normal incidence. The etching process is a mixture of the chemical reaction between the plasma and the semiconductor and "milling" of the surface by the accelerated ions. Details of the RIE process are given in [81]. Before the RIE stage resist residues left on the exposed parts of the surface of the sample were removed using an Oxygen plasma. *Figure 4.4a* is a SEM image of an array of 500nm wide dots formed after the reactive ion etching, and *Figures 4.4b,c* are atomic force microscopy (AFM) images of some typical quantum wires and dots on test samples.

a)

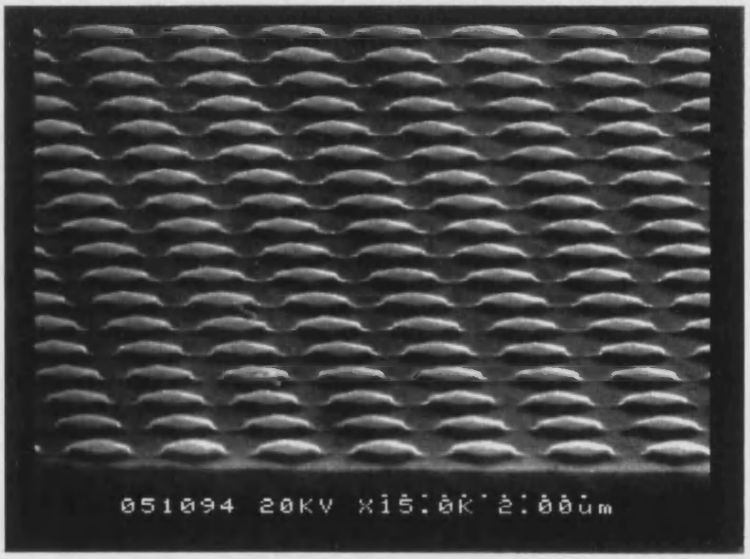

Figure 4.4: *Scanning electron microscope image of (a) an array of 500nm quantum dots formed on a test sample after holographic lithography and reactive ion etching.*

b)

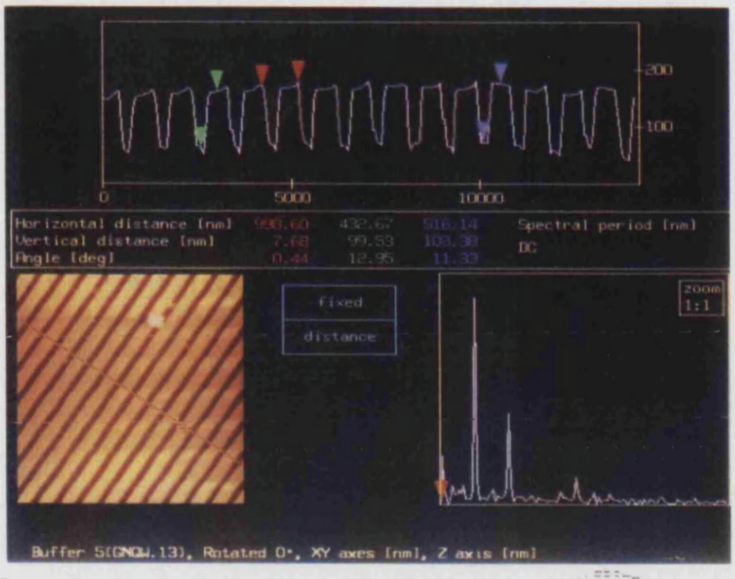

c)

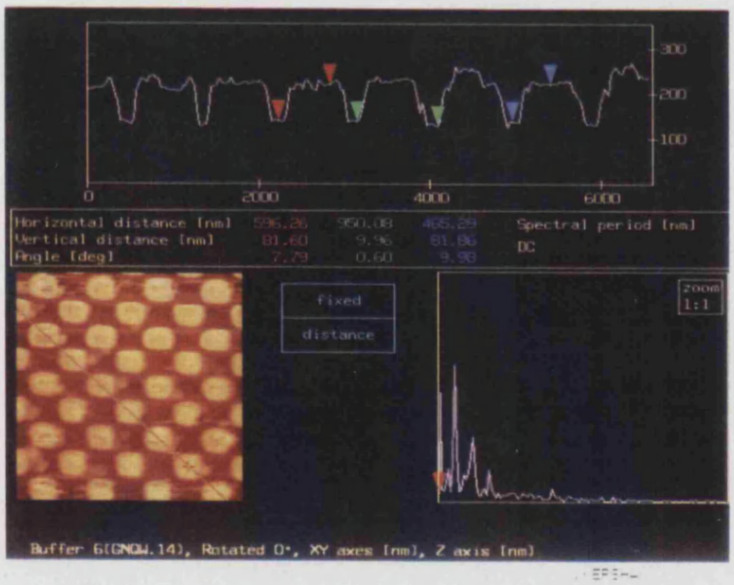

Figure 4.4: *Atomic force microscope images of (b) an array of 500nm wide quantum wires and (c) an array of 500nm wide quantum dots formed on a test sample after holographic lithography and reactive ion etching*

4.1.4 Fabrication of Interdigital Transducers

Before depositing the interdigital transducers (IDTs) used to excite the surface acoustic waves (SAWs) a wet mesa etch (using a mixture of H_2SO_4, H_2O_2 and H_2O in the ratio 1:8:40 [82]) was performed to leave an area around the edge of the samples free of conducting material. The etch depth in all cases was approximately 1μm. The samples were then coated in relatively thick layer (3000-3500Å) of photoresist and interdigital transducers were patterned in the resist using optical lithography. On each sample four IDTs were patterned, as shown in *Figure 4.5* which is schematic picture of a completed sample.

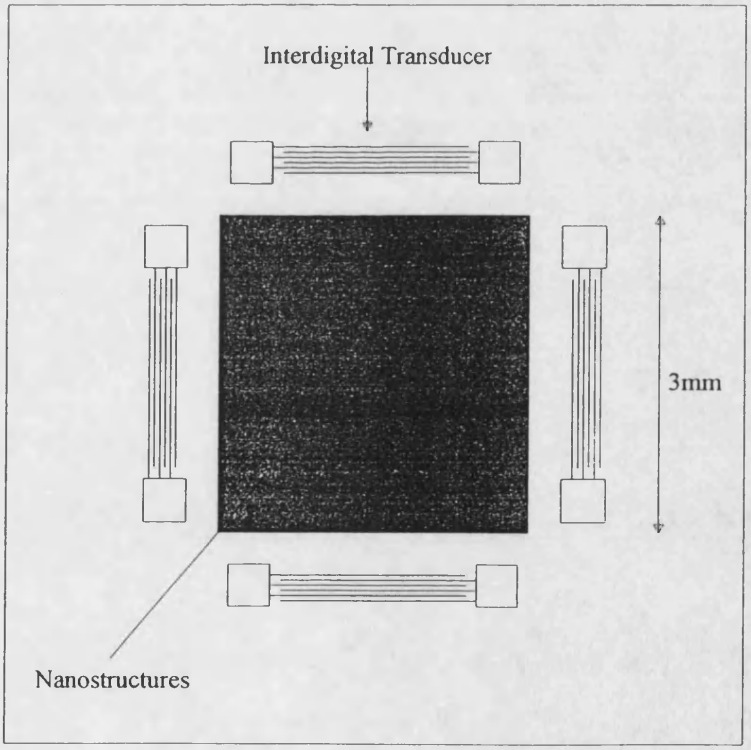

Figure 4.5: *Schematic diagram of a completed sample, with four interdigital transducers deposited on the surface.*

To harden the top layer of resist (by removing some of the solvent contained in the resist) the samples were soaked in chlorobenzene for ten minutes and then dried in an oven. This leads to the resist remaining after developing being undercut. A thin layer of chrome (~300Å) followed by a thicker layer of gold (2500Å) were then deposited on the surface of the samples via thermal evaporation. The remaining resist, and hence the metal on the resist, was then removed using propanol and acetone in the 'lift-off' process. Although the undercut of the resist due to the chlorobenzene soak dramatically improves the effectiveness of lift-off, in some cases gold from between the fingers of the transducers had to be removed using either the ultrasonic bath, or by using a single strand of a paintbrush under an optical microscope. *Figure 4.6* is an optical microscope image of a transducer where excess gold was removed in such a fashion. The width of each gold finger (or electrode), and the spacing between fingers, is 10μm, defining the wavelength of the excited SAWs to be 40μm. In each transducer there are ten finger pairs. To ensure that Schottky barriers were formed between the transducers and the semiconductor the samples were not subsequently annealed. A photograph of a portion of a completed IDT is shown in *Figure 4.7*. Note that the metallisation ratio of the transducers is one half η (ratio of the width of the fingers to their period), and that they have uniform overlap, or apodisation (see Chapter 3).

a)

b)

Figure 4.6: *(a) Optical microscope image of a portion of an interdigital transducer where the "lift-off" process was unsuccessful and a fragment of metal threatens to short two fingers and (b) the same portion of the transducer when the metal fragment has been removed using a paint brush. Magnification on both images was 1000x.*

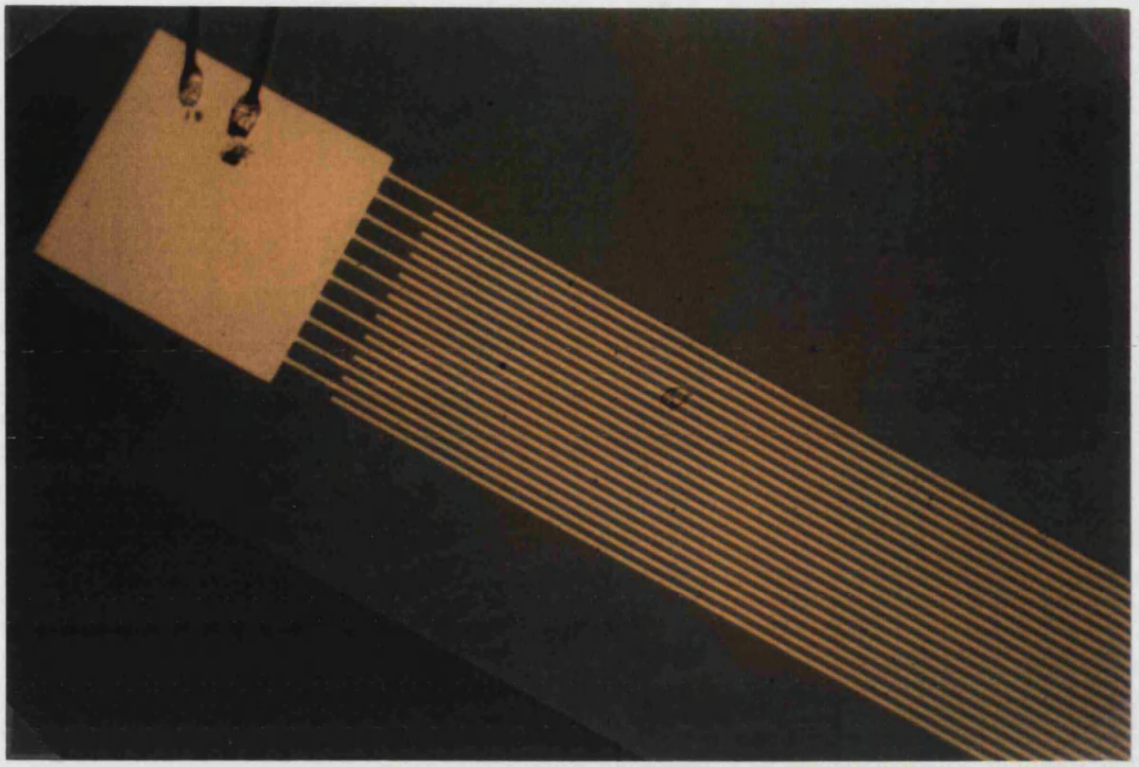

Figure 4.7: *An optical microscope image of a portion of a completed interdigital transducer.*

4.2 Cryogenics

4.2.1 Sample Mounting

Samples were mounted on alumina chip carriers using a silver loaded epoxy resin. An ultrasonic wedge bonder was used to connect both sides of each transducer to a gold pad on the chip carrier. As insurance against breakage of bond wires at low temperature both sides of a transducer were connected using two or three bond wires. A fine copper wire was indium soldered onto each gold pad on the chip carrier, and these solder joints were covered with a thin layer of silver loaded epoxy.

4.2.2 The Sample Probe

Measurements were performed using a liquid helium cryostat with a ten Tesla superconducting magnet. A schematic diagram of the cryostat is shown in *Figure 4.8.* The chip carrier containing the sample was mounted onto a copper sample stage using GE varnish. The sample stage was mounted at the end of a long stainless steel tube, *Figure 4.9a.* Four miniature semi-rigid coaxial cables (chosen to minimise thermal conduction) and four copper wires ran inside the tube connecting the sample stage to the top plate. At the sample stage the fine copper wires coming from the chip carrier were soldered directly to the semi-rigid cable (during initial measurements there was an intermediate pad between the sample and the cable). A temperature sensitive silicon diode, calibrated for temperatures above 1.4K, was mounted close to the sample, and a defocused GaAs infrared (IR) light emitting diode was used to illuminate the sample.

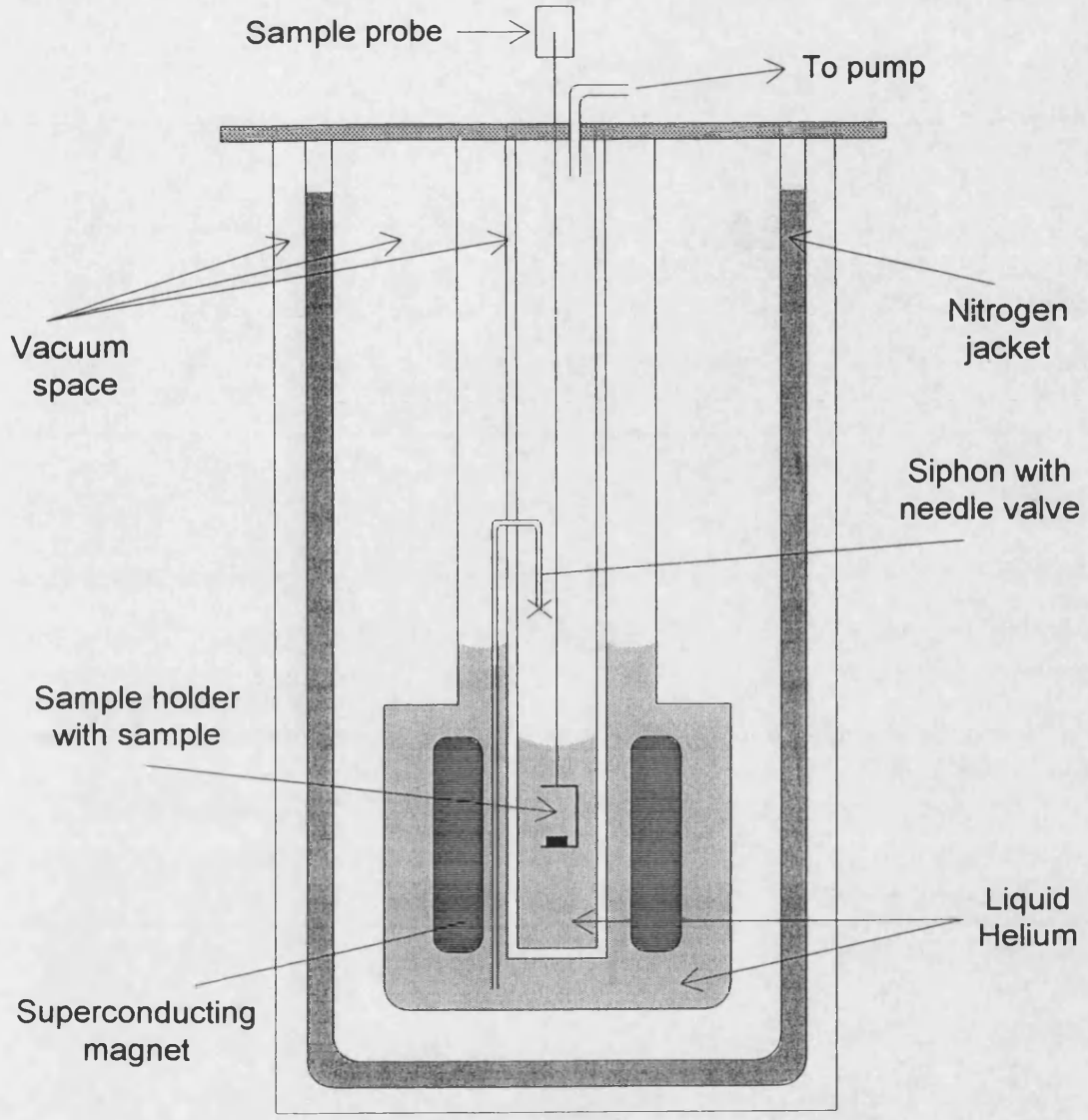

Figure 4.8: *A schematic diagram of the liquid helium cryostat used to perform measurements.*

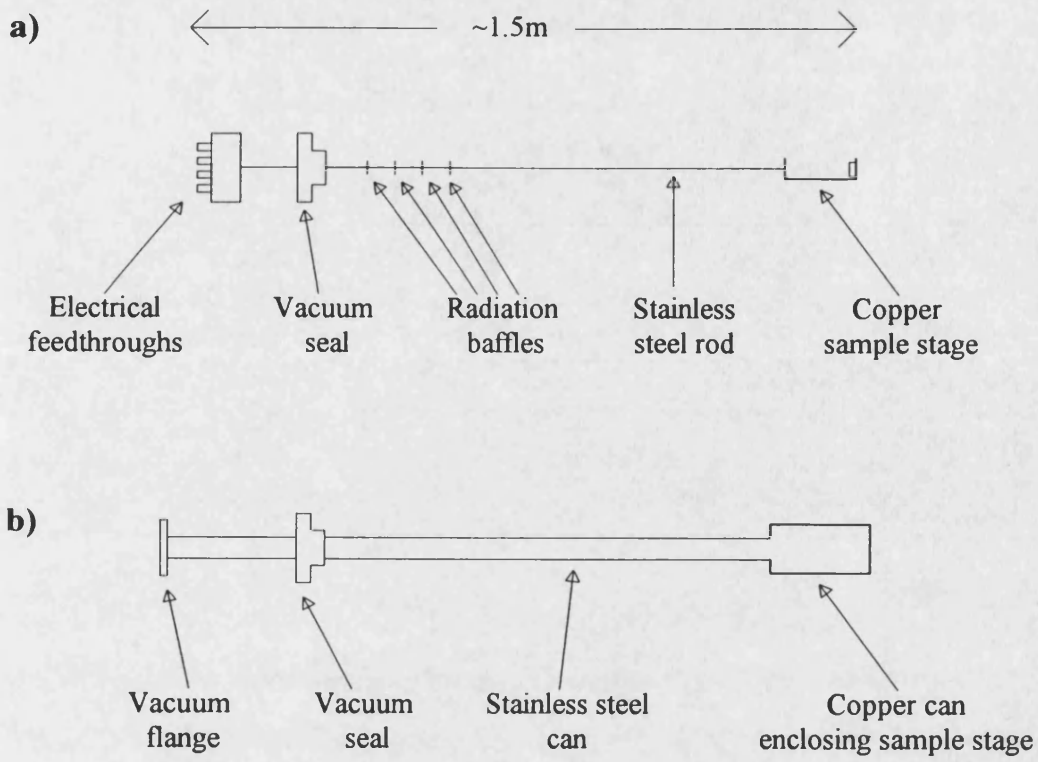

Figure 4.9: *(a) Sketch of the sample rod used to place sample at the centre of the superconducting magnet. (b) During later measurements the whole rod was surrounded by a stainless steel can and cooling of the sample occurred mostly radiatively.*

To obtain temperatures below 4.2K a high capacity rotary pump was used to lower the vapour pressure above the liquid helium, the lowest pressure obtainable being ~1.3mbar (measured at the top of the cryostat), corresponding to a temperature of 1.3-1.4K [83]. Initial measurements were made with the sample immersed in liquid helium. During later measurements the sample probe was surrounded by a can, *Figure 4.9b*, which was filled with approximately one atmosphere of gaseous helium at room temperature. In this case at temperatures below 4.2K the sample was in a partial vacuum and was therefore largely radiatively cooled. The can was introduced to determine whether contaminants in the liquid helium adverserly affected measurements (for example pieces of "dust" settling on the surface of the sample). No evidence of such effects was found. However, on average the measured SAW intensity was 13% (+/- 5%) higher when the can was used.

4.3 Instrumentation

4.3.1 Overview and Plan

A schematic diagram of the instrumentation is shown in *Figure 4.10.* A frequency synthesiser (Hewlett Packard 8647A, with an oven regulated oscillator), chosen for its spectral purity and stability, produces a continuous sine wave at 70MHz. For the majority of experiments the amplitude was set at -6.5dBm.

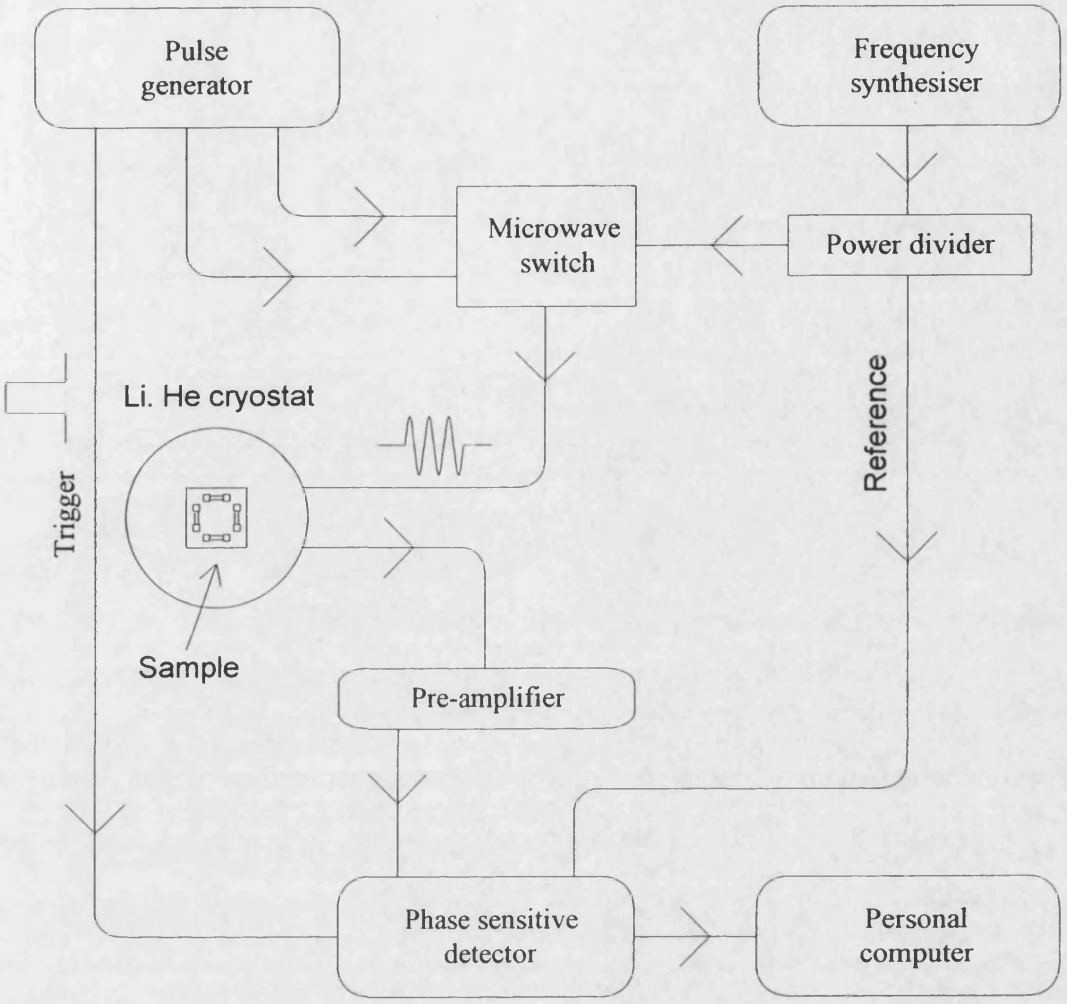

Figure 4.10: *Outline of the instrumentation used to measure changes in the measured surface acoustic wave intensity and phase. An explanation of the system is given in the text.*

The signal from the synthesiser is split into two parts of equal power with very little distortion using a power divider (Mini-circuits model ZFSC-2-1). One of the resulting signals is used as the reference for the phase sensitive detector. The other is gated using a GaAs microwave switch (Avantek MGS-71008) mounted on a double sided printed circuit board. The switch has a very good on/off ratio (~37dB at 1GHz). The width and repetition rate of the pulse (or tone-burst) produced by the gating unit was controlled by the pulse generator, and were set at 0.4μs (except for measurements on sample #8393no.m2 where it was set at 0.2μs) and 250KHz respectively, the intervals chosen to time out reflections from the edges of the samples. At the sample the electrical signal is converted (via one IDT) into a SAW pulse which then propagates across the surface of the sample. At the opposite transducer the SAW pulse is converted back into an electrical signal, having taken approximately 1.4μs to transverse the sample.

This electrical signal is pre-amplified, and then fed to input of the phase sensitive detector, which was purpose built to measure small relative changes in the amplitude and phase of the received SAW pulse. Semi-rigid cable and SMA connectors were used as much as possible to obtain a stable and fixed measurement system (for example bending impedances in standard coaxial cables might produce spurious changes in the measured SAW amplitudes). All cables and connectors were 50Ω. An IBM compatible personal computer was used to control the superconducting magnet power supply and phase sensitive detector and to process and store data.

4.3.2 Phase Sensitive Detector

A schematic plan of the phase sensitive detector is shown in *Figure 4.11*. After further amplification demodulation takes place by the multiplication of the signal received from the sample with the delayed, constant amplitude reference signal. The product is a dc level, which can be zero if the phase difference between the reference and signal is 90° or 270°, together with some ac components. Demodulation takes place eight times, with the reference signal delayed by an extra 2.77ns between each multiplication. This delay is set by a digital delay line (Newport 60AO28). A gated integrator, which acts as a low pass filter, then removes the ac components of the demodulation plus any high frequency noise. The width of the gate pulse, and its delay from the trigger signal received from the pulse generator, is set from the front panel of the detector so that gate pulse can be made to overlap with the signal received from the sample. The integrator is designed to have exponential averaging characteristics as it has a time constant much greater than the width of the pulse received from the sample. Further filtering is achieved by an eight channel muliplexed RC network which again has the attributes of a gated integrator with exponential averaging characteristics. The resistance values of the network can be selected from the front panel, therefore determining the time constant, and the capacitors are used to store each of the eight dc signal from demodulation. A demulitplexer, addressed by the system controller, switches the selected capacitor to a high impedance amplifier-buffer. This buffered signal is then fed to a front panel socket and also feeds, through a filter, a +/- 20,000 count analogue to digital converter (ADC).

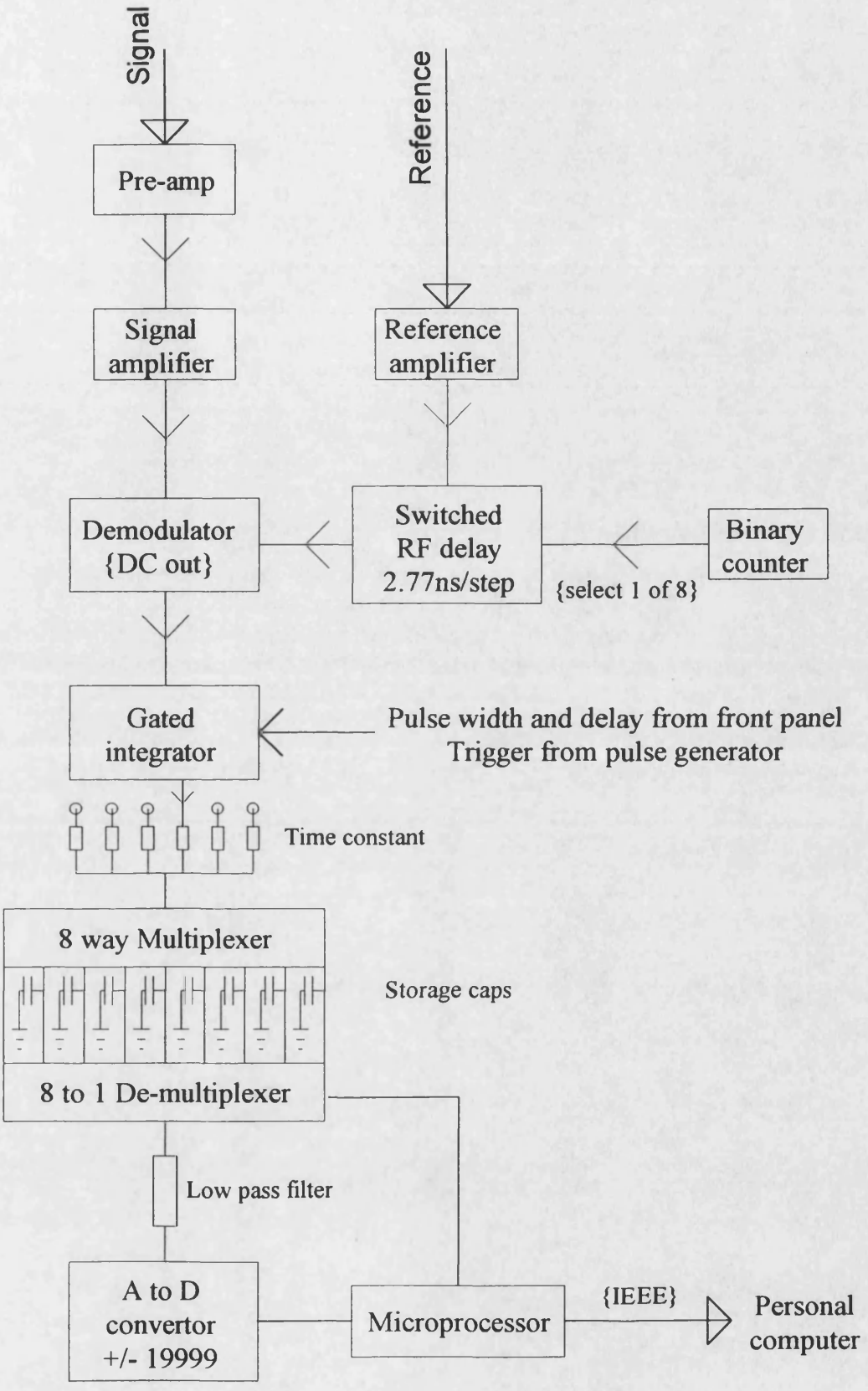

Figure 4.11: *A schematic representation of the purpose-built phase sensitive detector. A summary of the principles of operation of the detector is given in the text.*

Data from the ADC is made accessible to the computer via the GPIB. The eight dc signals produced by the demodulation lie on a sine wave, of frequency 70MHz, which represents the relative amplitude and phase of the signal received from the sample

4.3.3 Interdigital Transducer Characteristics

The resonant frequency, f_0, of the transducers is defined by the SAW velocity v and wavelength λ: $f_0 = v/\lambda$. The SAW velocity in GaAs is approximately 2841 m/s at room temperature [71], giving a resonant frequency of ~71.0MHz for the 40μm period transducers on the samples. The transmitted SAW amplitude across sample #8393no6 (SAW propagation parallel to 500nm quantum wires) was measured as a function of frequency at both room and liquid nitrogen temperatures and is shown in *Figure 4.12a*. The resonant frequency can be measured from this trace and is found to be approximately 70.0MHz at room temperature, suggesting that the SAW velocity is approximately 2800m/s. At 77K the resonant frequency is slightly higher, suggesting that the SAW velocity increases on cooling. This is consistent with both measurements of the elastic constants of GaAs as a function of temperature [84] and also with measurements made here (see Section 4.5.2). In Chapter 3 the *delta function model* was introduced as a means of calculating the frequency response of one IDT. In *Figure 4.12b* the measured and simulated frequency responses are plotted together (the simulated frequency response has been squared, as one transducer is used to transmit the SAW pulse and a second transducer is used to receive it, and then scaled to fit the measured data at the resonant frequency).

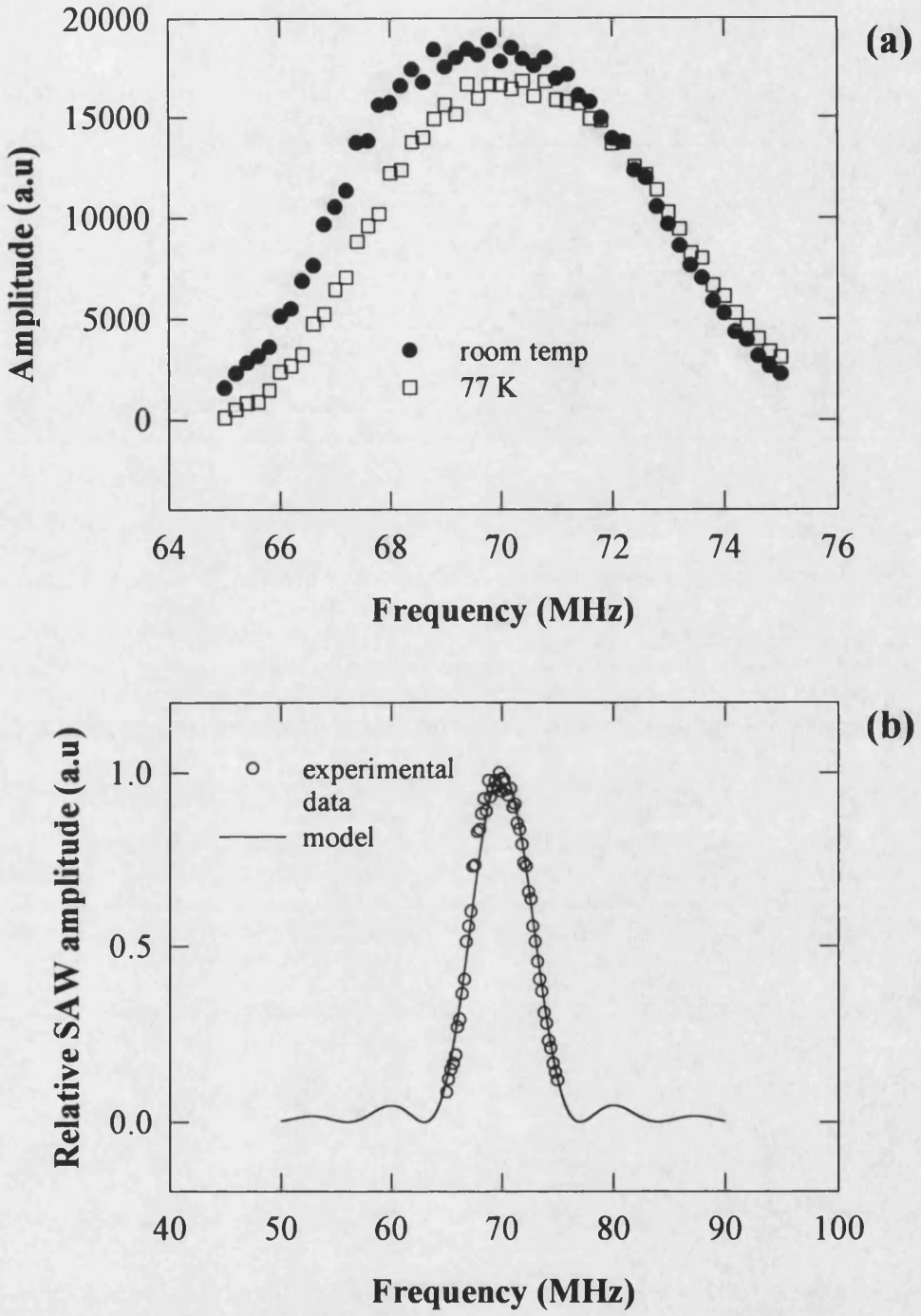

Figure 4.12: *(a) Measured frequency response of an interdigital transducer at room temperature and 77K. (b) Measured frequency response compared to the frequency response calculated using the delta function model. The data have been scaled to have equal amplitudes at the resonant frequency.*

In the *crossed field model* one IDT is represented in an electrical equivalent circuit as a capacitor C_T in parallel with a fictitious conductance $G_a(f)$, *Figure 4.13*. The capacitor describes the total static capacitance of the IDT finger pairs, and the conductance is related to SAW power emission from the excited transducer. The capacitance and conductance can be calculated from [12]:

$$C_T = NC_0W \tag{4.3}$$

$$G_a(f_0) = 8K_{eff}^2 f_0 C_T \tag{4.4}$$

where N is the number of IDT electrode pairs, W is the electrode apodisation overlap, C_0 is the capacitance/electrode pair/unit length, f_0 is the centre frequency of the transducer and K_{eff}^2 is the effective piezoelectric coupling coefficient.

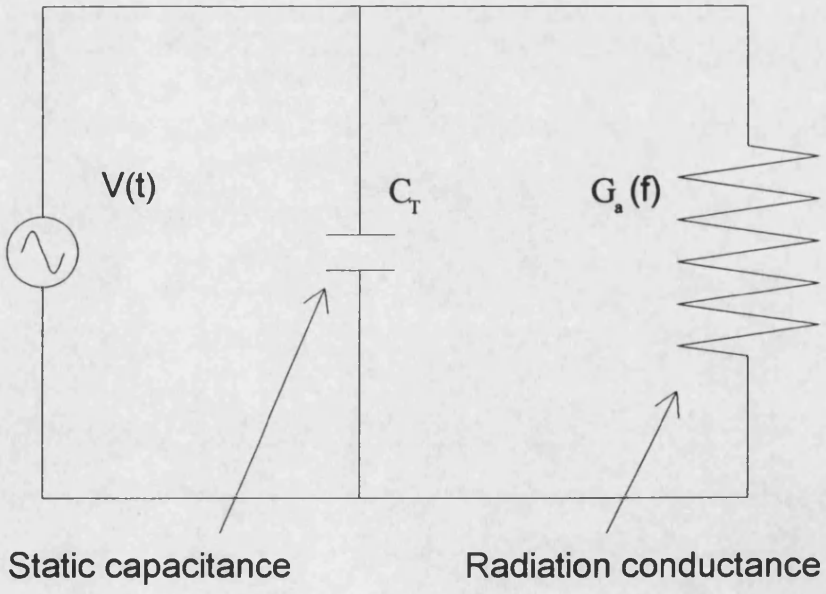

Figure 4.13: *Equivalent electrical circuit of an interdigital transducer in the crossed-field model.*

In GaAs at room temperature C_0 is 1.2pF/cm [85] and K^2_{eff} is 6.4 x 10^{-4}. The IDTs fabricated on the samples have W=1.8mm, f_0=70MHz and 10 (=N) finger pairs, giving calculated values of 2.16pF and 7.7 x 10^{-6} siemens for C_T and $G_a(f)$ respectively. The input impedance Z of one IDT at the resonant frequency is :

$$Z = \frac{1}{i\omega C_T + G_a(f_0)} \tag{4.5}$$

Using a network analyser the average input impedance of the four transducers on sample #8134no2 was measured as 13.40-452i at 69.6MHz, giving values of 5pF and 6.6 x 10^{-5} siemens for C_T and $G_a(f)$ respectively. The larger than expected capacitance measured may be due to the mounting of the sample in a diecast box, with associated long wires. The average magnitude of the reflection coefficient (the amplitude of the signal reflected over the incident amplitude) was measured as 0.97, implying a large mismatch between the transducers and a 50Ω system. The simplest matching circuit is the incorporation of a series or shunt inductance L to tune out C_T. Due to the limited space available in the measurement cryostat, however, this was found to be impracticable and stable matching at the top of the sample probe was also found to be difficult, and was eventually abandoned.

4.3.4 Software and Measurement Procedure

An outline of the operation of the QBASIC program, "Prog5.bas", used to control the instrumentation is shown in *Figure 4.14*.

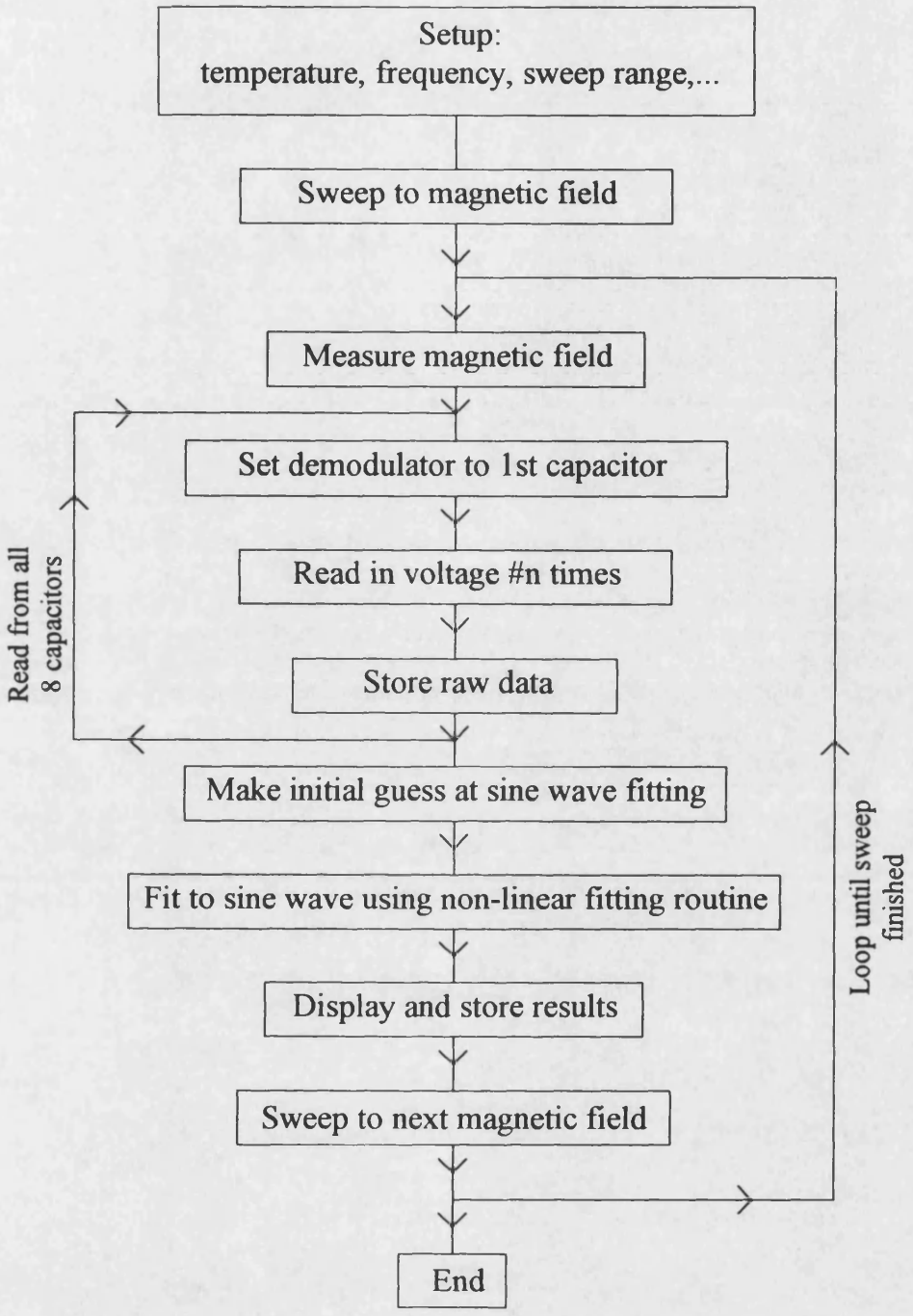

Figure 4.14: *Outline of the operation of the program used to control the instrumentation and process the data.*

Typical magnetic field sweeps were from 0-10 Tesla, with measurements of SAW amplitude (intensity data was obtained by squaring the measured amplitude) and phase made at ~0.066T intervals, and each sweep took approximately ninety minutes to complete. To avoid problems with hysteresis either only up, or only down sweeps, were made for a particular sample. At each magnetic field point the voltages stored in each of the eight capacitors in the muliplexer in the PSD were filtered, digitised and read by the computer sequentially. Although the capability existed to take a number of readings from each channel and average them time constraints usually prohibited this. A sine wave was fitted to the eight measured channels using a least squares fitting routine, based upon the Levenberg-Marquardt method, taken from "Numerical Recipes: the art of scientific computing" with phase and amplitude used as fitting parameters [86]. Both the unprocessed data and the fitted amplitude and phase were stored in data files. Relative phase shifts $d\phi$ can be converted into relative velocity shifts dv using the following relationship:

$$dv = -\frac{d}{t^2}dt = -\frac{v^2}{d}dt = -\frac{v^2}{d}\frac{d\phi}{2\pi}\frac{1}{f} \tag{4.6}$$

where t is the time taken for the SAW pulse to traverse the sample, d is the centre to centre separation of the transducers, and f is the frequency.

4.4 Stability and Sensitivity of the Measurement System

Many unwanted factors influence both the stability of, and random fluctuations in, the measured SAW intensity and phase. Systematic effects include; temperature drift of instrumentation and samples, inaccurate calibration of the magnetic field and systematic

errors in the fitting of the sine wave to the eight channels in the PSD (for example no DC offset is allowed for). Random effects include: noise (for example RF pickup), digitisation errors, and noise arising from the asynchronous gating of the continuous wave signal. As there are many contributing factors it is therefore difficult to evaluate theoretically the overall performance of the system. In the following sections practical assessments of the stability of the system, temperature dependence of the sample characteristics and noise levels are given. As a criterion it is worth noting that the maximum changes measured in intensity and phase in an increasing magnetic field, with the SAWs incident on a 2DEG, are approximately 3% and 0.11 radians respectively (see Chapter 5).

4.4.1 Stability of the Measurement System

As each magnetic field sweep takes considerable time to complete it is important that there are no, or at least small, changes in measured SAW amplitude and phase due to the instrumentation (for example phase changes could be introduced due to the thermal contraction or expansion of cables). *Figure 4.15* shows transmitted SAW intensity and phase as a function of time, with test sample #8134no2 submersed in liquid helium, at 1 atmosphere, to keep the temperature constant. Over three hours the phase and intensity increased by approximately 0.01 radians and ~1% respectively. Additionally, these changes could possibly be due to the temperature of the liquid helium changing, rather than an instrumentation effect. Similar results were obtained with a commercial SAW filter submersed in ice-water (over five hours the phase and intensity changing by ~0.03 radians and ~1% respectively).

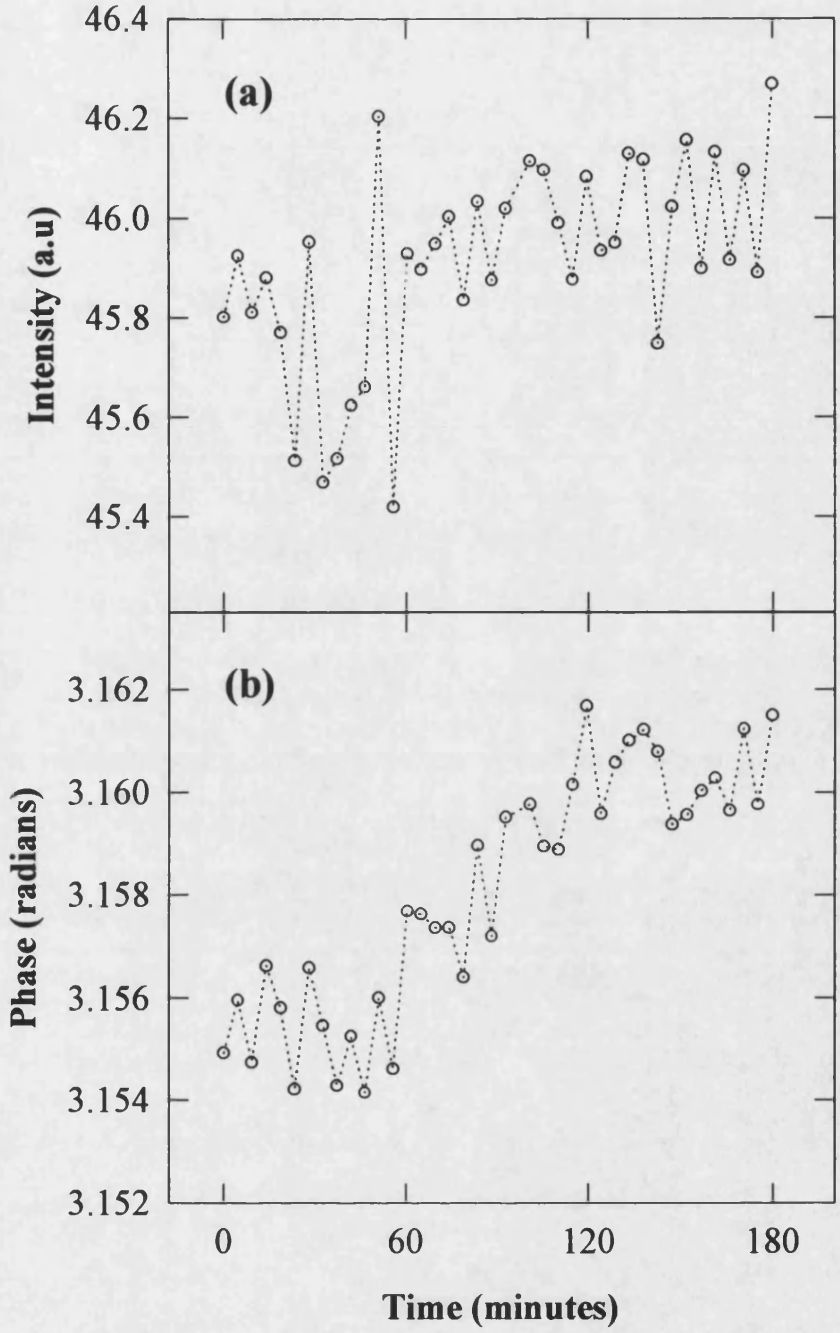

Figure 4.15: *Measured transmitted SAW (a) intensity and (b) phase as a function of time with test sample #8134no2 submersed in liquid helium.*

4.4.2 Temperature Dependence of the Sample Properties

Figure 4.16 shows the transmitted SAW intensity and phase as a function of temperature (above 4.2K) for test sample #8134no2 sitting in an atmosphere of helium gas. The temperature dependence of the SAW velocity, which is proportional to the measured phase, follows the temperature dependence of the elastic constants [84], as is expected from Eqn.3.18, and is reproducible from measurement to measurement. The temperature dependence of the intensity is more complex as it arises both due to the properties of the transducers and the attenuation of the SAW signal (for example by the phonon-phonon or phonon-electron interactions). In all measurements the SAW intensity is seen to broadly increase with temperature, although structure, such as the minimum at ~40K, is not reproducible from measurement to measurement. The attenuation coefficient of bulk acoustic waves in GaAs has been measured as increasing with increasing temperature [87], and it is unclear why the SAW intensity increases with temperature, but this perhaps indicates that it is the transducer characteristics that are dominant.

Figure 4.17 shows measured SAW intensity and phase as a function of temperature for sample #8393no15 immersed in liquid helium (after illumination). The temperature, measured using the silicon diode, is thought to be inaccurate below 4.2K and the abrupt changes seen in the phase and intensity at ~1.4K and 4K are thought to be due to the change in the density of liquid helium at the lambda point (2.2K), and to the surface of the sample "boiling dry " of liquid helium respectively.

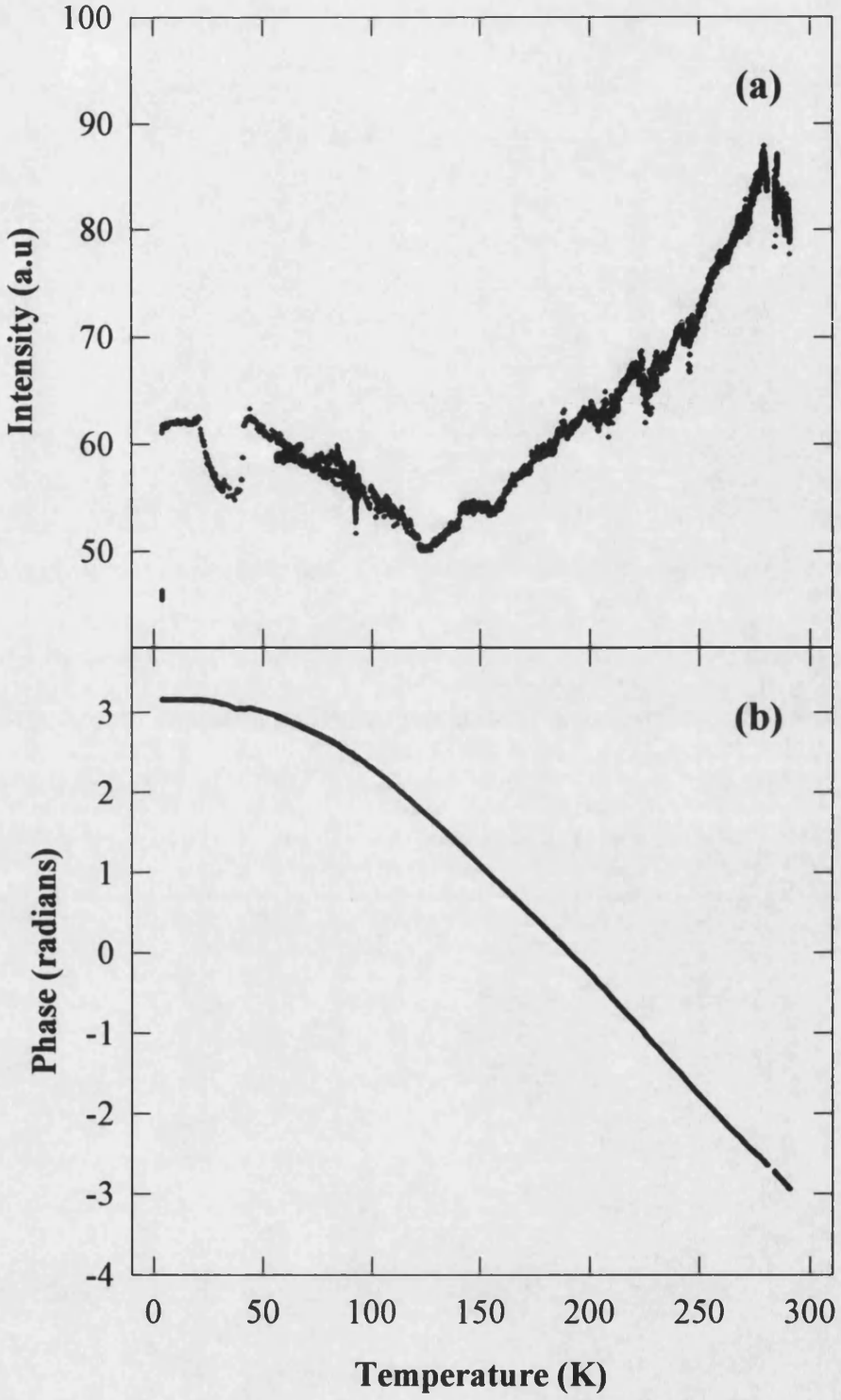

Figure 4.16: *Measured transmitted SAW (a) intensity and (b) phase as a function of temperature for test sample #8134no2 in an atmosphere of helium.*

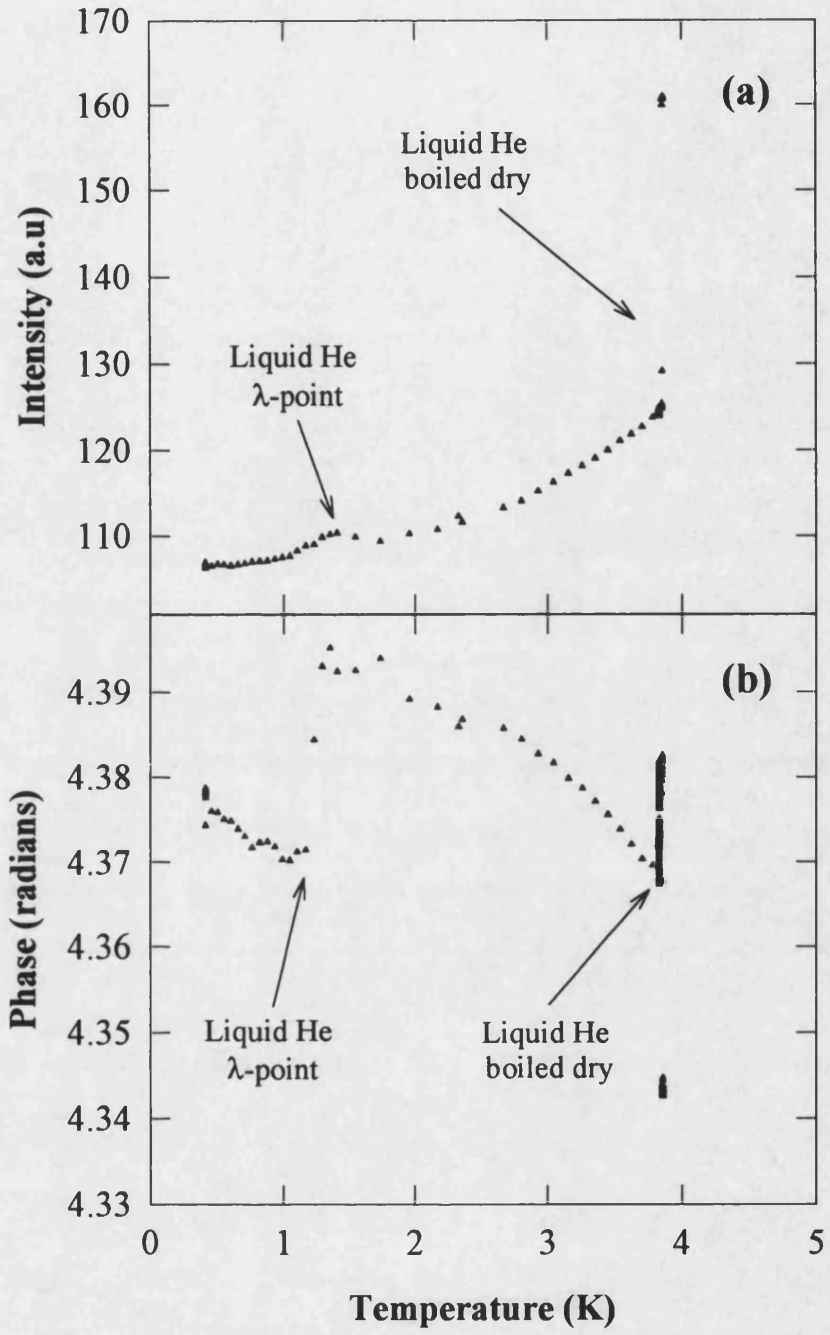

Figure 4.17: *Measured transmitted SAW (a) intensity and (b) phase as a function of temperature for sample #8393no15. Clearly visible are the marked changes in the intensity and phase at the λ point of liquid helium and when the helium boils dry at the sample surface.*

4.4.3 Measured Noise Levels

An indication of the noise levels has been obtained by examining magnetic field sweeps, with typical magnetic field increments, that were made with unilluminated quantum wire and quantum dot samples. The noise present in the SAW signal is assumed to be intrinsic to the measurement system and not due to the electronic properties of the samples (it is assumed here that there are too few electrons present, before illumination, in these samples to modulate the SAW signal, although this assumption is in itself an interesting area for further investigation). *Figure 4.18* shows measured SAW intensity and phase, as a function of magnetic field, for sample #8393no19 (quantum dots) at ~1.3K, and is typical of measurements on unilluminated samples. Neither the intensity or phase show significant magnetic field dependence. The standard deviation of the intensity is 0.08% (+/- 0.01%) of the mean intensity, and the standard deviation of the phase is 0.0022 (+/- 0.001) radians.

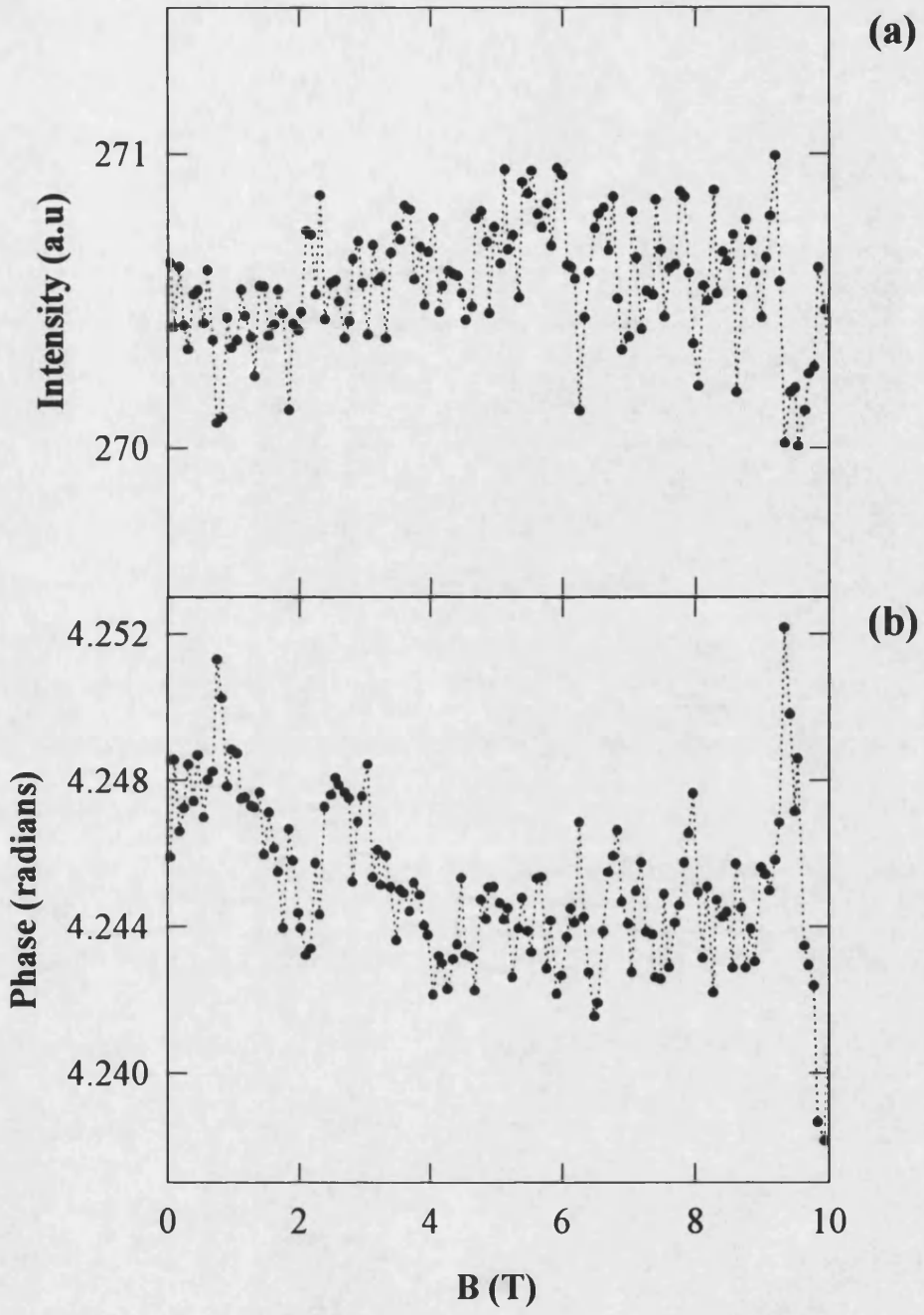

Figure 4.18: *Measured transmitted SAW (a) phase and (b) intensity as a function of magnetic field for sample #8393no19 without illumination.*

5 SAW Scattering from the 2DEG formed at an AlGaAs/GaAs Heterojunction

5.1 Introduction

Surface Acoustic Waves (SAWs) were first used to study quasi two dimensional systems by Wixforth et al [13,14]. At low temperatures the interaction between SAWs and electrons in a two dimensional electron gas (2DEG) leads to oscillations both in the transmitted SAW intensity, and in the SAW velocity shift, in an increasing magnetic field. These oscillations follow the Shubnikov-de Haas oscillations in the σ_{xx} component of the 2D conductivity tensor. The simple classical relaxation model outlined in Chapter 3, adapted for a sheet of 2D electrons, was used to describe the observed results, and the first part of this chapter describes the modifications required to apply the bulk classical relaxation model to a sheet of 2D electrons. SAW scattering data from unstructured 2DEG, obtained with the instrumentation described in Chapter 4, is then presented. The SAW scattering is described using both the classical relaxation model and quantum mechanically using Fermi's Golden Rule calculations.

5.2 The Classical Relaxation Model for 2D Electrons

In Chapter 3 the following expressions were derived for the velocity shift and attenuation coefficient of a SAW propagating on the surface of a piezoelectric conductor:

$$v = v_0\left\{1+\frac{K_{eff}^2}{2}\left[\frac{1}{1+(\omega_\sigma/\omega)^2}\right]\right\} \tag{5.1}$$

$$\alpha = \frac{\omega}{v_0}\frac{K_{eff}^2}{2}\left[\frac{(\omega_\sigma/\omega)}{1+(\omega_\sigma/\omega)^2}\right] \tag{5.2}$$

where K_{eff} is an effective electromagnetic coupling coefficient, v_0 is $\sqrt{c/\rho}$ (and is the acoustic wave velocity as the electron conductivity tends to towards infinity), and ω is the acoustic wave frequency. The conductivity relaxation frequency, ω_σ, is defined as:

$$\omega_\sigma = \frac{\sigma}{\varepsilon_1+\varepsilon_2} \tag{5.3}$$

where ε_1, ε_1 are the dielectric constants of free space and of the semiconductor crystal. These equations can be modified to describe the SAW-2DEG interaction by considering the electron gas as a thin sheet of mobile carriers (of thickness *d*) situated directly on top of the crystal, with a two dimensional sheet conductivity σ_{xx}^{2D} $(=\sigma d)$, so that the conductivity relaxation frequency becomes:

$$\omega_\sigma = \frac{\sigma_{xx}^{2D}/d}{\varepsilon_1+\varepsilon_2} \tag{5.4}$$

Adler [74] modelled the response of the electrons to the electric field of the SAWs by considering an oscillating voltage source driving a resistor and capacitor in series, where the time constant of the circuit (the "relaxation" time) is $1/\omega_\sigma$. In a conducting medium of semi-infinite height only a layer $1/q$ thick effectively carries the induced currents (which arise as the electrons move to screen the electric field of the SAW) as the electric field decays exponentially with depth z into the medium (electric field strength is proportional to e^{-qz}). However, in the 2DEG case only a thin conducting strip carries the induced currents and the effective resistance, and therefore the time constant,

increases by a factor $1/qd$ compared to an infinite medium. The conductivity relaxation frequency therefore becomes:

$$\omega_\sigma = \frac{\left(\sigma_{xx}^{2D}/d\right)qd}{\varepsilon_1+\varepsilon_2} = \frac{\sigma_{xx}^{2D}q}{\varepsilon_1+\varepsilon_2} \tag{5.5}$$

The ratio ω_σ/ω in Equations (5.1) and (5.2) therefore has to be replaced by the ratio $\sigma_{xx}^{2D}/\sigma_M$, where σ_M is a characteristic of the material and is defined as:

$$\sigma_M = \nu_0(\varepsilon_1+\varepsilon_2) \tag{5.6}$$

For GaAs σ_M is approximately 3.3 x 10^{-7} Ω^{-1} [13]. The expressions for the attenuation coefficient and the velocity shift therefore become:

$$\alpha = q\frac{K_{eff}^2}{2}\left[\frac{\left(\sigma_{xx}^{2D}/\sigma_M\right)}{1+\left(\sigma_{xx}^{2D}/\sigma_M\right)^2}\right] \tag{5.7}$$

$$\frac{\nu-\nu_0}{\nu_0} = \frac{\Delta\nu}{\nu_0} = \frac{K_{eff}^2}{2}\left[\frac{1}{1+\left(\sigma_{xx}^{2D}/\sigma_M\right)^2}\right] \tag{5.8}$$

It is usual to describe the attenuation in terms of the zero magnetic field intensity (typically at zero magnetic field the 2DEG conductivity is approximately four orders of magnitude larger than σ_M):

$$I(B) = I_0 e^{-\alpha L} \tag{5.9}$$

The attenuation coefficient, which is a non-monotonic function of the conductivity, and the velocity shift are shown in *Figure 5.1* as a function of $\sigma_{xx}^{2D}/\sigma_M$

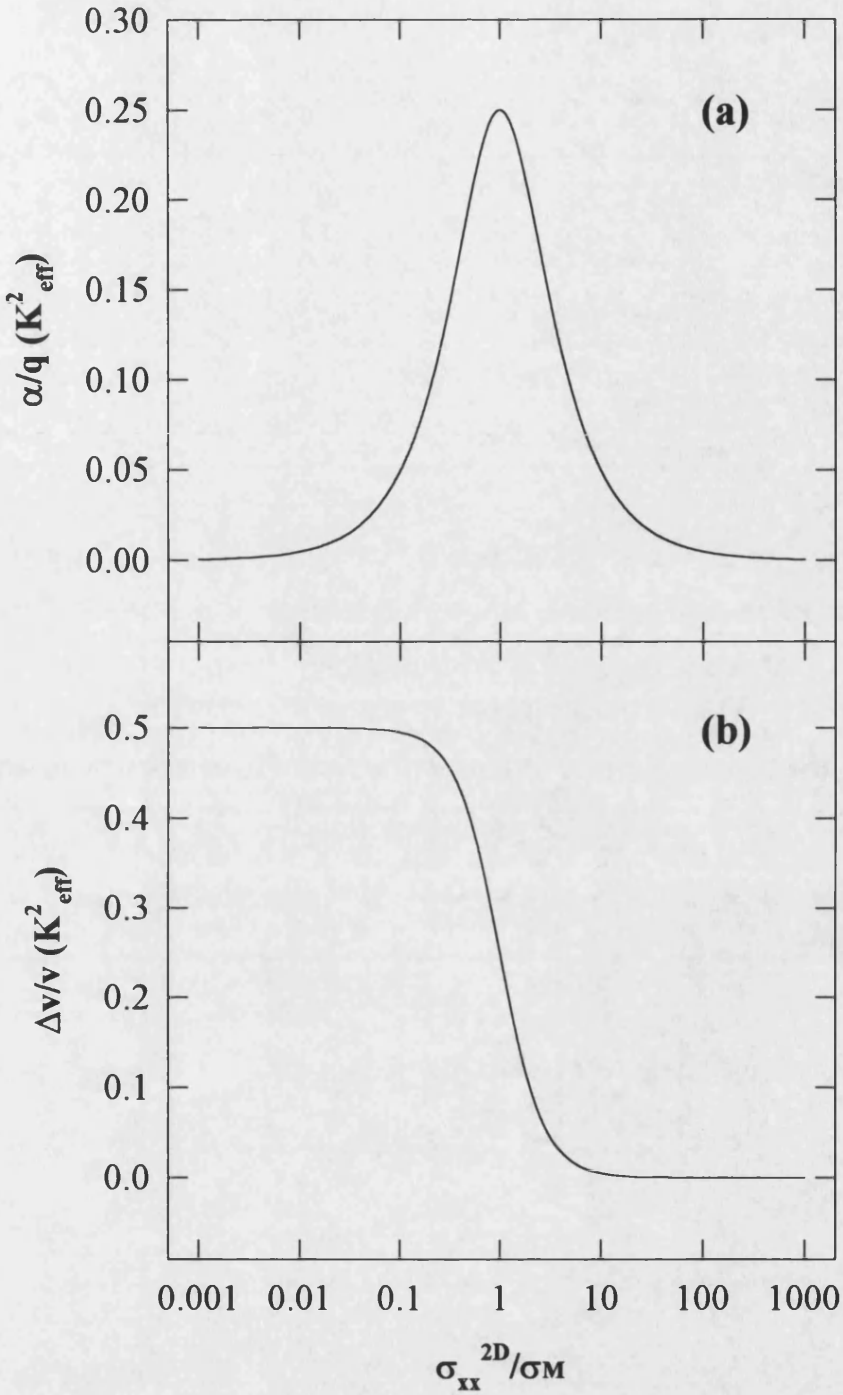

Figure 5.1: (a) *Attenuation coefficient α per unit wavevector q and (b) change in sound velocity $\Delta v/v_0$, both in units of K_{eff}^2, as a function of the sheet conductivity σ_{xx}^{2D} of the 2DEG, which is assumed to be on the top of the crystal surface.* σ_M *is a characteristic conductivity as defined in the text.*

For a (100) surface on GaAs, with a SAW propagating in the [110] direction, K^2_{eff} is 6.4 x 10^{-4} [71], so that the maximum predicted velocity shift is ~3 x 10^{-4} when moving from the insulating to the high conductivity case. The attenuation is a maximum when $\sigma^{2D}_{xx} = \sigma_M$, and the maximum predicted attenuation coefficient (for a SAW wavelength of 40μm) is ~30m^{-1}, giving a maximum predicted attenuation of ~1.1dB/cm (note that acoustic attenuation in decibels is 10log(I/I_0)). Both the maximum attenuation and velocity shift are independent of the value of σ_M.

5.3 SAW Scattering Results

Figure 5.2 shows transmitted SAW intensity and phase shift as a function of applied perpendicular magnetic field at 4.2 K, for SAWs propagating across sample #8393m2. The oscillations in both the phase and intensity are attributed to the Shubnikov-de Haas oscillations seen in the conductivity σ^{2D}_{xx}. The peaks in measured phase are labelled with the appropriate filling factor ν, and occur as the conductivity tends to zero (Eqn. 5.6). Note that the phase is proportional to the SAW velocity: an increase in the velocity of the waves results in an increase in the measured phase - see Chapter 4. A plot of integer filling factor versus inverse magnetic field is a straight line, *Figure 5.3*, and the 2D sheet concentration was calculated from the gradient (Eqn. 2.25) as 2.09 (±0.03) x 10^{15} m^{-2} at 4.2K in the dark, which compares well with the value of 2.1 x 10^{15} m^{-2} measured using the Hall effect (by the crystal grower).

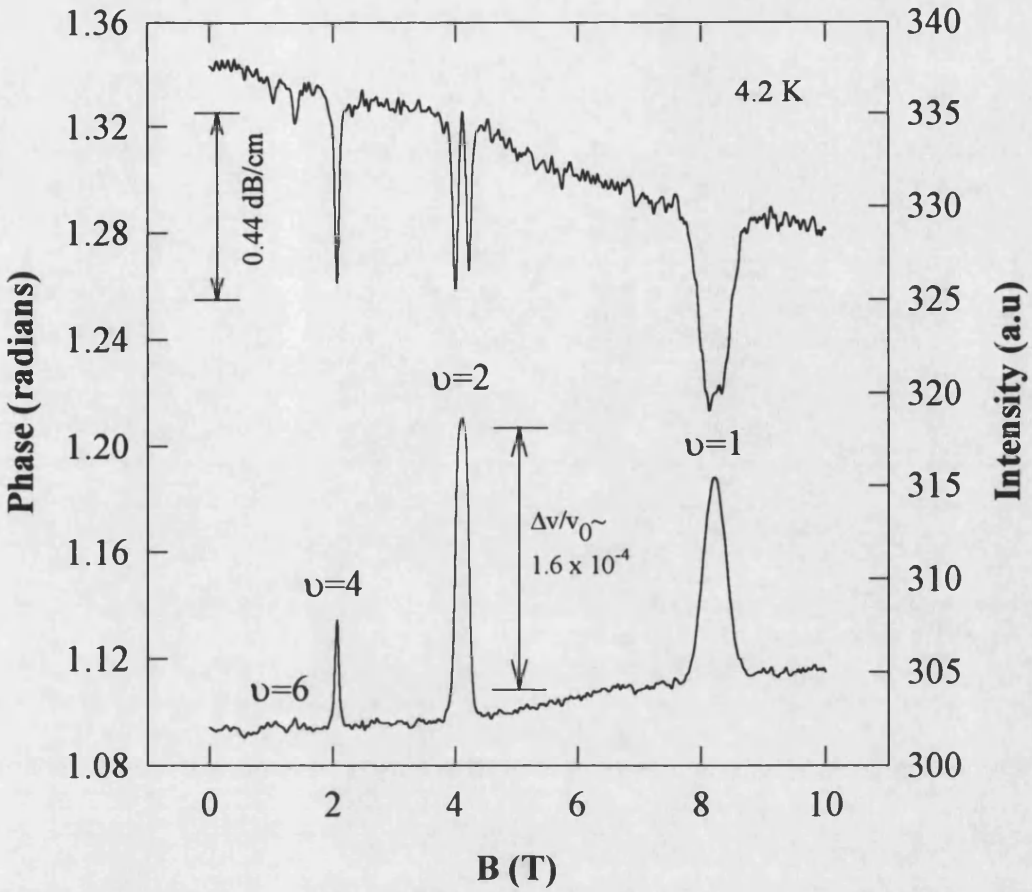

Figure 5.2: *Measured transmitted SAW intensity and phase as a function of applied magnetic field for unstructured 2DEG (sample #8393m2) at 4.2K. The peaks in phase are labelled with the appropriate filling factor as described in the text.*

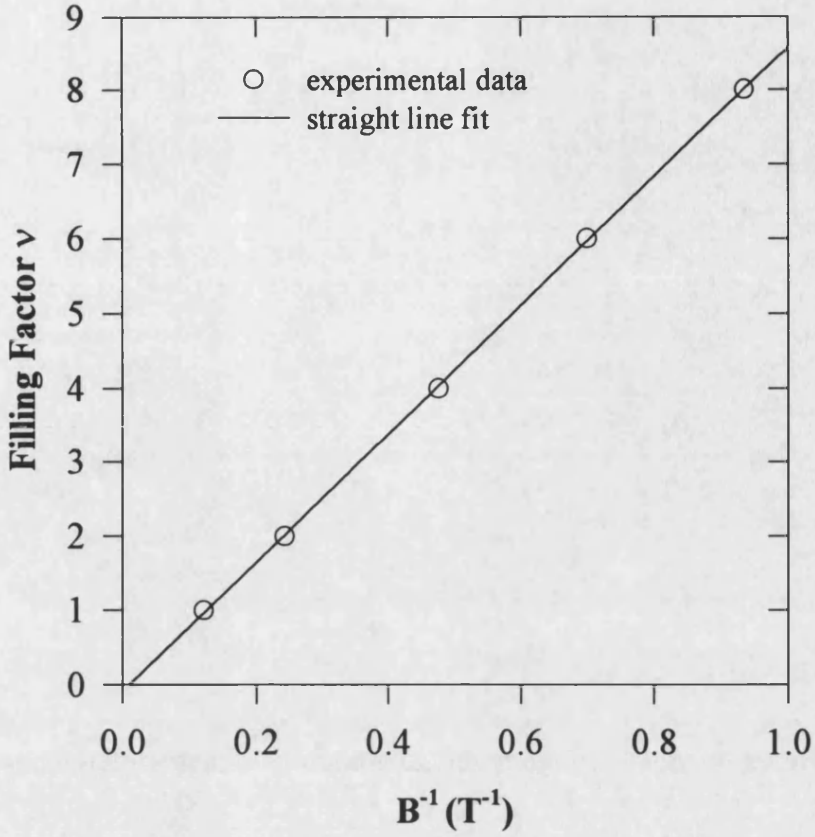

Figure 5.3: *Plot of integer filling factor versus inverse magnetic field. A linear fit to the experimental data (crosses) is also shown, and the electron concentration of the 2DEG was calculated from the gradient of the straight line as 2.09 (±0.03) x* 10^{15} m^{-2}.

Also marked in *Figure 5.2* are the magnitude of the velocity shift and attenuation. The peak in phase at ν=2 was ~0.11 (±0.006) radians in all measurements, corresponding to ~2/3 the size of the largest predicted velocity shift in the classical relaxation model. This may be explained by the fact that σ_{xx}^{2D} in this sample may not reach zero at 4.2K for this integer filling factor. However, the attenuation of the SAW intensity at this filling factor (ignoring the splitting for the moment which is described below) in this measurement is approximately half of the maximum predicted attenuation, although in other measurements the change in intensity was as large as the predicted maximum. It is possible that in this case a constant offset on the received SAW signal (perhaps from radio frequency pickup) has reduced the measured changes in intensity. This is hard to prove conclusively as different pre-amplifiers and signal levels were used during these initial measurements. In later measurements on other samples only the high gain pre-amplifier was used and the output level of the frequency synthesiser was set at -6.5dBm.

One notable feature of the intensity measurement is the splitting of the minima, clearly seen at $\upsilon = 2$. This is characteristic of SAW scattering and reflects the fact that maximum attenuation occurs when $\sigma_{xx}^{2D} = \sigma_M$ and not when $\sigma_{xx}^{2D} = 0$. Wixforth et al [14] observed that as SAW power is increased the splitting in the minima becomes less and less resolved until eventually at high power levels there is no observed splitting, and this was explained in terms of heating of the electron gas by the SAWs. *Figure 5.4* shows the $\upsilon = 2$ minima with the frequency synthesiser at 13.0dBm and -12.0dBm (giving a factor of approximately 17:1 between output voltages). There is little evidence to suggest that the splitting changes with SAW power in this range.

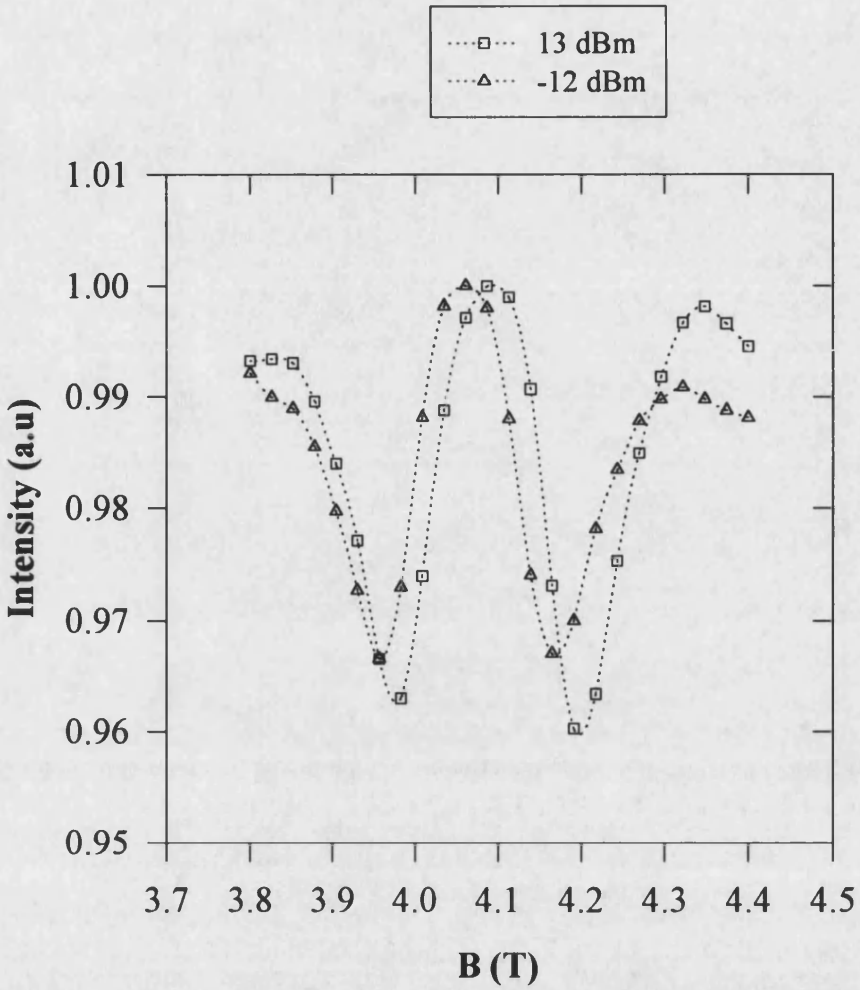

Figure 5.4: *Measured SAW intensity as a function of magnetic field, centred around filling factor 2, for two different frequency synthesiser output levels.*

The lineshapes of the minima were also investigated by Wixforth et al [14], particularly the observation that the minima in SAW intensity at an integer filling factor have different depths, which is not as expected from the classical model. Inhomogeneity of the 2DEG and parallel conduction in the AlGaAs were used to explain the appearance of a shoulder on the high field side and smearing out of the minimum. In *Figure 5.2* it is seen that in this case the low field minimum at $\upsilon = 2$ is larger indicating high homogeneity of the 2DEG and little or no parallel conduction. This is as expected as the 2DEG had not been illuminated, which is a large cause of inhomogeneity (if the illumination is inhomogeneous) and parallel conduction.

5.4 Quantum Mechanical Approach

When $ql<<1$, where q is the SAW wavevector and l is the elastic electron mean free path the SAW-electron interaction is most appropriately described in terms of the classical relaxation model. However, in the opposite limit when $ql>>1$ the interaction is best thought of as a quantum mechanical phonon absorption process as outlined in Chapter 3. The SAW wavevector is ~1.6 x 10^5 m^{-1} and the electron mean free path in the 2DEG at 4.2K is ~4.4μm, so that ql~1. A classical or quantum mechanical approach is therefore equally valid. At the Quantum Hall plateaux (i.e at integer filling factors) the electron mean free path is known to be very long (10-100μm) and it is unclear whether the classical approach is rigorously correct at these magnetic fields.

The energy of a SAW quantum is ~0.3μeV which is much less than either kT (~0.4meV at 4.2K) or the Fermi energy (~7meV). The SAW-electron interaction is hence quasielastic and to conserve energy, and momentum parallel to the crystal surface, SAW quanta can only be absorbed at the flanks of the Fermi disk; *Figure 5.5*.

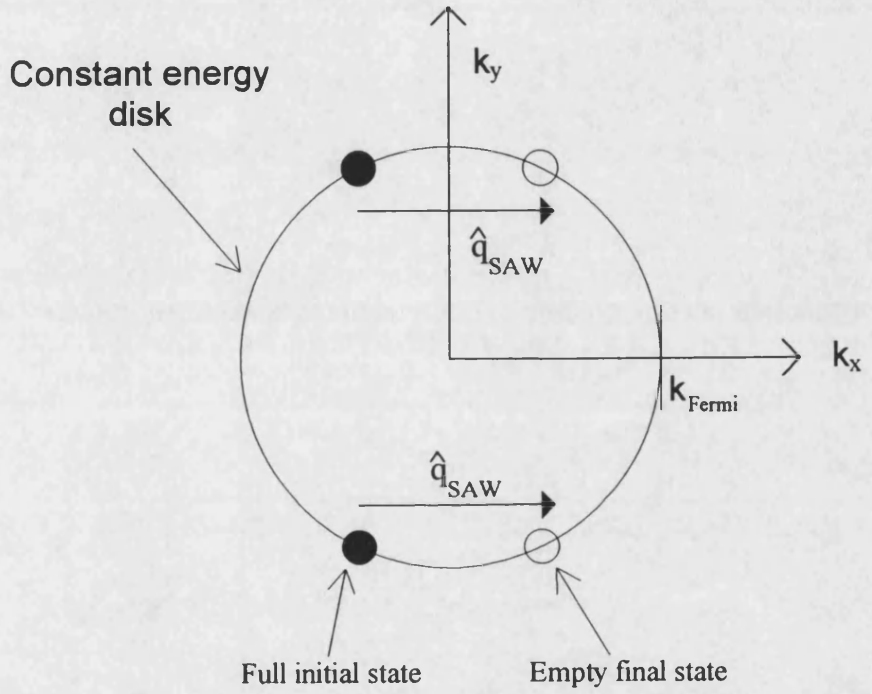

Figure 5.5: *Schematic representation of absorption of SAW quanta by electrons in a two dimensional electron gas.*

Fermi's Golden Rule calculations yield a SAW scattering rate τ^{-1} at zero magnetic field of [M. Boero, private communication]:

$$\tau^{-1} = \frac{2\pi}{\hbar}\frac{e^2 e_{14}^2}{\varepsilon_r^2 \varepsilon_0^2}\frac{\hbar}{2\rho\omega_{qs}}\left(\frac{q^2}{q^2+q_0^2}\right)^2\left(\frac{m^*}{\pi\hbar^2}\right) \tag{5.10}$$

where e_{14} , ρ, ε_r are respectively the piezoelectric constant, mass density, and the relative dielectric constant of GaAs, q, ω_q are the SAW wavevector and frequency, q_0 is the inverse Thomas-Fermi screening length, and m^* is the effective mass. The last term in the equation is the constant 2D density of states (Eqn. 2.6), and the previous term represents the electron screening of the coupling coefficient. In a non-zero magnetic field the scattering rate becomes:

$$\tau^{-1} \propto \left(\frac{q^2}{q^2+q_0^2(B)}\right)^2 \sum_n \left|\left\langle \psi_{n,x_0} \left| e^{iqx} \right| \psi_{n,x_0} \right\rangle\right|^2 D_n(E_F,B) \tag{5.11}$$

where the first term is the filling factor dependent screening. The second term, $\left\langle \psi_{n,x_0} \left| e^{iqx} \right| \psi_{n,x_0} \right\rangle$, is the "form factor" ($\sim e^{-\hbar q^2/4m^*\omega_c}$) and is ~1 in high magnetic fields $\left(B > 10^{-6}T\right)$. $D_n(E_F,B)$ is the Landau level density of states.

The inverse 2D Thomas-Fermi screening length q_0, for a single filled subband in zero magnetic field, is given by [88]:

$$q_0 = \frac{e^2}{2\pi\varepsilon_r\varepsilon_0}\left(\frac{m^*}{\pi\hbar^2}\right) \tag{5.12}$$

where ε_r is an effective dielectric constant (averaged over the GaAs and AlGaAs layers), and the last term is just the 2D density of states at the Fermi energy. The relative SAW-electron scattering rate was calculated over a very small magnetic field range (centred on filling factor 2), assuming that in a magnetic field the 2D density states in Eqn. 5.12 is

just replaced by the Landau level density of states at the Fermi energy. The broadening of the Landau levels, due to disorder, was taken as being of Gaussian form as described in Chapter 2 (Section 2.2.2) and a QBASIC programs was written to firstly calculate the Fermi energy at each magnetic field point. This was done iteratively using an asymptotic approximation for the total density of states, and taking the electron concentration to be 2.09×10^{15} m^{-2}. The density of states at the Fermi energy was then calculated using Eqns 2.22 and 2.23, with the scattering time τ_B taken as 2.0991×10^{-11} s, and the effective dielectric constant taken as 13.6. *Figure 5.6* shows the calculated scattering rates for SAW wavevectors of 1.6×10^{5} m^{-1} and 4.8×10^{5} m^{-1}. Each trace has been scaled to have unity maximum amplitude, although the scattering rate actually increases with increasing wavevector. Note that, as observed experimentally and also predicted in the classical model, there are two maxima in the scattering rate. However, the magnetic field separation of the maxima is much smaller than could ever be resolved experimentally. This implies that in non-zero magnetic field the inverse Thomas-Fermi screening length is not simply proportional to the density of states at the Fermi energy, for example the effects of localisation might dramatically alter the screening characteristics. Note also that the splitting of the peaks in the scattering rate increases with increasing SAW wavevector, and an interesting experiment would be to measure this splitting as a function of wavevector.

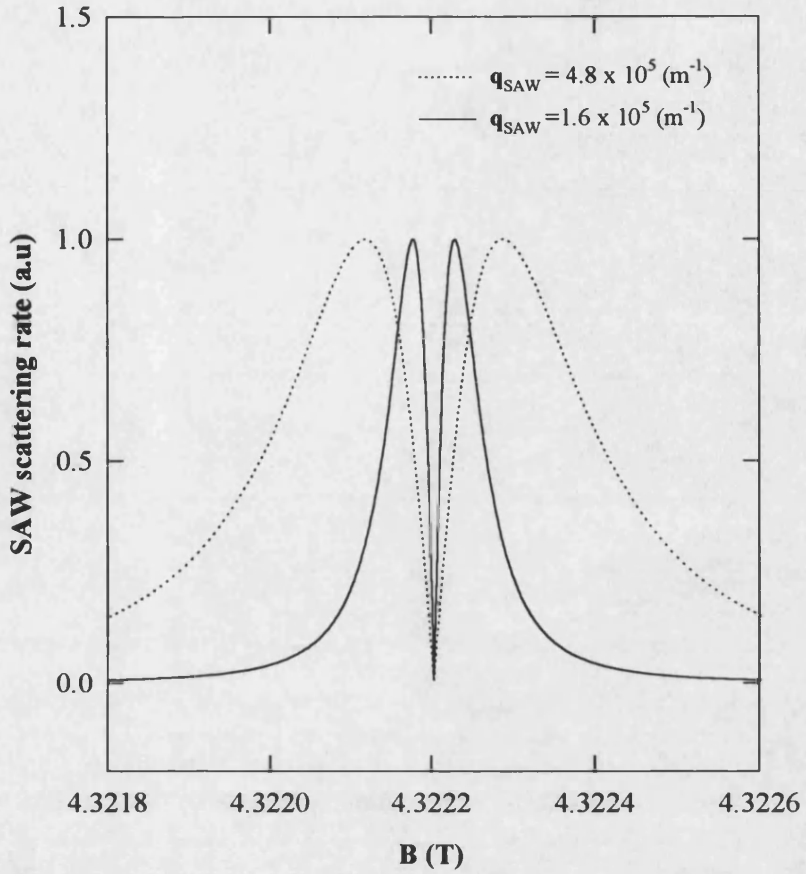

Figure 5.6: *Calculated SAW scattering rate, using the quantum mechanical approach outlined in the text, as a function of magnetic field, centred around filling factor 2, with* τ_B *taken as* 2.0991×10^{-11} *s.*

6 Surface Acoustic Wave Scattering from Quantum Wire Arrays

6.1 Introduction

In this chapter the first investigations of anisotropic surface acoustic wave (SAW) scattering at AlGaAs/GaAs quantum wire arrays are described. The chapter begins with a brief discussion of the classical and quantum mechanical models, first introduced in Chapter 3, that can be used to described the experimental data, with particular emphasis on the regimes where each approach is more rigorous. With the SAWs propagating perpendicular to the wires oscillations are observed in both the measured intensity and phase with increasing magnetic field (the phase is proportional to the SAW velocity: an increase in the velocity of the waves results in an increase in the measured phase - see Chapter 4). The oscillations are attributed to the magnetic depopulation of 1D subbands and the oscillations in intensity are fairly well modelled by the quantum mechanical description. To our knowledge no model yet exists to describe the phase data. With the SAWs propagating along the length of the wires no depopulation oscillations are observed, and at low electron concentrations the measured intensity and phase are independent of applied magnetic field. Both the quantum mechanical and classical approach predict very small interaction between the SAWs and the electrons in this orientation. Surprisingly, therefore, at high electron concentrations ($> 8.1 \times 10^8$ m^{-1} for 500nm wires, $> 3.8 \times 10^8$ m^{-1} for 250nm wires) there is a large increase in the SAW scattering rates, with a corresponding decrease in measured SAW intensity. Moreover

the scattering in this longitudinal direction at high carrier concentrations is three times larger than that of the unstructured 2DEG. At these electron concentrations both the measured intensity and phase are functions of magnetic field and show broad resonances. The origin of this enhanced scattering is as yet unclear, but it is speculated that the excitation of collected modes may explain this data.

6.2 Theory

6.2.1 Introduction

In the last Chapter (and in previous work on the interaction between SAWs and two dimensional systems) a classical relaxation model was used to described the experimental data, where the attenuation coefficient Γ, and velocity shift $\Delta v/v_0$ are functions of the sheet conductivity σ_{xx}^{2D} (Eqns 5.7 and 5.8), and Γ has a maximum near a characteristic conductivity $\sigma_M \left(\approx 3.3\text{x}10^{-7}\Omega^{-1}\right)$. This classical approach, however, is only strictly valid when $ql<<1$, where l is the electron elastic mean free path, and when $ql>>1$ quantum mechanical perturbation theory should be used (see Chapter 3). Perpendicular to the wires it is meaningless to define a conductivity and quantum mechanical perturbation theory must used to describe the SAW intensity measurements. These calculations, however, only describe SAW scattering rates and as yet there is no model to describe the phase data in either orientation. As a starting point it is interesting to consider phonon absorption as a mechanism of elastic stiffening. When the scattering rate is high energy is transferred from the SAWs to the electrons. Compared with when the scattering rate is low it now appears as though more energy is required to produce a

SAW of the same amplitude. This results in increased elastic constants ("stiffened") and the velocity of the SAW will therefore increase. However, this very simplistic approach is not consistent with the classical relaxation model, where the attenuation is a non-monotonic function of σ_M, whereas the velocity shift is a monotonic function of σ_M (Chapter 5).

Parallel to the wires, using the conductivity of the unstructured 2DEG as a starting point, it is estimated that ql~1 and neither a classical nor quantum mechanical approach is rigorously correct. However, it will be shown that both models predict negligibly small SAW scattering rates in this orientation.

6.2.2 SAW Propagation Perpendicular to the Wires

As the SAW energy quantum ($\hbar\omega$ ~300neV) is negligible compared to the 1D subband spacing (1-2meV), and the SAW wavevector ($q=1.6 \times 10^5$ m^{-1}) is very much smaller than a typical Fermi wavevector ($k_F \sim 5 \times 10^8$ m^{-1}), except when a subband is almost depopulated, only quasi-elastic intraband transitions need to be considered. In reality, of course, an electron in a perfect sample cannot accommodate even the very small energy of the SAW without a change of momentum (in the direction parallel to the wires) of size $\Delta k = m^* \Delta E / \hbar^2 k_f \approx 0.5 \times 10^3$ m^{-1}, where ΔE is the SAW energy quantum. This theory therefore assumes that disorder in our system relaxes momentum conservation, via the uncertainty principle on a scale of $\Delta k = 1/l \approx 1 \times 10^6$ m^{-1}, where l is the electron elastic mean free path in the wire $(l \approx 1\mu m)$, so that electron transitions are therefore allowed. With the SAW propagating in the [110] direction (x' co-ordinate) perpendicular to the wires total momentum conservation is relaxed and only electron momentum along the

wires must be conserved. In this case the scattering rate reduces to [M. Boero, private communication]:

$$\tau^{-1} = \frac{2\pi}{\hbar}\frac{e^2 e_{14}^2}{\varepsilon^2}\left(\frac{\hbar}{2\rho\omega_q}\right)\left(\frac{q^2}{q^2+q_0^2(B)}\right)^2 \sum_n \left|\langle\psi_n|e^{iqx'}|\psi_n\rangle\right|^2 \frac{1}{\pi\hbar}\sqrt{\frac{2m^*(B)}{(E_F - E_n(B))}} \tag{6.1}$$

where e_{14} , ρ, ε_r are respectively the piezoelectric constant, mass density, and the relative dielectric constant of GaAs, q, ω_q are the SAW wavevector and frequency, and q_0 is the inverse Thomas-Fermi screening length. The assumption of a parabolic confinement potential allows one to retain the concept of one dimensional subbands with modified effective masses $m^*(B)$ and subband energies $E_n(B)$ in finite magnetic fields [50]. The summation is over the n occupied 1D subbands and the matrix element or 'form factor' is close to unity in all cases since the SAW wavelength is very much longer than the width of the wires. Assuming that screening is weak in this system the B-dependent scattering rate is dominated by the total density of electronic states at the Fermi energy (last term of Eqn.6.1). This is plotted as a function of applied magnetic field in *Figure 6.1a* for typical wire parameters after negation in order to model the transmitted SAW intensity. Note the strong oscillations as the Fermi energy drops through the singular density of states at a 1D subband edge. The two traces represent two different levels of Gaussian disorder broadening (σ_E) of the subband energies.

6.2.3 SAW Propagation Parallel to the Wires

Applying the same quantum mechanical approach with the SAW parallel to the wires requires total momentum conservation. This prohibits all SAW absorption except for the

Umklapp like process across the Fermi line when $|\mathbf{k}_F^n| = |\mathbf{q}|/2$. This yields the following expression for the scattering rate:

$$\tau^{-1} = \frac{2\pi}{\hbar}\frac{e^2 e_{14}^2}{\varepsilon^2}\left(\frac{\hbar}{2\rho\omega_q}\right)\left(\frac{q^2}{q^2+q_0^2(B)}\right)^2 \frac{2m^*(B)}{\pi\hbar^2 q} \qquad \text{when } |\mathbf{q}| = 2|\mathbf{k}_F|$$

and zero otherwise.

(6.2)

Scattering is now only allowed for a few discrete magnetic fields just before a subband depopulates. The last term in Eqn.6.2 (the dominant contribution to the density of states at the Fermi energy when $|\mathbf{q}| = 2|\mathbf{k}_F|$) is plotted negated as a function of magnetic field in *Fig.6.1b* for the same wire parameters and disorder broadening as before and assuming that the SAW power is uniformly distributed in the range $f = 70 \pm 2.5$MHz due to the pulsed measurement mode used. Note that although oscillatory attenuation is predicted it is four orders of magnitude weaker than in the other orientation and it is very unlikely that it would be possible to measure such small changes in SAW intensity. An estimate of $\sigma_{xx} \sim 10^{-2}\ \Omega^{-1}$ in this orientation as the average 2D conductivity of the wires, is five orders of magnitude greater than σ_M and hence negligible SAW scattering rates are also predicted in the classical relaxation model (Eqn.5.7).

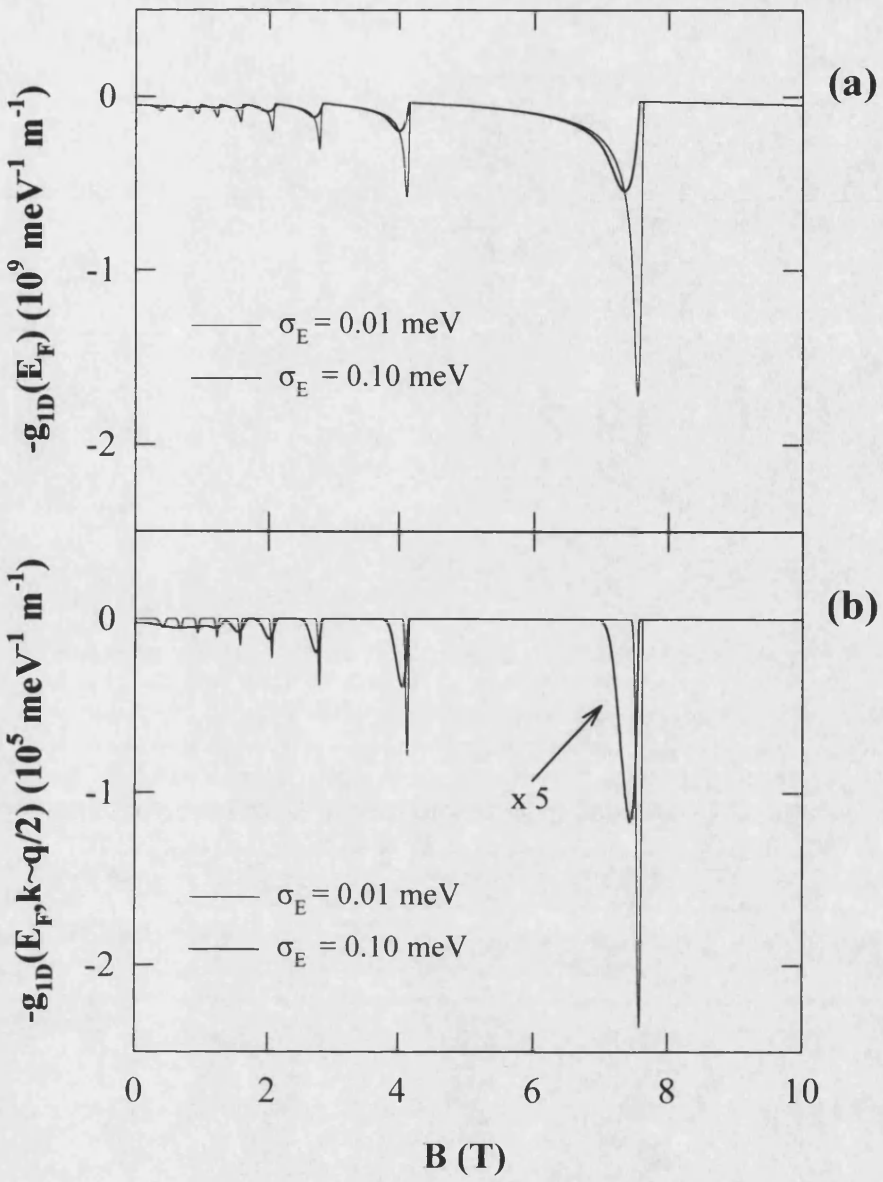

Figure 6.1: *(a) The calculated electronic density of states at the Fermi energy, negated, and (b) the contribution of the highest subband to the electronic density of states at the Fermi energy when* $\left|\mathbf{k}_F^n\right| = |\mathbf{q}|/2$, *negated, for* $N_{1D} = 7.6 \times 10^8\ m^{-1}$ *and* $\frac{1}{2}\hbar\omega_0 = 0.85meV$.

6.3 Experimental Results

The wires were orientated parallel to the [$\bar{1}$10] axis. The SAWs propagate either in the [$\bar{1}$10] or [110] directions, parallel or perpendicular to the wires, which have the strongest piezoelectric coupling coefficient [71], and carry a longitudinal electric field (see Chapter 3). The SAW power at the sample (~0.1μW) was reduced to well below the level where there was any evidence of heating of the electron gas. Measurements were performed in the 10T liquid helium cryostat described in Chapter 4, at ~1.3K, with the magnetic field perpendicular to the plane of the samples. Samples #8393no6 (500nm wide quantum wires) and #8393no15 (250nm wide quantum wires) were studied.

6.3.1 SAW Propagation Perpendicular to the Wires

Figures 6.2a,c show transmitted SAW intensity as a function of applied magnetic field for SAW propagation perpendicular to the 500nm and 250nm quantum wires respectively. Persistent photoconductivity [89] was used to increase the electron concentration in the samples (100ms long 50mA pulses from an infrared LED), and successive traces in both *Figures* have been offset by -10 units on the y-axis for clarity. Each trace has been labelled with a calculated 1D electron concentration (see below). In *Figure 6.2c* the traces are also labelled by the total illumination time in seconds since too few magneto-oscillations were observed in the zero illumination case for it to be possible to calculate an electron concentration.

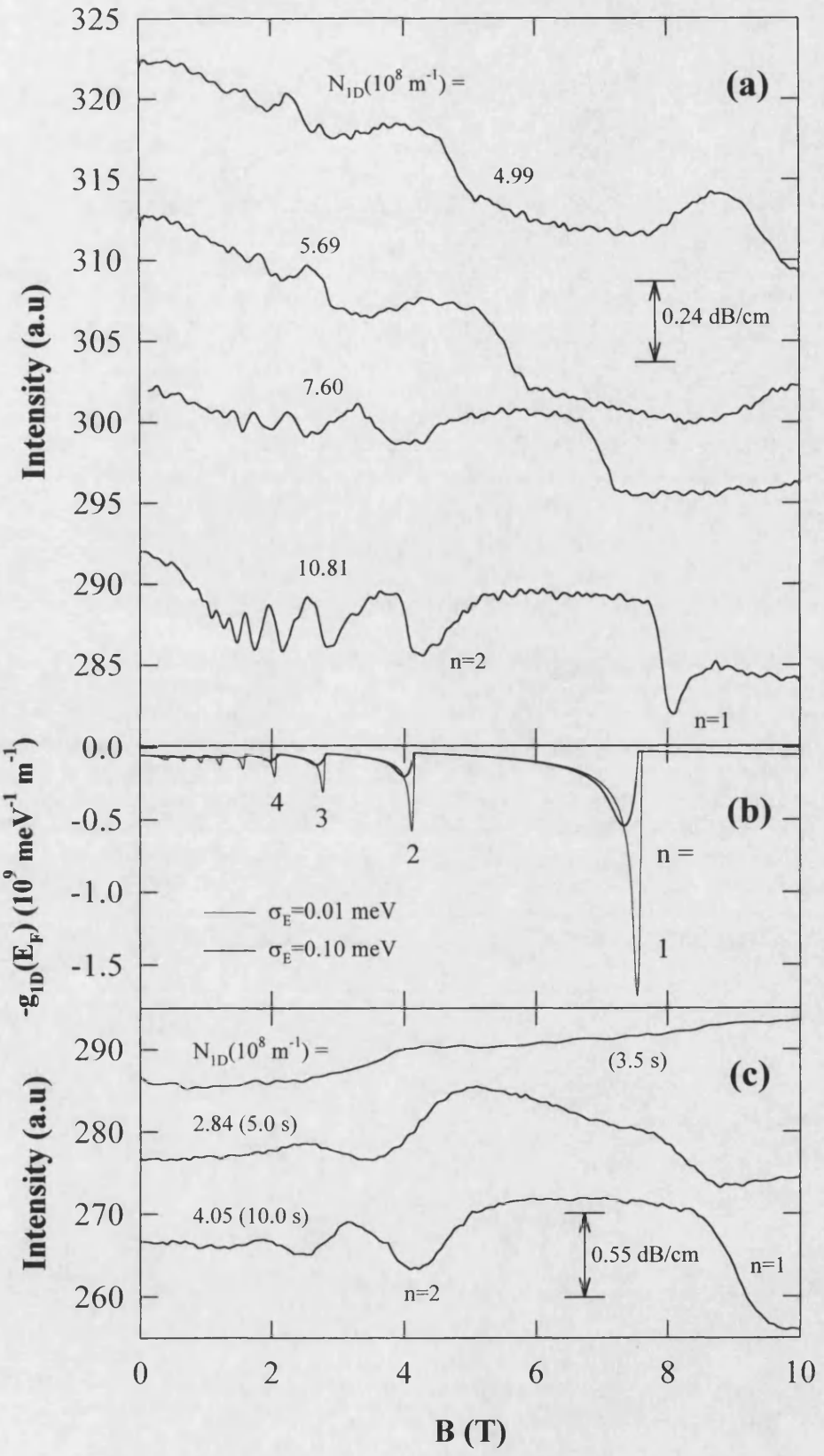

Figure 6.2: *Measured transmitted SAW intensity as a function of magnetic field for (a) 500nm and (c) 250nm quantum wires respectively, with the SAWs propagating perpendicular to the wires. The calculated electronic density of states at the Fermi energy is plotted negated in (b) for* $N_{1D} = 7.6 \times 10^8\ m^{-1}$ *and* $\frac{1}{2}\hbar\omega_0 = 0.85meV$.

The SAW intensity oscillations in both sizes of wires are attributed to the magnetic depopulation of 1D subbands, with the minima corresponding to the peak in the electronic density of states when the Fermi energy lies near a subband edge. The amplitudes of the oscillations are smaller than those measured in the unstructured two dimensional electron gas (2DEG) sample. For example in the wide wires the intensity falls by ~1.3% at the minimum labelled as n=2 in the highest electron concentration trace in *Figure 6.2a*. In the narrow wires the intensity falls by ~2% at the n=2 minimum in the highest electron concentration trace in *Figure 6.2c*. In the unstructured 2DEG sample the intensity falls by ~3% in all the minima above 1.5 Tesla. Note, however, that the sharp fall in the intensity at n=1 in both sizes of wires (~2% and ~5% respectively) is much larger than the low field oscillations. The Fermi's Golden rule calculations predict that when the penultimate 1D subband has been depopulated (i.e. at magnetic fields greater than the n=1 minimum) the intensity should increase close to the original level (*Fig.6.1a*). It is unclear why this does not occur, although it could be due to reduced spatial screening of disorder when only one subband is occupied or to an enhanced spin splitting of the last subband due to many body effects. However, this does not explain the large decrease in SAW intensity when depopulation into the last subband occurs.

The good agreement between the magnetic field positions of the minima in the negated density of states $-g(E_F)$ (plotted again in *Fig.6.2b*) and those of the equivalent SAW intensity (the third trace in *Fig.6.2a*) suggests that SAW absorption is, as predicted, predominantly proportional to the density of states at the Fermi energy. However, the failure of the simulation to faithfully reproduce the measured line-shapes of the wide wires near depopulation, even after the inclusion of substantial disorder broadening (e.g. σ_E = 0.1 meV), implies that the screening of the SAW-electron

interaction ($q_0(B)$) must play a significant role even in 1D. The lineshapes in the narrow wires, *Fig.6.2c*, agree rather better as one would expect since the more confined wavefunctions states will respond more weakly to the linear applied SAW electric field and hence screening will be less important. It is interesting to note that the n=1 minimum, and to some extent the higher minima, in the lowest trace of *Fig.6.2a* are much more clearly defined than at lower illumination levels suggesting that static screening of disorder is considerably more effective at very large electron concentrations as one would expect.

Assuming parabolic electrostatic confinement the following non-linear relationship can be derived for the magnetic field when the (n+1)th subband has just been depopulated [50]:

$$N_{1D} = \frac{2}{\pi}\left(2m^*/\hbar\right)^{1/2}\left[\left(\left(\frac{eB}{m^*}\right)^2 + \omega_0^2\right)^{\frac{3}{4}} \Big/ \omega_0\right]\sum_{j=1}^{n}\sqrt{j} \qquad (6.3)$$

where m^* is the normal effective mass, N_{1D} is the 1D electron concentration and ω_0 is a characteristic frequency defining the electrostatic confinement; $V_E(x) = \frac{1}{2}m\omega_0^2 x^2$. N_{1D} and the characteristic confinement energy ($\frac{1}{2}\hbar\omega_0$) can be obtained from linear plots of B^2 versus $\left(\sum_{j=1}^{n}\sqrt{j}\right)^{-1/3}$ at the SAW intensity minima. A typical such plot is shown in *Figure 6.3a*, while in *Figure 6.3b* a plot of integer filling factor versus inverse field is shown for the same data. At low magnetic fields, where the electrostatic confinement dominates the magnetic confinement, it is seen in *Fig.6.3b* that the linear relationship between filling factor and inverse field, which is valid for a two dimensional system, no longer applies.

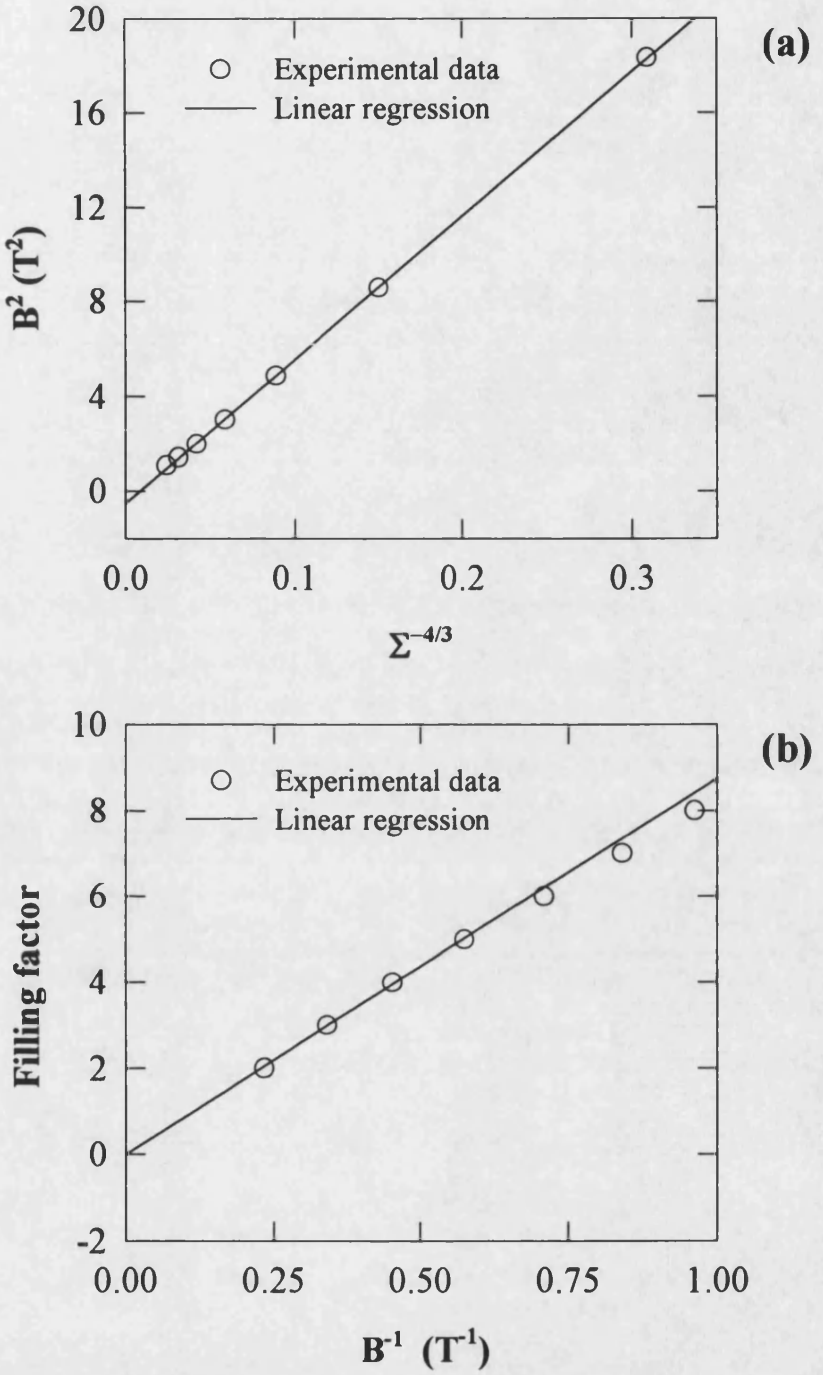

Figure 6.3: *(a) Typical linear fit to B^2 versus* $\left(\sum_{j=1}^{n}\sqrt{j}\right)^{-4/3}$. *(b) Plot of integer filling factor versus reciprocal magnetic field for the same data.*

In *Figure 6.4* N_{1D} and $\frac{1}{2}\hbar\omega_0$ are plotted for a range of illumination levels in both 500nm and 250nm wires. The values of N_{1D} and $\frac{1}{2}\hbar\omega_0$ obtained are consistent with figures obtained from magnetotransport measurements on similar quantum wires fabricated using holographic lithography and reactive ion etching [90]. The confinement energy of the narrow wires is approximately a factor of two larger than for the wide wires in broad agreement with the assumption of parabolic confinement. The characteristic confinement energy decreases with increasing carrier concentration in both cases. This is expected due to self-consistent screening of the potential [59], with a more rapid change visible in the 250nm wires which have less occupied 1D subbands. The effective electronic widths of the wires also increase with increasing electron concentration, and are 220nm and 75nm for the 500nm and 250nm wires respectively at the largest electron concentrations. These are smaller than the geometric widths due to sidewall depletion which is expected to be ~100nm at each edge [91].

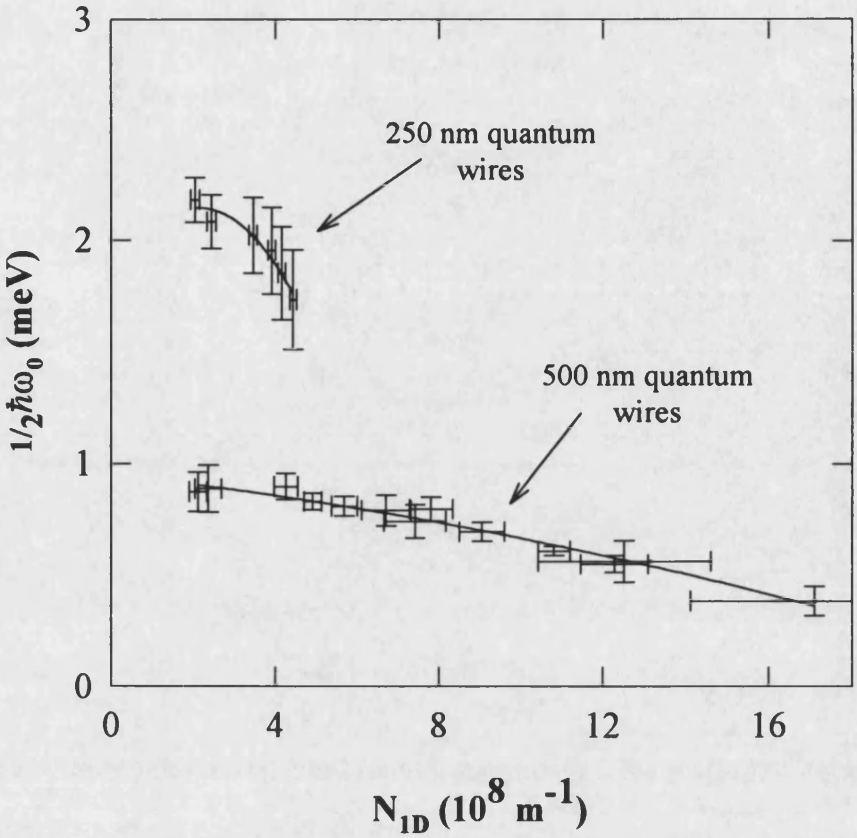

Figure 6.4: *Plot of characteristic confinement energies as a function of 1D electron concentration for both 500nm and 250nm quantum wires.*

Figures 6.5a,b show transmitted SAW phase as a function of applied magnetic field for SAW propagation perpendicular to the 500nm and 250nm quantum wires respectively. The illumination levels are the same as in *Figure 6.2* and each trace is labelled with a 1D electron concentration. Each trace has been offset to aid clarity, however, it should be remembered that absolute measured phase is arbitrary. The magneto-oscillations seen in the intensity are mirrored in the measured phase, with the phase having minima at magnetic fields at which the intensity is at a maximum. As with the intensity data the amplitudes of the oscillations are much smaller than in the case of the unstructured 2DEG sample. At the n=2 maxima the phase increases by ~0.012 rads. and ~ 0.015 rads. respectively in the wide and narrow wires which compares to the largest increase in measured phase, ~0.11 rads., in the unstructured 2DEG. However, at the n=1 maxima in both the wide and narrow wires there is a large, ~0.015 rads. and ~0.072 rads. respectively, increase in phase. As with the intensity the largest amplitude oscillations were observed in the 250nm wide wires, suggesting that the much more confined states in the narrow wires make them less sensitive to the disorder which might reduce the SAW-electron interaction in this orientation.

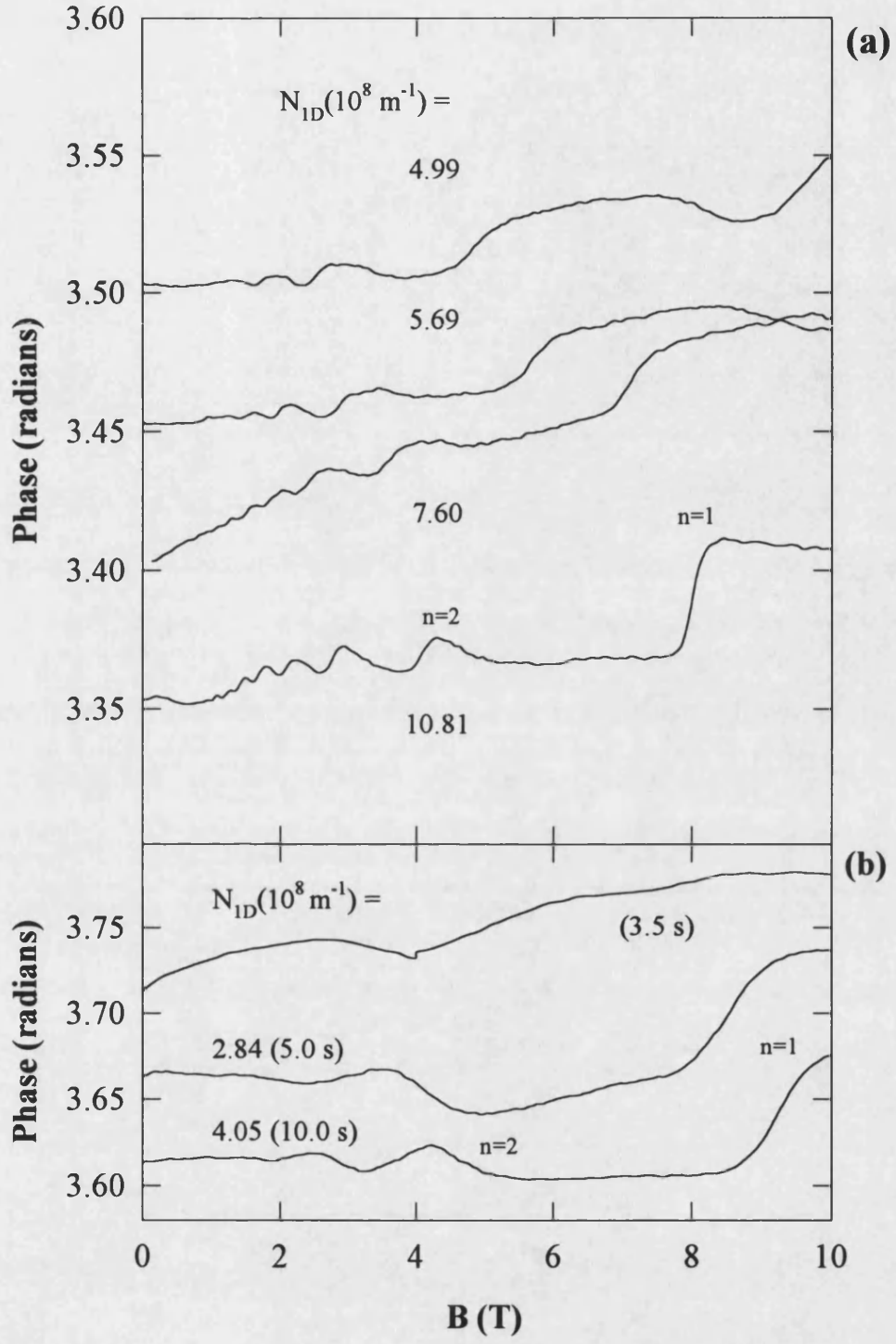

Figure 6.5: *Measured transmitted SAW phase as a function of magnetic field for (a) 500nm and (b) 250nm quantum wires respectively, with the SAWs propagating perpendicular to the wires.*

6.3.2 SAW Propagation Parallel to the Wires

Figures 6.6a and c show transmitted SAW intensity as a function of magnetic field with the SAWs propagating parallel to the wires. Note that the traces have not been offset in this *Figure*. The traces are labelled with N_{1D} values that have been established from consecutive measurements with the SAWs perpendicular to the wires. There is no evidence for Umklapp scattering near fields corresponding to subband depopulation as depicted in *Figure 6.6b*. This is to be expected due to the relative weakness of this channel. In the wide wires, starting with an electron concentration of 4.26×10^8 m^{-1}, an initial increase in electron concentration with illumination actually leads to an increase in the measured SAW intensity. With the SAWs propagating perpendicular to the wires fluctuations (probably the result of temperature changes-see Chapter 4) of ~1.5% were measured in the zero magnetic field SAW intensity as the illumination was increased. However, the increase in SAW intensity observed here is much greater (~7%) and may be due to a reduction in disorder coupling (disorder relaxes the momentum conservation rules) as N_{1D} is increased and the disorder is screened. Additional illumination, however, leads to a strong reduction in SAW intensity. In the narrow wires there is no significant change in SAW intensity from the zero illumination case (the dotted line in *Fig. 6.6c*) until the saturation electron concentration is almost reached, when the SAW intensity drops rapidly. This might again be due to the much more confined states in the narrow wires being less sensitive to disorder, and this is probably why there is no significant disorder coupling here.

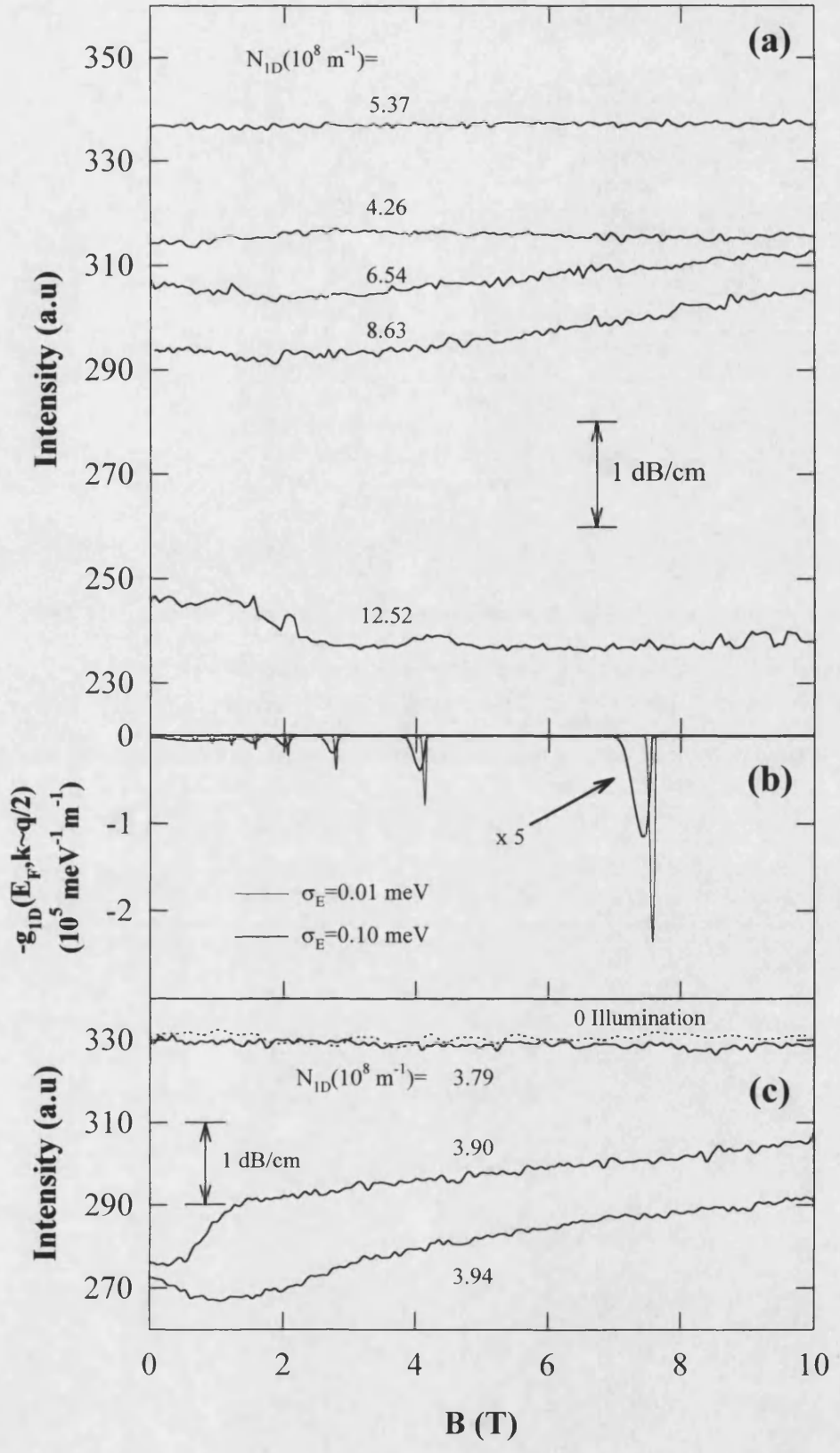

Figure 6.6: *Measured transmitted SAW intensity as a function of magnetic field for (a) 500nm and (c) 250nm quantum wires respectively, with the SAWs propagating parallel to the wires. The contribution of the highest subband to the electronic density of states at the Fermi energy when* $\left|\mathbf{k}_F^n\right| = |\mathbf{q}|/2$ *is plotted negated in (b) for* $N_{1D} = 7.6 \times 10^8\ m^{-1}$ *and* $\frac{1}{2}\hbar\omega_0 = 0.85meV$.

At high electron concentrations the transmitted SAW intensity in both cases seems to show broad magnetic field dependent resonances superimposed on a gently varying background. Parallel conduction in the modulation doped AlGaAs layer is one possible explanation of the large SAW absorption at high illumination levels. However, the fall in intensity from the low to high illumination traces corresponds to an attenuation of ~3.5dB/cm, which is considerably larger than the maximum possible predicted attenuation of ~1.1dB/cm for an unstructured 2DEG (when the conductivity changes from zero to σ_M), calculated using the classical relaxation model. In addition this strong attenuation is absent in the perpendicular direction (n^+ AlGaAs is highly disordered and would not be expected to show significant confinement effects, so that electrons in the AlGaAs layer would exhibit 2D properties) and these two facts indicate that parallel conduction is not responsible. SAWs have been used previously to study edge magnetoplasmons [57]. Since the frequency of these diverges as the applied magnetic field tends to zero they cannot alone explain our data, but the excitation of other plasmonic modes must be considered. Recent work by Sun *et al* [92] has calculated the collective excitations of arrays of parallel quantum well wires. In the limit of this experiment, when the electron wavefunctions in adjacent wires are uncoupled and the SAW wavelength is much greater than the wire period, they predict a 2D-plasmon-like acoustic intrasubband excitation in the direction of the wires which depends on the mean two-dimensional electron density, $\overline{N_{2D}}$; ($\omega_{pl} \approx \sqrt{\frac{\overline{N_{2D}} e^2}{2m^* \varepsilon} q}$). This dispersion curve is, however, three orders of magnitude too steep to allow the SAW to make energy and momentum conserving transitions. However, the theory neglects interactions

between 1D subbands and we speculate that this could strongly influence the plasmon dispersion and allow the SAWs to couple.

Figures 6.7a,b show transmitted SAW phase as a function of applied magnetic field for SAW propagation perpendicular to the 500nm and 250nm quantum wires respectively for the same illumination levels as in *Fig. 6.6.* It has already been noted that the absolute value of phase is arbitrary. However, the traces shown in *Fig. 6.7* were obtained on the same day under the same experimental conditions. No offset has been added, but the changes in the zero magnetic field phase with sample illumination should be viewed with caution. In both sizes of wires the zero magnetic value of the measured SAW phase decreases with increasing illumination and reflects the change in measured SAW intensity. The classical relaxation model predicts changes in the measured phase only when the conductivity of the wires lies approximately within the region $(\sigma_M/10) \leq \sigma_{xx} \leq (10\sigma_M)$, σ_M being the characteristic conductivity $(\approx 3.3\text{x}10^{-7}\,\Omega^{-1})$ (see Chapter 5). In this region the model predicts that measured phase will decrease with increasing conductivity of the wires. However, if the conductivity of the wires is assumed to be much higher than σ_M then an increase in the attenuation of the SAW signal, which is observed as the electron concentration is increased, would require a decrease in the conductivity of the wires. The observed decrease in measured phase, and the increase in SAW attenuation, in this orientation are therefore not consistent if described using the classical relaxation model.

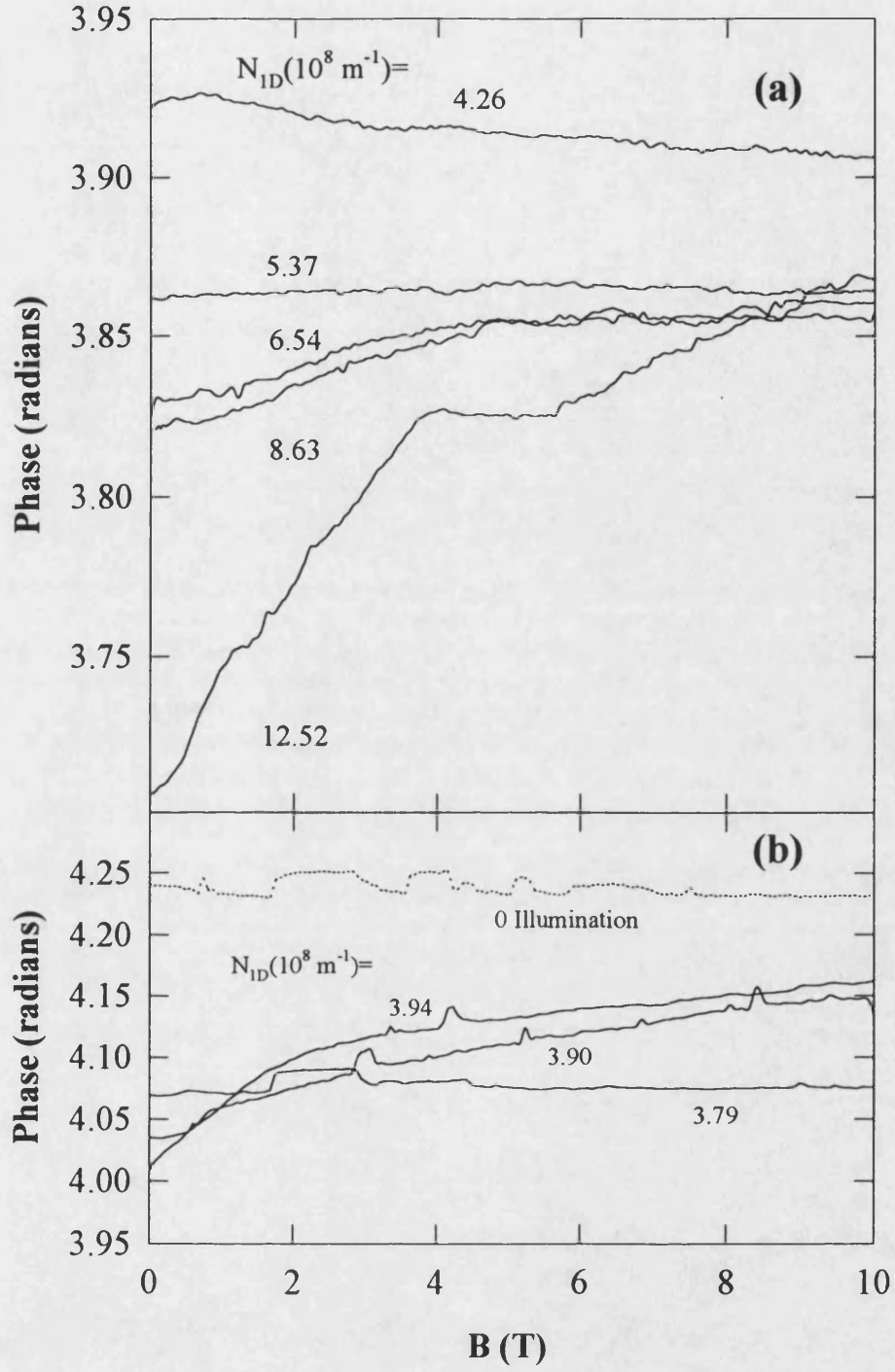

Figure 6.7: *Measured transmitted SAW phase as a function of magnetic field for (a) 500nm and (b) 250nm quantum wires respectively, with the SAWs propagating parallel to the wires.*

At large electron concentrations the measured SAW phase is magnetic field dependent, and shows broad resonances. Particularly striking in the last trace of *Fig. 6.7a* is the region between magnetic fields of approximately four and six Tesla in which the phase is independent of magnetic field. These "plateaux" were observed in previous measurements at similar electron concentrations, but at different magnetic fields. *Figure 6.8* shows a single measurement of SAW intensity and phase (taken in a different set of measurements) as a function of magnetic field, for SAW propagation parallel to the 500nm wires (at electron concentration of $12.28 \times 10^8\ m^{-1}$), in which the broad features in both the intensity and phase are particularly sharp. It is worth noting that here at approximately two Tesla the measured SAW intensity has a maximum, while the measured SAW phase has a minimum. However, at approximately four Tesla both the phase and intensity have minima. Again, assuming that the conductivity of the wires is much higher than the characteristic conductivity σ_M, it is impossible to explain this data consistently in terms of an oscillating magnetoconductivity using the classical relaxation model.

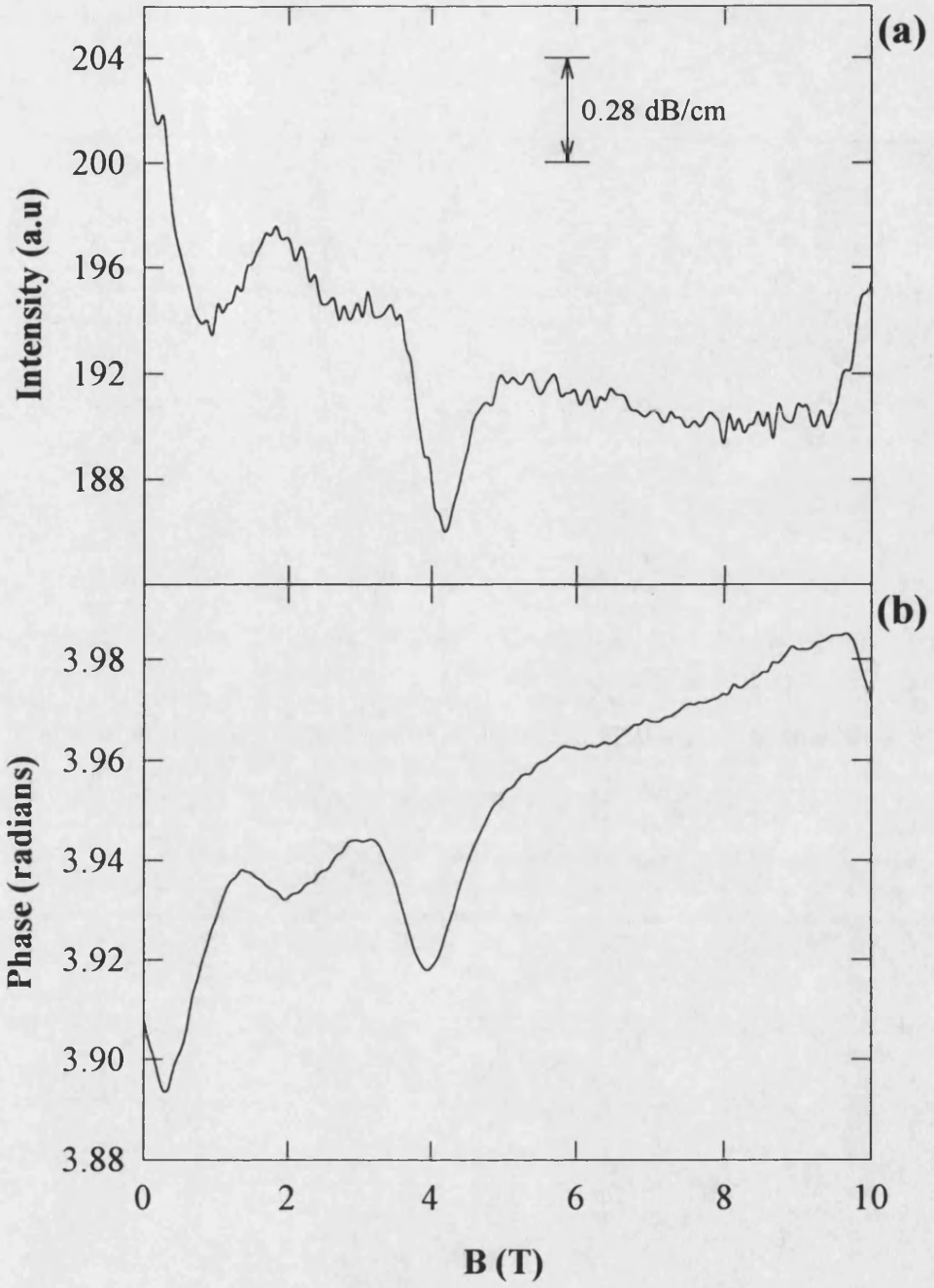

Figure 6.8: *Measured transmitted SAW (a) intensity and (b) phase as a function of magnetic field, for SAW propagation parallel to 500nm quantum wires, showing clearly defined structure in both the intensity and phase.*

7 Surface Acoustic Wave Scattering from Arrays of Quantum Dots

7.1 Introduction

In this chapter the first investigations of surface acoustic wave (SAW) scattering at AlGaAs/GaAs quantum dot arrays are described. In a quantum dot the electron energy is quantised into a set of discrete states. The classical relaxation model, used to describe the SAW-2DEG interaction, is therefore no longer applicable as conductivity is clearly not defined in this case. To first order the attenuation of the SAW signal can be described in terms of the absorption of single SAW quanta. The chapter therefore begins with the calculation of the phonon scattering rate using Fermi's Golden Rule. With a simple parabolic model for the electrostatic confinement of the dots the calculated scattering is shown to be have a strong magnetic field dependence, which follows the density of single electron level crossings. For a dot containing 210 electrons there is a maximum in the calculated scattering rate at ~ 2 Tesla, and a qualitatively similar magnetic field dependence is observed in the measured SAW intensity at high sample illumination levels.

7.2 Theory

In a quantum dot having a parabolic confinement potential of the form $V_{conf} = \frac{1}{2}m^*\omega_0^2 r^2$, where r is the distance from the centre of the dot, the single electron energy levels in a magnetic field are [51]:

$$E_{m,l} = \left(2m + |l| + 1\right)\sqrt{\left(\hbar\omega_0\right)^2 + \left(\frac{\hbar\omega_c}{2}\right)^2} + l\left(\frac{\hbar\omega_c}{2}\right) \tag{7.1}$$

where m = 0, 1, 2, ... and l = 0, ±1, ±2, ... are the radial and azimuthal quantum numbers respectively. This single electron energy spectrum is shown in *Figure 2.8*, which was calculated using a confinement energy of $\hbar\omega_0$=3.3meV. As the energy of the SAW quantum ($\hbar\omega$ ~300neV) is much smaller than the separation of the energy levels, scattering can only occur when at least two electronic states are very nearly degenerate at the Fermi energy. This is reflected in the SAW electron-scattering rate, which was calculated using Fermi's Golden rule as [M. Boero, private communication]:

$$\tau^{-1} = \frac{2\pi}{\hbar}\frac{e^2 e_{14}^2}{\varepsilon_0^2\varepsilon_r^2}\left(\frac{\hbar}{2\rho\omega_q}\right)\left(\frac{q^2}{q^2 + q_0^2(B)}\right)^2 \times \sum_{\substack{m,m',l,l' \\ m\neq m', l\neq l}} \left|\left\langle\varphi_{m'l'}\left|e^{iqx}\right|\varphi_{ml}\right\rangle\right|^2 \delta\left(E_F - E_{ml}, E_F - E_{m'l'}\right) \tag{7.2}$$

where e_{14}, ρ, ε_r are respectively the piezoelectric constant, mass density, and relative dielectric constant of GaAs, $\mathbf{q}$, ω_q are the SAW wavevector and frequency, q_0 is the magnetic field dependent inverse Thomas-Fermi screening length, and the matrix element $\left\langle\varphi_{m'l'}\left|e^{iqx}\right|\varphi_{ml}\right\rangle$ is fairly weak. The delta function forces the scattering rate to be zero unless $E_{ml} \cong E_{m'l'}$. However, it is estimated that in each quantum dot there are a few hundred electrons (the highest electron concentration measured in the quantum wires

samples was ~1x10^{9} m^{-1}, Chapter 6, giving 500 and 250 electrons/dot for the 500nm and 250nm dots respectively). It is therefore experimentally impossible to resolve individual degeneracies and it is therefore better to consider a density of level crossings per unit magnetic field interval. The simple non-interacting single electron model (assuming a parabolic confinement potential) predicts a strongly peaked density of level crossings at low fields, which rapidly falls off with increasing fields and is shown negated (to model the SAW intensity) in *Figure 7.1* for a dot containing 210 electrons and having a confining potential ($\hbar\omega_0$) of 1meV. Rather surprisingly the 2D Landau level "fan-like" structure (compare to *Fig. 2.6*) is still clearly reflected in this plot. It is also worth noting that at magnetic fields greater than ~ 6T the density of level crossings, in this simple single electron picture, is zero. At zero field there is a large degeneracy of states, however, this large degeneracy is broken if the confining potential is not perfectly parabolic. As the dots are unlikely to have perfect circular geometry (see Chapter 4), due to the nature of the holographic lithography process used to define them, it is unlikely that this is the case.

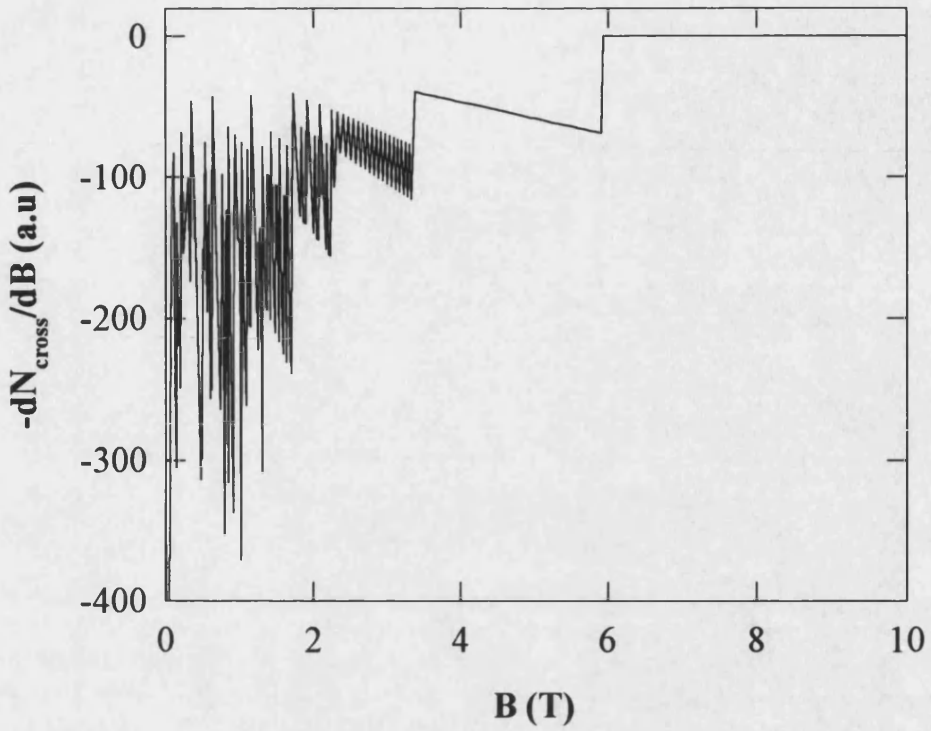

Figure 7.1: *Density of single electron level crossings, per unit magnetic field, as a function of magnetic field for a dot containing 210 electrons and a confining potential* $(\hbar\omega_0)$ *of 1meV.*

7.3 Experimental Results

Measurements were performed in the 10T liquid helium cryostat described in Chapter 4, at ~1.3K, with the magnetic field perpendicular to the plane of the samples. Two samples were used: #8393no19 and #8393no15 (with 500nm and 250nm widths respectively, and 1:1 aspect ratios), although much fewer measurements were made on sample #8393no15.

Figures 7.2a,b shows typical transmitted SAW intensity as a function of applied magnetic field for SAW propagation across samples #8393no19 and #8393no15 respectively. Persistent photoconductivity [89] was used to increase the electron concentration in the samples (100ms long 50mA pulses from an infrared LED). Each trace is labelled with the total illumination time in seconds. However it must be noted that there is no method of calculating the electron concentration from these illumination times. It is also likely that the relationship between illumination time and electron concentration, which is not necessarily linear, depends on a number of variable factors. For example, the rate at which the sample is cooled may influence the initial electron concentration. No offset has been added to the traces. These results show some remarkable features. In the 500nm dots the SAW intensity has a strong magnetic field dependence, which, as predicted qualitatively reflects the changing density of energy level crossings with increasing field as shown in *Figure 7.1* (if it is assumed that at zero field the multiple degeneracy are broken). The magnetic field dependence is most clearly visible in the 7s illumination trace in *Fig. 7.2a*, where even at high magnetic fields (>6T) the SAW intensity still has a clear magnetic field dependence.

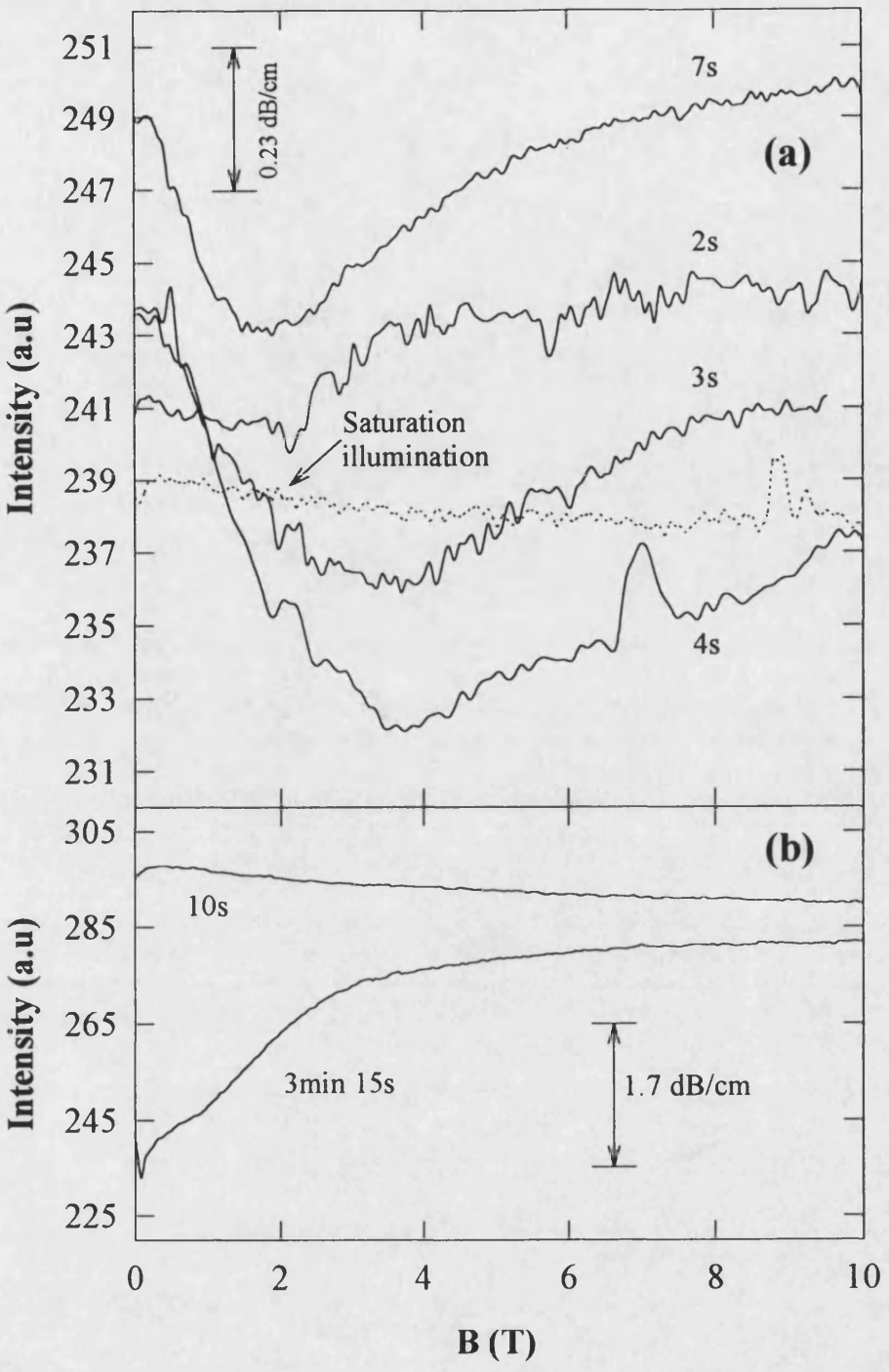

Figure 7.2: *Measured SAW intensity as a function of magnetic field for (a) 500nm and (b) 250nm quantum dots.*

This could perhaps be due to many body effects modifying the density of energy level crossing calculated using the simple single electron picture. The magnetic field position of the intensity minimum also appears to be a function of illumination, and further simulations are required to determine the origin of this effect . At saturation illumination the SAW intensity has very little magnetic field dependence. In the 250nm dots the highest illumination level trace has a similar magnetic field dependence, at fields greater than ~2 Tesla, to that seen in the larger dots. At zero magnetic field, however, there is strong attenuation of the SAW signal. This suggests that the confining potential is more parabolic than in the 500nm dots, due to the increased confinement, leading to a large degeneracy of electron states at zero field.

In the large dots, initially (as in all measurements on the large dots) the SAW intensity decreased with illumination; *Figure 7.2a*. After 4s illumination of the large dots, however, there is no further decrease in intensity and the trace at 5s (which has been omitted for clarity) has almost the same intensity as that at 4s while the trace at 7s has the pre-illumination intensity. The changes in SAW intensity with illumination are larger than any systematic drift that might be expected from the instrumentation, for example the zero magnetic field intensity falls by approximately 5% from the zero to the 2s illumination case (corresponding to an attenuation of ~0.7dB/cm), and similar changes with illumination were seen in all measurements (to quantify these changes precisely would require a knowledge of the electron concentration at each illumination level). In the 250nm dots it is more instructive to consider the SAW intensity at 10 Tesla, as the zero field intensity is strongly attenuated in the high illumination case, which falls by ~3% with illumination (corresponding to an attenuation of ~0.4dB/cm). In Chapter 2 it was noted that far-infra red (FIR) absorption measurements on arrays of quantum dots have

been successfully interpreted by considering the excitation of edge magnetoplasmons around individual dots (which are modelled as finite size circular disks of two dimensional electron gas), where the resonant frequency of the plasmons is inversely proportional to the radius of the disk (Equations (2.49) and (2.50)). However, in FIR measurements on AlGaAs/GaAs dots of radius 140nm (each dot containing 210 electrons) [90], the resonant plasmon frequency was measured as ~1000GHz at zero magnetic field. Even with much larger dots, therefore, it appears as though there would be little coupling to such plasmons with 70MHz SAWs. This suggests that a collective excitation, involving many dots, might be responsible for the observed changes in SAW intensity with illumination and this is an interesting area for future research.

In the large dots there is also a clear fine structure superimposed on the broad background which is larger than the noise level (which is expected to be much less than 1 unit in the y-axis; Chapter 4). These fluctuations appear to get finer at higher carrier concentrations, which is consistent with an increase in the number of level crossings, per unit field interval, with more electrons. With approximately 500 electrons in the large dots at saturation illumination the average magnetic field interval between level crossings, which is estimated as ~0.02T by dividing the field range by the number of electrons, is much less than the magnetic field resolution of these measurements (~0.07T), even if sample inhomogeneity is overlooked. Fine structure, however, might be expected due to irregular peaks in the single electron level crossing density that occur for certain special values of magnetic field, *Figure 7.1.* Calculations of the addition spectra of quantum dots [59] (the addition energy being the energy taken to add an electron to the dot) in strong magnetic fields show that when electron-electron interactions are taken into account there are magnetic fields at which there are large

changes in the addition energy, and hence electron configuration. *Figure 7.3* shows one measurement, taken with a higher than normal magnetic field resolution of 0.05T, that contains very strongly peaked structure both in the intensity, and in the measured phase, that might be the signature of many body effects. However, this result has yet to be satisfactorily reproduced. The measurements on the 250nm quantum dots, *Figure 7.2b*, were also both taken with a higher than normal magnetic field resolution (0.05T and 0.04T for the 10s and 3min 15s illuminated cases respectively). It is interesting to note that in these traces there is no evidence of any fine structure.

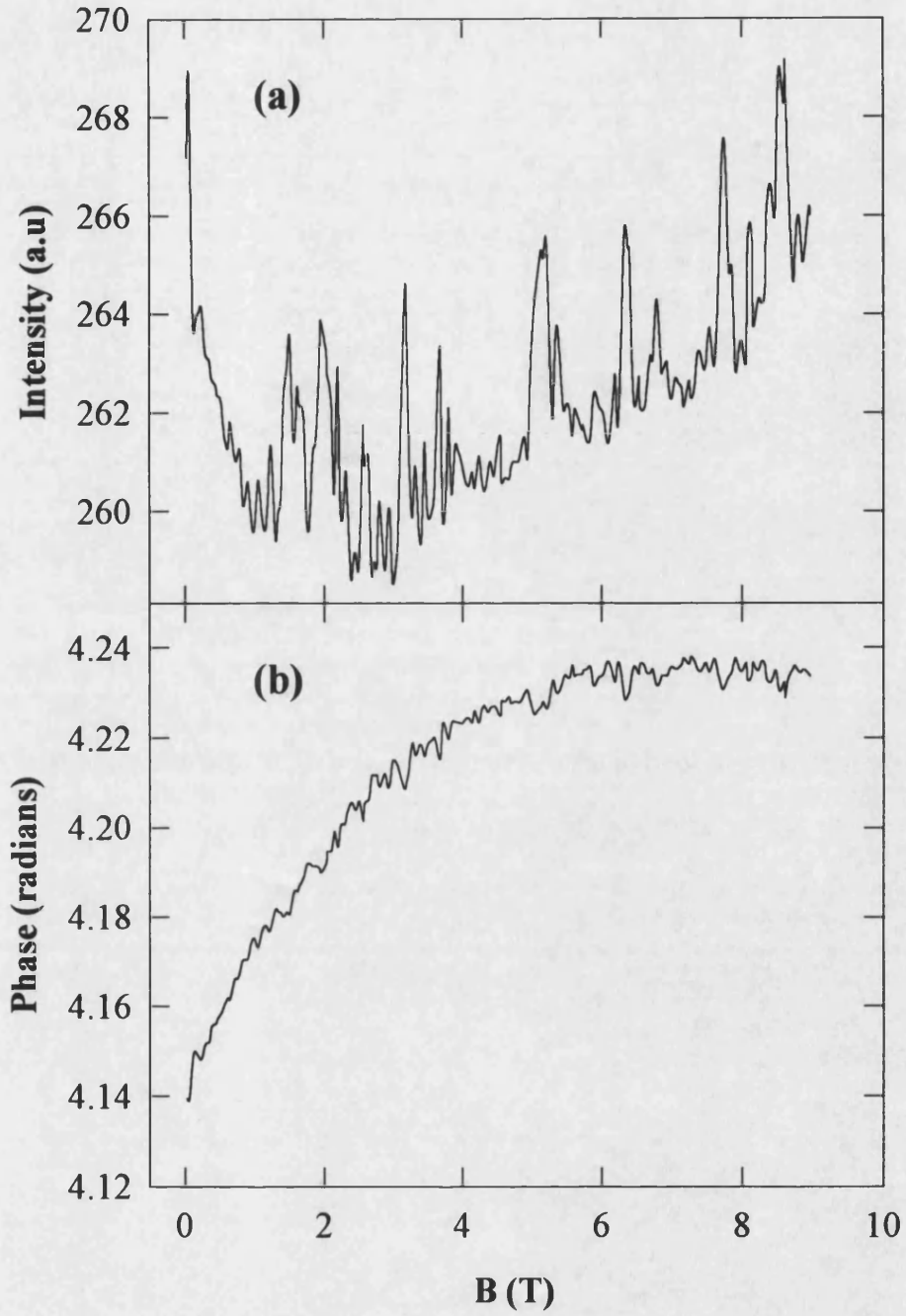

Figure 7.3: *Measured SAW intensity (a) and (b) phase as a function of magnetic field for 500nm quantum dots, showing very strongly peaked structure both in the intensity and phase.*

Figure 7.4a,b shows transmitted SAW phase as a function of applied magnetic field for SAW propagation across the 500nm and 250nm quantum dots for the same illumination levels as in *Figure 7.2*. Although the traces shown in *Figure 7.4* were obtained on the same day, and as far as possible under the same conditions, it must be remembered that absolute phase is arbitrary. In the large dots the increase in phase with magnetic field, which is seen in all but the saturation illumination case, however, is typical. At high magnetic fields the measured phase at all illumination levels tends towards the same value. Some fine structure is also visible above the noise level (which is expected to be ~0.002 radians; see Chapter 4), which again appears to be generally finer at high illumination levels. The phase in the 250nm dots at the low illumination level has a similar magnetic field dependence to that measured in the large dots. However, at the highest illumination level the phase has a broad peak at ~2Tesla. As mentioned previously, as far as is known, there is as yet no model to describe the phase data, which is hard to interpret intuitively in the case of quantum dots.

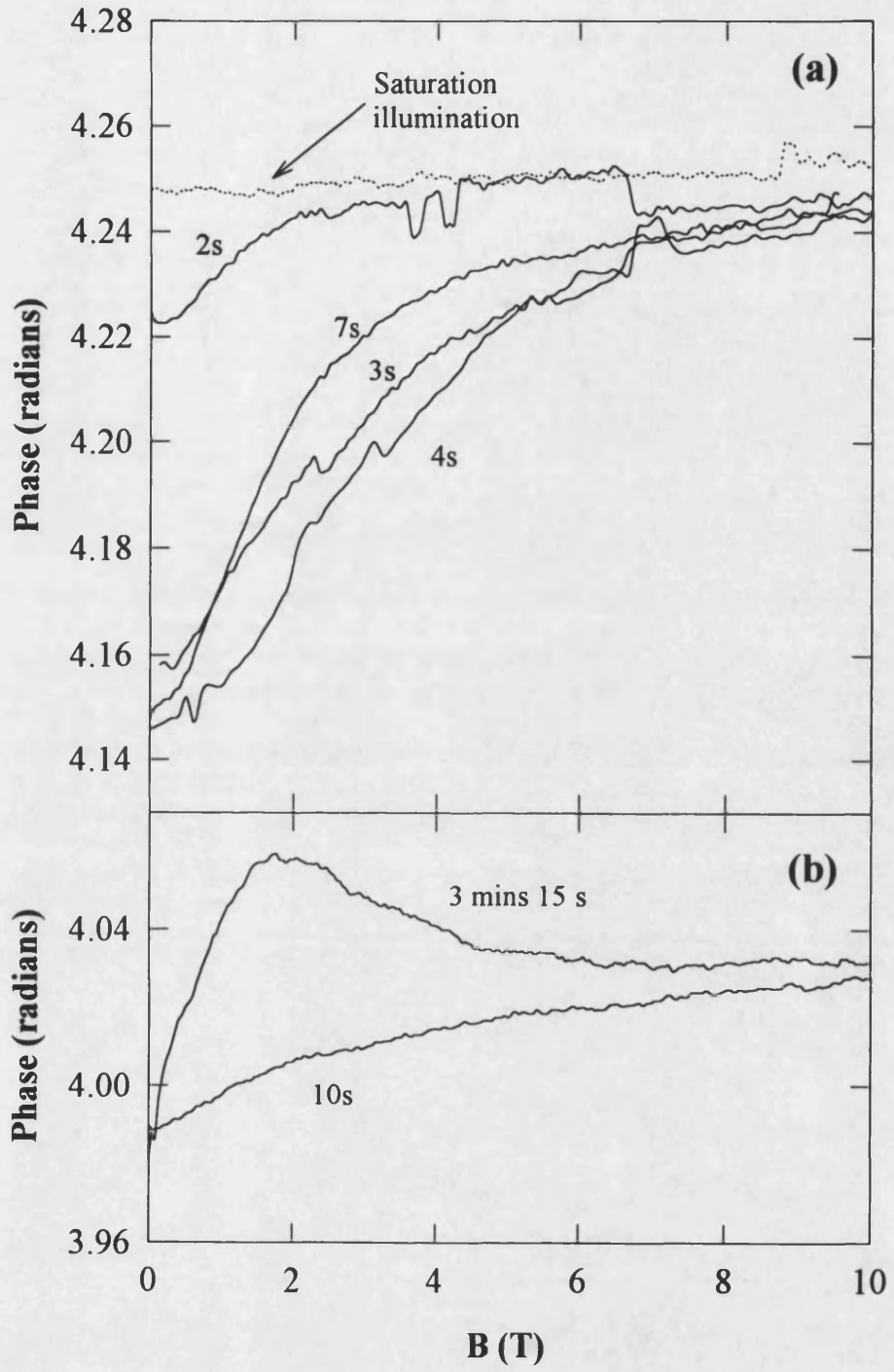

Figure 7.4: *Measured SAW phase as a function of magnetic field for (a) 500nm and (b) 250nm quantum dots.*

8 Conclusions

8.1 Introduction

The work presented in this thesis demonstrates that surface acoustic waves (SAWs) are a powerful tool for the investigation of the properties of semiconductor quantum nanostructures. While SAWs have been used extensively in the past to investigate two dimensional electron gases (2DEGs) they have never been previously used to study lower dimensional electron systems. Central to this work was the development of a detection system, based upon a custom-built phase sensitive detector, capable of measuring extremely small changes in the measured SAW amplitude and phase (which can then be converted into intensity and velocity shift respectively). The electronic properties of low dimensional systems were then probed by measuring the transmitted SAW intensity, and phase shift, as a function of applied magnetic field, and electron concentration (which was varied, via the persistent photoconductivity effect, using illumination).

Quantum wire and dot arrays were fabricated from an AlGaAs/GaAs heterojunction using holographic lithography and reactive ion etching. Great care was taken to realise homogeneous arrays. On the surface of every sample four interdigital transducers were deposited, one on each side of the nanostructure arrays, enabling SAWs to be excited in two propagation directions on the same sample. The interesting and intriguing results, obtained with two, one and zero dimensional systems, which are discussed in greater detail below, have been partially described by considering the SAW-electron interaction perturbatively and calculating SAW scattering rates using Fermi's

Golden Rule. This is in contrast with previous work on two dimensional systems in which the SAW-electron interaction was described using a classical relaxation model. The chapter begins with a brief description of the results obtained from unstructured 2DEG samples.

8.2 Two Dimensional Electron Gas

Oscillations were observed in the measured SAW intensity and velocity shift (phase) in an increasing perpendicular magnetic field. The magnitude of the oscillations were broadly as expected from the classical relaxation model, and the peaks in velocity shift were labelled with integer filling factors. A plot of integer filling factor versus inverse magnetic field was a straight line, and the 2D electron concentration calculated from the gradient was in good agreement with a value obtained from Hall measurements. A striking feature of the SAW intensity measurements was the double minima in intensity observed at magnetic fields close to integer filling factors. This splitting, which is characteristic of SAW measurements, is predicted both in the classical relaxation model and in Fermi's Golden Rule calculations, where the magnetic field separation of the minima is a function of SAW wavevector. As the power of the SAW signal was increased there was no evidence of heating of the electron gas (when the double minima in intensity would no longer be resolved).

8.3 Quantum Wire Arrays

With the SAWs perpendicular to the wires oscillations in the transmitted SAW intensity and phase (velocity shift) are observed as a function of magnetic field (applied perpendicular to the supporting substrate), with minima in the intensity, and maxima in the phase, occurring at fields corresponding to the depopulation of 1D subbands. The data are in fair agreement with theoretical quantum mechanical calculations, which show that the SAW attenuation reflects the electronic density of states at the Fermi energy. Assuming parabolic confinement the oscillations were labelled with subband index and values of 1D electron concentration and confinement energies were calculated which were in good agreement from those measured previously on similar nanostructures. When the SAWs propagate along the wires theory predicts strongly suppressed scattering rates. This reduction, however, is only clearly observed in the narrowest wires at low electron concentrations. Surprisingly, in this longitudinal direction, there is a sharp increase in the attenuation at high electron concentrations to a level which exceeds that of the unstructured 2DEG by a factor of three. It is speculated that this is due to excitation of intrasubband 2D plasmon-like modes, whose dispersion is strongly influenced by intersubband plasmons. At high illumination levels the phase increases significantly with increasing magnetic field. A common feature of these measurements are the formation of "plateaux" of constant phase over certain magnetic field ranges. As yet no model exists to describe the phase data.

8.4 Quantum Dot Arrays

Characteristic of measurements on 500nm wide quantum dots is a deep asymmetric minimum in the measured SAW intensity as a function of magnetic field (applied perpendicular to the supporting substrate). At highest illumination levels the 250nm dots show a similar magnetic field dependence, but with large attenuation of the SAW signal at zero magnetic field. Since the SAW can only excite electronic transitions near where two single electron levels cross at the Fermi energy the observed background is interpreted as a measure of the density of energy level crossings per unit magnetic field interval and this is reflected in the calculated SAW scattering rates. The observed data is in qualitative agreement with the scattering rate calculated assuming a simple non-interacting single electron model, in a parabolic confinement potential. Illumination of the dots causes the zero magnetic field intensity to first fall, and then recover to almost pre-illumination levels. As with the quantum wires this may be due to the excitation of a collective mode. The measured phase shows a strong magnetic field dependence in both sizes of dots, although this data is much harder to interpret intuitively than the intensity measurements. Fine structure superimposed in both the intensity and phase measurements is larger than the intrinsic noise level of the detection system and may indicate that many body effects significantly alter the single electron model.

8.5 Future Prospects

The present work has proven the value of SAWs as probe of the electronic properties of low dimensional electron systems and suggest a number of avenues for further investigation. One limitation of the present measurement system is the need to fabricate transducers on the surface of each sample. This could be overcome by having the transducers on a separate crystal (perhaps based on a commercially available device such as a lithium niobate SAW filter), preferably with a very large piezoelectric coupling coefficient The sample to be investigated would then be brought into close physical contact with the transducer crystal, so that the electric field of the SAWs penetrates the electronic system of interest.

Future work will concentrate on quantum wire and quantum dot arrays, with a range of wire and dot sizes and aspect ratios to further study possible collective excitations. A new detector system has also been developed to operate at 210 MHz (by slightly modifying the metallisation ratio of the transducers higher harmonics of the resonant frequency can be excited), which will lead to strong coupling. A new sample probe, with a rotating sample mount, will allow measurements in tilted magnetic fields, which will differentiate between isotropic and anisotropic magnetic field interactions (e.g Zeeman and Landau terms). Other interesting experiments include varying the orientation of the SAW propagation to the structures, for example having the SAWs propagating at 45 degrees to the wires. Further theoretical studies are required to construct a model for the effect of the SAW-electron interaction on the SAW velocity, enabling the interpretation of the phase measurements.

References

[1] L. L. Chang, L. Esaki, and R. Tsu, Appl. Phys. Lett. **24**, 593 (1974).

[2] H. Sakaki, in *Physics of Nanostructures*, edited by J. H. Davies and A. R. Long (Institute of Physics Publishing, Bristol, 1992), pp1-20.

[3] J. O. Williams, in *Growth and Characterisation of Semiconductors*, (Institute of Physics Publishing, Bristol, 1990), pp17-33.

[4] M. Jaros, *"Physics and Applications of Semiconductor Microstructures"*, Oxford University Press (1989).

[5] M. A. Paalanen, D. C. Tsui, and A. C. Gossard, Phys. Rev. B **25**, 5566 (1982).

[6] R. Willet, J. P. Eisenstein, H. L. Störmer, D. C. Tsui, A. C. Gossard, and J. H. English, Phys. Rev. Lett. **59**, 1776 (1987).

[7] H. van Houten, B. J. van Wees, M. G. J. Heijman, and J. P. André, Appl. Phys. Lett. **49**, 1781 (1986).

[8] Ch. Sikorski and U. Merkt, Phys. Rev. Lett. **62**, 2164 (1989).

[9] D. A. Wharam, T. J. Thornton, R. Newbury, M. Pepper, H. Ahmed, J. E. F. Frost, D. G. Hasko, D. C. Peacock, D. A. Ritchie, and G. A. C. Jones, J. Phys. C **21**, L209 (1988).

[10] P. L. McEuen, E. B. Foxman, U. Meirav, M. A. Kastner, Yigal Meir, Ned S. Wingreen, and S. J. Wind, Phys. Rev. Lett. **66,** 1926 (1991).

[11] H. Sakaki, in *Springer Series in Solid State Sciences*, edited by F. Kuchar, H. Heinrich and G. Bauer (Springer-Verlag, Berlin, 1990), Vol 97, p.2.

[12] C. Campbell, *"Surface Acoustic Wave Devices and Their Signal Processing Applications"*, Academic Press (1989).

[13] A. Wixforth, J. P Kotthaus, and G. Weimann, Phys. Rev. Lett. **56**, 2104 (1986).

[14] A. Wixforth, J. Scriba, M. Wassermeier, J. P Kotthaus, G. Weimann, and W. Schlapp, J. Appl. Phys. **64**, 2213 (1988).

[15] A. Wixforth, J. Scriba, M. Wassermeier, J. P Kotthaus, G. Weimann, and W. Schlapp, Phys. Rev. B **40**, 7874 (1989).

[16] V. W. Rampton, M. I. Newton, P. J. A. Carter, M. Henini, O. H. Hughes, M. Heath, M. Davies, L. J. Challis, and A. J. Kent, Acta Phys. Slovakia **40**, 5 (1990).

[17] F. Gullion, A. Sachrajda, M. D'Iorio, R. Boulet, and P. Coleridge, Can. J. Phys. **69**, 461 (1991).

[18] J. W. M. Campbell, F. Gullion, M. D'Iorio, M. Buchanan, and R. J. Stoner, Solid State Commun. **84**, 735 (1992).

[19] V. W. Rampton, K. McEnaney, A. G. Kozorezov, P. J. A. Carter. C. D. W. Wilkinson, M. Henini, and O. H. Hughes, Semicond. Sci. Technol. **7**, 641 (1992).

[20] C. Rocke, S. Manus, A. Wixforth, M. Sundaram, J. H. English, and A. C. Gossard, Appl. Phys. Lett. **65**, 2422 (1994).

[21] R. L. Willett, M. A. Paalanen, R. R. Ruel, K. W. West, L. N. Pfeiffer, and D. J. Bishop, Phys. Rev. Lett. **65**, 112 (1990).

[22] M. A. Paalenen, R. L. Willett, P. B. Littlewood, R. R. Ruel, K. W. West, L. N. Pfeiffer, and D. J. Bishop, Phys. Rev. B **45**, 11342 (1992).

[23] R. L. Willett, R. R. Ruel, M. A. Paalanen, K. W. West, and L. N. Pfeiffer, Phys. Rev. B **47**, 7344 (1993).

[24] R. L. Willett, R. R. Ruel, K. W. West, and L. N. Pfeiffer, Phys. Rev. Lett. **71**, 3846 (1993).

[25] R. L. Willett, Surf. Sci. **305**, 76 (1994).

[26] R. L. Willett, K. W. West, and L. N. Pfeiffer, Phys. Rev. Lett. **75**, 2988 (1995).

[27] A. Schenstrom, Y. J. Qian, M. -F. Xu, H. -P. Baum, M. Levy, and Bimal K. Sarma, Solid State Commun. **65**, 739 (1988).

[28] A. L. Efros and Yu. M. Galperin, Phys. Rev. Lett. **64**, 1959 (1990).

[29] A. Esslinger, A. Wixforth, R. W. Winkler, J. P. Kotthaus, H. Nickel, W. Schlapp, and R. Lösch, Solid State Commun. **84**, 939 (1992).

[30] Vladimir I. Fal'ko, S. V. Meshkov, and S. V. Iordanskii, Phys. Rev. B **47**, 9910 (1993).

[31] A. Esslinger, R. W. Winkler, C. Rocke, A. Wixforth, J. P. Kotthaus, H. Nickel, W. Schlapp, and R. Lösch, Surf. Sci. **305**, 83 (1994).

[32] J. M. Shilton, D. R. Mace, V. I. Talyanskii, M. Y. Simmons, M. Pepper, A. C Churhill, and D. A. Ritchie, J. Phys.: Condens. Matter 7, 7675 (1995).

[33] J. M. Shilton, D. R. Mace, V. I. Talyanskii, M. Pepper, M. Y. Simmons, A. C Churhill, and D. A. Ritchie, Phys. Rev. B **51**, 14770 (1995).

[34] J. M. Shilton, D. R. Mace, V. I. Talyanskii, Yu Galperin, M. Y. Simmons, M. Pepper, and D. A. Ritchie, J. Phys.: Condens, Matter **8**, L337 (1996).

[35] D. Heitmann, in *Physics of Nanostructures*, edited by J. H. Davies and A. R. Long (Institute of Physics Publishing, Bristol, 1992), pp229-256.

[36] B. J. van Wees, H. van Houten, C. W. J. Beenakker, J. G. Williamson, L. P. Kouwenhoven, D. van der Marel, and C. T. Foxon, Phys. Rev. Lett. **60**, 848 (1988).

[37] C. Weisbuch and B. Vinter, *"Quantum Semiconductor Structures"*, Academic Press (1991).

[38] M. J. Kelly, *"Low-Dimensional Semiconductors: Materials, Physics, Technology, Devices"*, Oxford University Press (1995).

[39] P. C. W. Davies, *"Quantum Mechanics"*, Routledge & Kegan Paul (1984).

[40] T. Englert, D. C. Tsui, A. C. Gossard, and C. Uihlein, Surf. Sci. **113**, 295 (1982).

[41] T. Ando and Y. Uemura, J. Phys. Soc. Japan **36**, 959 (1974).

[42] R. R. Gerhardts and V. Gudmundsson, Phys. Rev. B **34**, 2999 (1986).

[43] E. Stahl, D. Weiss, G. Weinmann, K. Von Klitzing, and K. Ploog, J. Phys. C **18**, L783 (1985).

[44] J. P. Eisenstein, H. L. Störmer, V. Narayanamurti, A. Y. Cho, A. C. Gossard, and C. W. Tu, Phys. Rev. Lett. **55**, 875 (1985).

[45] H. Aoki and T. Ando, Solid State Commun. **38**, 1079 (1981).

[46] K. Von Klitzing, G. Dorda, and M. Pepper, Phys. Rev. Lett. **45**, 494 (1980).

[47] R. J. Haug, Semicond. Sci. Technol. **8**, 131 (1993).

[48] M. Büttiker, Phys. Rev. B **38**, 9375 (1986).

[49] K. -F. Berggren, T. J. Thornton, D. J. Newson, and M. Pepper, Phys. Rev. Lett. **57**, 1769 (1986).

[50] K. -F. Beggren, G. Roos and H. Van Houten, Phys. Rev. B **37**, 10118 (1988).

[51] V. Fock, Z. Phys. **47**, 446 (1928).

[52] T. N. Theis, J. P. Kotthaus, and P. J. Stiles, Solid State Commun. **26**, 603 (1978).

[53] E. Batke, D. Heitmann, and C. W. Tu, Phys. Rev. B **34**, 6951 (1986).

[54] A. L. Fetter, Phys. Rev. B **32**, 7676 (1985).

[55] T. N. Theis, J. P. Kotthaus, and P. J. Stiles, Solid State Commun. **24**, 273 (1977).

[56] D. Heitmann, K. Kern, T. Demel, P. Grambow, K. Ploog, and Y. H. Zhang, Surf. Sci. **267**, 245 (1992).

[57] P. Hawker, P. F. Lenne, M. Tonouchi, V. W. Rampton, C. J. Mellor, and M. Henini, Physica B **194-196**, 419 (1994).

[58] B. I. Halperin, P. A. Lee, N. Read, Phys. Rev. B **47**, 7312 (1993).

[59] S. E. Laux, D. J. Frank, and F. Stern, Surf. Sci. **196**, 101 (1988).

[60] S.-R. Eric Yang, A.H. MacDonald and M. D. Johnson Phys. Rev. Lett. **71**, 3194 (1993).

[61] Lord Rayleigh, Proc. London Math. Soc. **17**, 4 (1885).

[62] R. M. White and F. W. Voltmer, Appl. Phys. Lett. **7**, 314 (1965).

[63] D. P. Morgan, *"Surface Acoustic Wave Devices for Signal Processing"*, Elsevier (1991).

[64] see: Sensors and Actuators **A 44**, 1994.

[65] J. F. Nye, *"Physical Properties of Crystals"*, Oxford University Press (1985).

[66] C. Kittel, *"Introduction to Solid State Physics"*, John Wiley & Sons (1986).

[67] J. S. Blakemore, J. Appl. Phys. **53**, R123 (1982).

[68] Sadao Adachi, J. Appl. Phys. **58**, R1 (1985).

[69] G. W. Farnell, in *Acoustic Surface Waves*, edited by A. A. Oliner (Springer, Berlin, 1978), pp13-60.

[70] T. C. Lim and G. W. Farnell, J. Acoust. Soc. America **45**, 845 (1968).

[71] R. T. Webster and P. H. Carr, in *Rayleigh Waves, Theory and Applications*, edited by E. A. Ash and E. G. S. Paige, (Springer, Berlin, 1985), pp 122-130.

[72] J. H. McFee, in *Physical Acoustics*, edited by W. P. Mason, (Academic Press, New York, 1966), Vol. 4A, pp 1-45.

[73] A. R. Hutson and D. L. White, J. Appl. Phys. **33**, 40 (1962).

[74] R. Adler, IEEE Trans. Sonics Ultrason. **SU-18**, 115 (1971).

[75] Enrico Fermi, *"Nuclear Physics"*, The University of Chicago Press, Chicago, (1949).

[76] B. K. Ridley, *Quantum Processes in Semiconductors*, Clarendon Press (1982).

[77] H. Engan, IEEE Trans. Electron Devices, **ED-16**, 1014 (1969).

[78] J.J. Harris, C. T. Foxon, K. W. J. Barnham, D. E. Lacklison, J. Hewett, and C. White, J. Appl. Phys. **61**, 1219 (1987).

[79] F. Stern and S. Das Sarma Phys. Rev. B **30**, 840 (1984).

[80] J. J. Harris, J. A. Pals, and R. Woltjer, Rep. Prog. Phys. **52**, 1217 (1989).

[81] T. Demel, D. Heitmann, P. Grambow, K. Ploog, Appl. Phys. Lett. **53**, 2176 (1988).

[82] D. W. Shaw, J. Electrochem. Soc: Solid State Science and Technology **128**, 874 (1981).

[83] G. K. White, *"Experimental Techniques in Low Temperature Physics"*, Clarendon Press (1979).

[84] R. I. Cottam and G. A. Saunders, J. Phys. C **6**, 2105 (1973).

[85] S. Datta, *"Surface Acoustic Wave Devices"*, Prentice-Hall (1986).

[86] W. H. Press, B. P. Flannery, S. A. Teukolsky and W. T. Vetterling, *"Numerical Recipes: the Art of Scientific Computing"*, Cambridge University Press (1986).

[87] R. I. Cottam and G. A. Saunders. J. Phys. C 7, 2447 (1974).

[88] H. Haug and S. W. Koch, *"Quantum Theory of the Optical and Electronic Properties of Semiconductors"*, World Scientific (1990).

[89] D. E. Lacklison, J. J. Harris, C. T. Foxon, J. Hewett, D. Hilton, and C. Roberts, Semicond. Sci. Technol. **3**, 633 (1988).

[90] T. Demel, D. Heitmann, P. Grambow, and K. Ploog, Superlatt. Microstruct. **9**, 285 (1991).

[91] T. Demel, D. Heitmann, P. Grambow, and K. Ploog, Phys. Rev. B **38**, 12732 (1988).

[92] H. Sun, Y. L. Liu and K. W. Yu, J. Phys.: Condens. Matter 7, 3539 (1995).